Dynamic Analysis of River Embankments during Earthquakes based on Finite Deformation Theory Considering Liquefaction

2014

Hamidreza SADEGHI

Abstract

The dynamic behavior of geotechnical structures during earthquakes and the induced liquefaction has been the subject of many numerical and experimental investigations. The failure patterns of river embankments during earthquakes have also attracted much attention. However, liquefaction phenomena and the numerous factors that affect the level of damage and the deformation-failure patterns in river embankments still contain many unknown elements. Problems such as the adoption of suitable constitutive models for the cyclic behavior of soils, the lack of material parameters, structural degradation, rate dependency, unsaturated soil behavior, the heterogeneity of the ground, the effect of the duration and the frequency content of earthquakes, and the possible subsoil formations add to the complexity of the dynamic behavior of river embankments.

In the present study, the dynamic behavior of river embankments during large earthquakes is studied using a multiphase finite element method based on the finite deformation theory. An elasto-viscoplastic cyclic model is used for clay, while an elasto-plastic cyclic model is adopted for sand. Dynamic analyzes have been performed using code COMVI-2D-DY in which the unsaturated soil behavior and the finite deformation formulation are included. Efforts are made to find the different possible failure mechanisms and damage patterns of river embankments due to earthquakes and liquefaction using the above-mentioned finite element code. Moreover, achieving the complex deformation-failure modes that are not usually considered in geotechnical engineering practice, using the finite element method, is of great interest.

In the numerical analysis, four typical formations of embankment-foundation profiles are used considering the damage patterns observed in the 2011 off the Pacific Coast of Tohoku Earthquake. The failure modes of embankments which are not common in ordinary geotechnical engineering practice are what grab the most attention. It is observed that in the case of the settlement of an embankment into a saturated ground, with the existence of a groundwater table inside the embankment, not only do the damage levels become extreme, but inclined cracks appear in the embankment body. This deformation-failure mode is achieved in the present study and the results seem to be in agreement with the field observations.

The differences between the infinitesimal and the finite deformation methods have also remained unclear in the dynamic analysis of river embankments considering liquefaction. Although the finite deformation and the updated Lagrangian methods seem to be more suitable for the study of large deformations in geotechnical structures, there are some limitations for high rates of loading. In this study, a comparison is made for the dynamic behavior of embankments with liquefiable foundations between the infinitesimal formulation and the finite deformation scheme. The results show that the finite deformation formulation leads to more realistic results in the cases concerned with liquefaction and large deformations.

Acknowledgements

The present research was performed over a period of three years at the Geomechanics Laboratory, Department of Civil and Earth Resources Engineering, Kyoto University. This research could not have been achieved without the great support and attention of my supervisors, friends, and family to whom it is my distinct pleasure to declare my gratitude.

First and foremost, I would like to express my profound and sincere appreciation to Emeritus Professor Fusao Oka for his encouragement and invaluable advice. His positive attitude, patience, deep insight, constant support, and well-recognized experience in the field of study have guided my path of research. I will always be indebted to him not only for his support of my academic work and research, but also for his unconditional help in various aspects of my life in Japan.

It is also my great pleasure to show appreciation to Associate Professor Sayuri Kimoto for taking charge of my supervision after the retirement of Professor Oka. She never refused to share her time and support with me. Her attention and vast knowledge of the studied major proved to be very constructive to my research. Her outstanding experience in computational mechanics and constitutive modeling has been more than helpful.

I would next like to express my sincere appreciation to Professor Makoto Kimura and Professor Mamoru Mimura, members of the dissertation committee, for their valuable suggestions and active discussions as well as for their time and effort in reviewing this thesis.

Additionally, I have greatly benefited from friendly advice and help from Associate Professor Yosuke Higo, whom I would like to thank. I must also kindly express my appreciation to Ms. Chikako Itoh, Secretary of the Geomechanics Laboratory, who was kind enough to help me with matters of my daily life and official works during my period of stay in Japan.

Special thanks are extended to my friend Dr. Babak Shahbodaghkhan, former PhD Student of the Geomechanics Laboratory and current Assistant Professor at the University of New South Wales, Sydney, Australia; his support and friendly assistance did not stop even after his graduation.

I would like to express my appreciation to other students of our laboratory for their friendship, assistance and support. The time and joy that I shared with my friends Dr. Chung-Won Lee and Mr. Kensuke Noma will never be forgotten. Sincere thanks are also due to Mr. Hiromasa Iwai, doctoral student of the Geomechanics Laboratory, for his help and support during my study. Let my honest thanks also be extended

to Mr. Tatsuya Doi, Mr. Kazuki Saimyou, Mr. Yasuhiro Morimoto, Mr. Toshifumi Akaki, Mr. Ryoichi Morishita, and Mr. Hirokazu Yui who never refused to help me with Japanese language and daily issues.

The financial support provided by the Japan Ministry of Education, Science and Culture, Government of (MEXT), which made this study possible, is also recognized and greatly appreciated.

I also remember the help and support of Ms. Rama Rezvani during my studies and I appreciate her assistance. Finally, my most deeply felt gratitude goes to my parents and my brother in Iran for all their unchanging love, support, and faith throughout my life, entirely and particularly during my residence in Kyoto.

Table of Contents

List of Figures

List of Tables

Chapter 1

Introduction

1.1. Damage Patterns of River Embankments

River and road embankments play major roles in transportation and flood control in all countries. However, these important infrastructures are often subjected to earthquake damage. Settlement and spreading brought about by earthquakes and the induced liquefaction can cause severe levels of damage to or the failure of embankments. Based on the type of earthquake, the formation of subsoil layers, the dimensions of the embankment, and the mechanical properties of the materials in the body and the sublayers, numerous patterns of deformation and failure are possible for any given embankment. Above all this, the deformation-failure modes assumed in conventional engineering practice are still basic problems.

Many researchers have reported their observations of damage patterns to river embankments due to earthquakes. Sasaki et al. (1994) reported various failure modes in dikes and road embankments based on their observations of embankment failures due to the 1993 Kushiro-Oki Earthquake which hit the eastern part of Hokkaido, Japan.

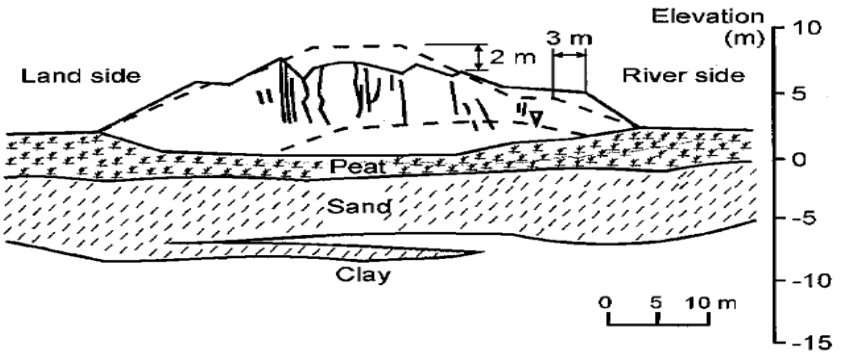

Figure 1.1. Kushiro River dike failure (Sasaki et al., 1995)

The failure mechanism illustrated in Figure 1.1. was adopted by Sasaki et al. (1995). The embankment body was up to 2.5 m below the groundwater level.

Sasaki et al. reported that typical damage to river facilities in Hokkaido consisted of dike failure, revetment failure, and sluice damage. Their main idea, however, was to report new failure modes followed by examples of severely damaged embankments along the Kushiro & Tokachi Rivers.

Sasaki et al. (1994, 1995) explained that the failure mechanism was due to the water trapped inside the embankment body, which was higher than the ground level, and to the location of the embankment bottom, which was below the water table.

The former may have been caused by water that seeped into the dikes from the surface and was trapped in there, while the latter may have occurred when the bottom of the embankment settled into the lower compressible or soft foundation layer (i.e., loose sand & soft peat).

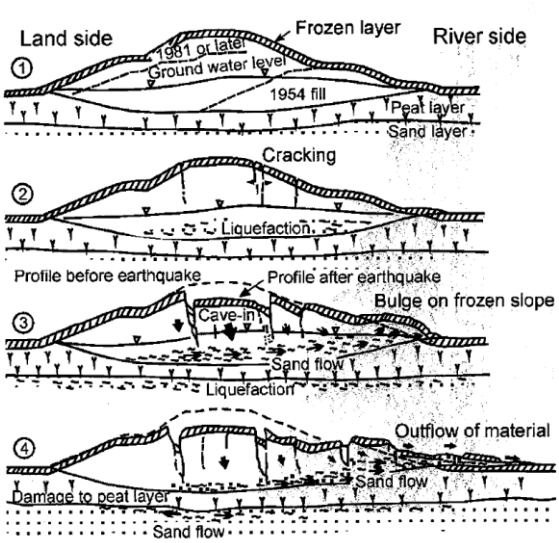

Figure 1.2. Mechanism of embankment failure (Kaneko et al., 1995)

Earthquake motion triggered cracking in the crest and liquefied the saturated embankment material. The slopes slid towards the river on the liquefied material, and the crest settled severely. Cracks in the frozen surface layer allowed an outflow of liquefied material from the toe. The settlement of the crest in this case was 2.5 m. Sasaki et al. especially emphasized that with such a mechanism, the failure mode is not circular, but that the cracks face the inside or the center of the embankment.

Sasaki et al. (1995) concluded that when an embankment is unexpectedly saturated or when it settles inside the foundation, the damage can be severe. Sasaki et al. (2012) also reported that one of the major causes of failure in the embankments due to the 2011 off the Pacific Coast of Tohoku Earthquake was the liquefaction in the foundation.

In agreement with Sasaki et al.'s findings, Harder et al. (2011) also reported that in the 2011 off the Pacific Coast of Tohoku Earthquake, the most severe damage to embankments was seen at the time of the earthquake in sections with continuous liquefiable layers in the foundation or ones with compressible soft foundations, which allowed the lower portion of the liquefiable sandy embankment fills to settle into the ground below a shallow water table and become saturated. For the sites damaged by the 1993 Kushiro-Oki Earthquake, Kaneko et al. (1995) also pointed out the effect of the water-saturated region in the levee on the behavior during the earthquake, as seen in Figure 1.2.

Figure 1.3. Major slumping of landside slope of Naruse River dike at river kilometer 30 (Harder et al., 2011)

Harder et al. explained that in some reaches (i.e., Naruse River), major damage ascribed to foundation liquefaction had been seen, i.e., Figure 1.3. The liquefaction was thought to have developed in either the foundation sands or the lower portions of a sandy levee embankment that had settled significantly into a clay foundation and had been saturated by groundwater. At several sites, groundwater on the landward side of the levee appeared to be significantly higher than the water level in the river, indicating groundwater flow towards the river.

Finn et al. (2000) tried to explain the mechanical reasons for the failure mechanism suggested by Sasaki et al. and proposed geometric criteria for the prediction of settlement in dikes against seismic liquefaction. Their simple criteria include the dike's height, the side slopes, and the thickness of both the liquefiable layer and the overlaying foundation layer. Towhata (2008) presented a classification for the seismic behavior of slopes and embankments with several examples of surface sliding, slump, and vertical

cracks. He also offered useful statistical data on the relationship between damage type and the subsidence to height ratio of several embankments.

Oka et al. (2012) reviewed the main causes and patterns of river embankment damage in the 2011 off the Pacific Coast of Tohoku Earthquake with a complete report and examples of river dike failures in many regions based on the *in situ* research carried out by the authors, MLIT (Ministry of Land, Infrastructure, Transport and Tourism), and JICE (Japan Institute of Construction Engineering (2011)).

Eai River embankment: Oka et al. (2012) reported that the most severely damaged dike was the left embankment of the Eai River (27.2–27.8 km) in the Fuchishiri District of Osaki City, Miyagi Prefecture (Figure 1.4). A sum of 400 m of the left dike was damaged with several large cracks at the crest, which was deformed in a wavy pattern with a maximum crest settlement of 0.83 m. The failed embankment blocks had moved laterally toward the river side with a maximum lateral movement of 9.37 m. The lower part of the embankment was composed of loose sandy soil with an N value of less than 10. This failure pattern is similar to Pattern 6 in Figure 1.6.

Figure 1.4. Left embankment at Fuchishiri-jyoryu of the Eai River (27.6 km).
(Courtesy of Kitakamigawa-Karyu River Office Tohoku Regional Bureau of MLIT, 2011).

The embankment at 27.6 km is underlain by soft deposits consisting of, from top to bottom, a 2-m clayey sandy layer (Acs) and two soft clay layers (Ac1 and Ac2) with a thin sandy layer (As1) (Ac1(1.5 m)+As1(0.5 m)+ Ac2(10m)) having a thickness of 12 m; the N value of the Acs layer is about 5–11. Beneath the clay layers, there is another sandy layer (As2) with a thickness of 4.5 m, and the N value

varies with depth from 10 to 40 m. The undrained strength of Ac1 and Ac2 is 16 kPa. For Acs, D_{50} is around 0.085–0.25 mm and D_{10} is 0.005–0.009 mm; Ip <=5. The D_{50} of embankment B_{s0} is 0.22 m and the Fc is about 25%. As2 is underlain by a rather stiff sandy layer with clay, Ds1, and an N value of more than 10.

Naruse River embankment: Also mentioned by Oka et al. (2012) was the failure that occurred to the right embankment of the Naruse River. River dikes of the Naruse River were also severely damaged and failed at seven sites, namely, the left embankment (29.7–30.1 km) in the Shimonakanome-jyouryuu District, the right embankment (29.7–30.1 km) in the Shimoibano District, the left embankment (29.0–29.1 km) in the Shimogawara District, the left embankment (20.1–20.3 km) in the Wadanuma District, the right embankment (11.9–12.0 km) in the Komazuka District, the left embankment (11.3–11.5 km) in the Sunayama District, and the right embankment (0–0.4 km) in the Nobiru District. The number of middle-level damaged sites is 121.

As seen in Figure 1.5, the settled crest and the interior inclined cracks resemble the failure mechanism presented by Sasaki et al. (1994).

Figure 1.5. Naruse River right bank, Fukunuma (Oka et al., 2012)

Along with the report of observations, Oka et al. (2012) used an infinitesimal strain analysis method to analyze four simplified most frequent cases of embankments with different formations in the foundation. Their results agreed with Sasaki et al.'s report; they also proved that long duration earthquakes can be significantly different from short duration ones in terms of damage patterns and total settlement. Although the results show a good qualitative agreement with what has occurred in the field, it

seems that the infinitesimal strain analysis method is not absolutely reliable for post-liquefaction periods or following large deformations. Moreover, some minor modifications to the dimensions of the assumed sublayers seem necessary. Better horizontal boundary conditions would yield better results.

Sadeghi et al. (2013) showed the importance of the subsoil clay's stiffness on the failure mode of an embankment using a viscoplastic model for clay. They also proved how easily the foundation's mechanical properties can affect the failure mode of two embankments with identical dimensions subjected to the same input accelerations.

This aim of this part of the research is to obtain different failure modes in river embankments using the finite deformation (FD) formulation. For that, and also for the sake of comparing the results of finite deformation and infinitesimal strain analysis methods considering liquefaction, the same four simplified cases of embankments with different formations used by Oka et al. (2012) were modeled applying elasto-viscoplastic materials for clay and elasto-plastic materials for sand. To ensure a better numerical simulation, equal displacement horizontal boundary conditions were employed.

1.2. Patterns of Failure in River Embankments

As previously mentioned, several modes of failure can be assumed for embankments. However, summarizing them into simplified groups will result in the patterns of damage shown in Figure 1.6.

In this figure, Pattern 1 represents shallow circular sliding, a sort of slight and recoverable damage that happens when the earthquake is not too strong and the foundation does not settle too much. Shallow sliding is minor damage to any embankment and can be easily repaired.

Pattern 2 represents the deep circular sliding failure mode. In this mechanism, sliding slices are long enough to reach the foundation. Figure 1.7 shows an example of this failure mode which was caused by the 2007 Pisco Earthquake in Peru. Patterns 1 and 2 are the usual modes of failure considered in common geotechnical engineering practice.

Pattern 3 shows the settlement of an embankment with a heaving of the toe. This generally occurs but is not limited to embankments on stiff or incompressible foundations. This can also even happen to embankments on loose or compressible foundations, provided that short duration earthquakes do not cause liquefaction. No apparent tension cracks can be seen with this mode of failure, since the embankment body is compressed.

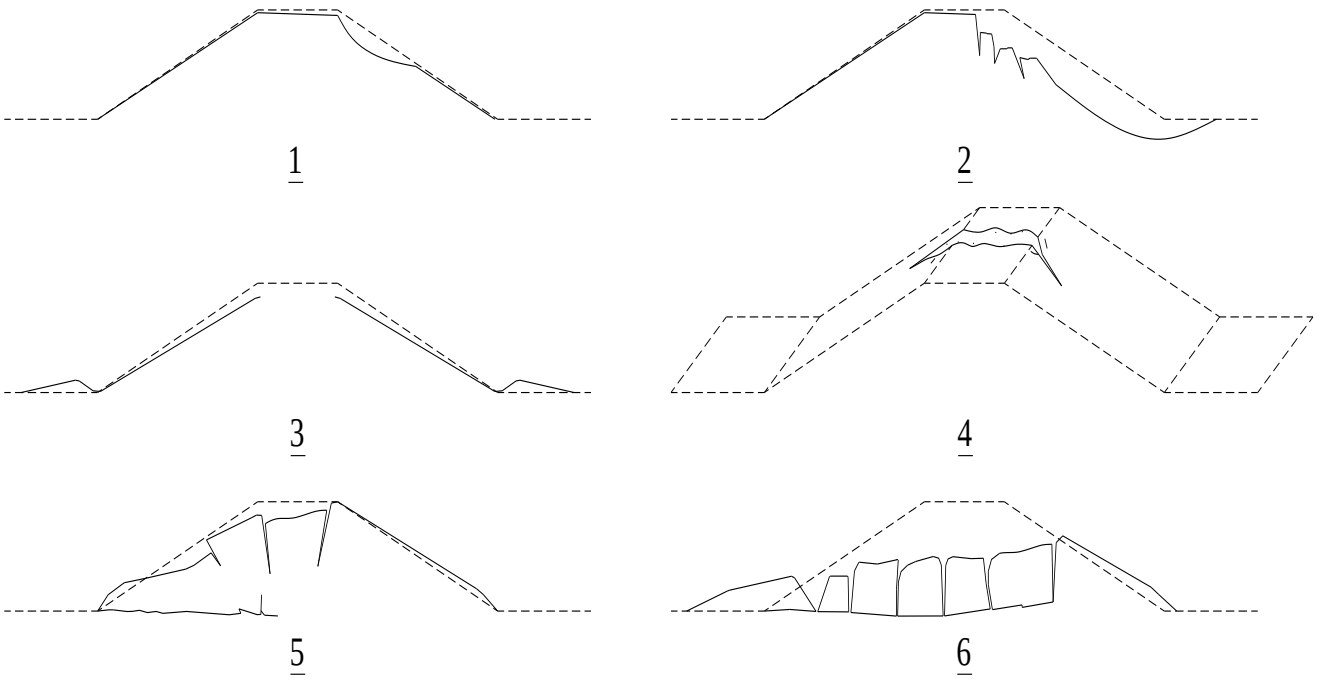

Figure 1.6. Different patterns of failure in embankments

Figure 1.7. Deep sliding of road embankment in 2007 Pisco Earthquake, Peru (Photo credit: Ing. Jack Lopez)

Pattern 4 depicts transversal cracks and fissures in the length of the embankment. This mode can be brought about by transverse asynchronous excitations along the embankment i.e., Figure 1.8.

Pattern 5 happens when the soil foundation loses its strength due to liquefaction and allows for excessive settlements of the embankment crest and shoulders. Lateral expansion of the embankment toe, which leads to tension fields in the body and the settlement of the crest, create longitudinal cracks in the embankment body. Although liquefaction of the foundation is a major reason for this behavior, highly compressible and soft materials can also lead to the same state even without the occurrence of liquefaction.

Figure 1.8. Eai River right bank, Fukunuma (Oka et al., 2012)

Pattern 6 shows one of the most severe types of damage that can occur to embankments due to earthquake-induced liquefaction. Lateral expansion of the toe and lateral movement of the embankment slopes, caused by a loosened, liquefied or excessively settled soft foundation, create fissured blocks in the embankment body with large settlements, i.e., Figure 1.5.

1.3. Objectives and Scope of Work

The main objective of the present research is to study the failure mechanisms of river embankments during earthquakes considering liquefaction. The damage patterns that have been discussed thus far, although seen in many fields, have not yet been fully studied with numerical methods. The reason is the complex behavior of soils and earth structures during earthquakes and especially after liquefaction.

Depending on the frequency content, the magnitude, the duration, the distance from the origin, the site conditions, and other factors, earthquakes have different effects on different structures. Moreover, the

various possible ground profiles and formations of earth structures, i.e., road and river embankments, make it difficult to predict the failure mode that will occur.

In this thesis, using suitable constitutive models and a finite deformation coupled formulation, the dynamic behavior of river embankments is studied. The main focus is on the possible deformation- failure patterns that may occur to an embankment. For this purpose, several ground profiles and different earthquake motions are analyzed.

It is also important to pay attention to the basic issues involved in the numerical analysis of embankments. Thus, we also present the results of a study on the differences between infinitesimal and finite deformation methods in the dynamic analysis of embankments. An outline of the present study is given as follows:

Chapter 1, the current chapter, presents the main purposes of this doctoral study, along with a discussion and background information on different failure patterns in river embankments.

Chapter 2 is dedicated to the introduction of the cyclic constitutive models used in this analysis. The elasto-viscoplastic model applied for the analysis of clayey materials and the elasto-plastic model applied for the analysis of sandy soils are presented in this chapter. It ends with the results of numerical test simulations performed on the materials employed in this study.

Chapter 3 deals with the dynamic finite deformation formulation of an analysis for multiphase materials. It continues with the introduction of code COMVI2D-DY that has been developed based on this formulation for the coupled dynamic analysis of soil and geotechnical structures.

Chapter 4 presents the main results of this study. It contains the different ground profiles and earthquake wave inputs that have been assumed for studying the dynamic behavior of river embankments during earthquakes including liquefaction. This chapter shows the results of the numerical dynamic large deformation analysis performed in the study and discusses the new findings.

Chapter 5 deals with the basic concepts of the dynamic analysis of river embankments. It presents a comparison between the results of the infinitesimal strain and the finite deformation methods. For the comparison, an embankment lying over liquefiable soil is subjected to an earthquake and its results are discussed.

Chapter 6 presents the concluding remarks and a summary of the present study with suggestions for future works.

Chapter 2

Constitutive Models for Cyclic Behavior of Soils

2.1. Introduction

This chapter is dedicated to details on the constitutive models used in this research. The constitutive model used for the sandy materials is an elasto-plastic (EP) cyclic model, while that employed for the clayey materials is an elasto-viscoplastic (EVP) model. Details on the above-mentioned models and the results of test simulations are presented herein.

2.2. Cyclic Elasto-viscoplastic Model for Clay

2.2.1. Introduction

The importance of the time-dependent behavior of soils is well-known in geotechnical engineering. It is also evident that clay in particular shows dissimilar stress-strain behavior for different strain rates. Thus far, many researchers have tried to bring this behavior into a formulation, i.e., Adachi and Oka (1982), Kaliakin et al. (1990), and Kimoto and Oka (2005). However, fewer attempts have been made to model this behavior for cyclic loading, i.e., Oka (1992), Modaressi and Laloui (1997), Oka et al. (2004), and. Oka (1992) developed a cyclic elasto-viscoplastic constitutive model for clay based on the nonlinear kinematic hardening rule. Later on, Oka et al. (2004) proposed a cyclic viscoelastic-viscoplastic model by introducing viscoelasticity into the constitutive equations, in which the behavior of clay could be described for both low and high levels of strain.

Despite the ability of these models to explain the deformation characteristics under cyclic loading conditions, the effect of the structural degradation of clay particles was neglected. Taking structural degradation and microstructural changes into account, a cyclic elasto-viscoplastic model was developed based on the nonlinear kinematic hardening rule for changes in both the stress ratio and the mean effective stress (Hoizumi, 1996; Watanabe et al., 2007). In order to improve predictions of the behavior

during the cyclic loading process, the nonlinear kinematic hardening rule for changes in the viscoplastic volumetric strain was included in the model.

Many constitutive models have also been proposed for unsaturated soils, i.e., Alonso et al. (1990), Thomas and He (1998), and Oka et al. (2008). However, most of the suggested models have been derived within the framework of rate-independent models, such as elasto-plastic ones. Kim (2004) and Oka et al. (2010) investigated the time-dependent property of unsaturated soils with experiments. They illustrated the necessity of constructing a cyclic elasto-viscoplastic model for predicting the mechanical behavior of partially saturated soils.

In the present study, the cyclic elasto-viscoplastic constitutive model, created by Kimoto et al. (2013) and extended for partially saturated soils using the skeleton stress and suction effect in the constitutive model by Shahbodaghkhan (2011), which is an extended version of the model by Kimoto et al. (2007), is being used. The collapse behavior of unsaturated soil is totally independent of the stress variables adopted in the constitutive modeling (Schrefler et al., 1995; Oka, 1988; Jommi, 2000). In the model, the collapse behavior is described by the shrinkage of the overconsolidation boundary surface, the static yield surface, and the viscoplastic surface due to the decrease in suction. After presenting the constitutive model, element test simulations were conducted by the integration of the constitutive equations on soil specimens in cyclic triaxial tests.

2.2.2. Skeleton Stress in Partially Saturated Soil

Terzaghi (1936) introduced the effective stress concept to describe the deformation behavior of water-saturated soils. This concept was based on the results of experiments on the strength and deformation of such soils. Terzaghi's effective stress in a three-dimensional form is defined as

$$\sigma'_{ij} = \sigma_{ij} - u_w \delta_{ij} \tag{2-1}$$

in which σ' is the effective stress tensor, σ is the total stress tensor, u_w is the pore-water pressure, and δ_{ij} is Kronecker's delta. Equation (2-1) is only applicable to saturated soils with incompressible grains, while pore spaces are completely saturated with incompressible fluid.

Oka (1996) clarified the validity and the limits of the effective stress concept in geomechanics by describing the dependency of saturated soil behavior on both the balance of forces and the compressibility of the constituents.

Bishop (1960) proposed an effective stress equation for unsaturated soils as

$$\sigma'_{ij} = \left(\sigma_{ij} - u_a\delta_{ij}\right) + \chi\left(u_a - u_w\right)\delta_{ij} \tag{2-2}$$

where σ'_{ij} is the effective stress tensor or the Bishop stress tensor, σ_{ij} is the total stress tensor, u_a and u_w are the pore-air pressure and the pore-water pressure, respectively, δ_{ij} is Kronecker's delta, and χ is a constitutive material parameter ranging from zero for dry soils to 1.0 for saturated soils depending on the degree of saturation. The term $\sigma_{ij} - u_a\delta_{ij}$ is called net stress, and the term $\chi(u_a - u_w)$ represents the inter-particle effective stress due to capillary cohesion.

To reflect the collapse behavior of unsaturated soils, researchers have suggested the independent stress variable approach, in which two stresses are proposed for both the soil particles and the fluids, i.e., Bishop and Donald (1961) and Fredlund and Morgenstern (1977).

Meanwhile, using net stress and suction as the stress variables, it is very difficult to apply many constitutive models developed for saturated soils to unsaturated soils (Kohgo et al., 1993).

In this formulation, the fluid pressure contributions are linked to the respective volumetric fractions by

$$\sigma'_{ij} = \sigma_{ij} + P^F\delta_{ij}\ ,\ P^F = \left(1 - S_r\right)P^G + S_rP^W \tag{2-3}$$

where P^F is the average pressure of the fluids surrounding the soil skeleton; it is positive when the fluids are in compression. S_r is the degree of saturation, and P^G and P^W are the pore-gas pressure and the pore-water pressure, respectively.

In the present model, the skeleton stress and the suction are adopted as the basic stress variables. Suction is incorporated into the constitutive model to describe the collapse behavior of partially saturated soils. Skeleton stress is the same as the average soil skeleton stress by Jommi (2000) and the generalized effective stress by Laloui and Nuth (2009). However, the terminology used here is “skeleton stress”. The skeleton stress is consistent with the theory of mixture for multiphase materials.

2.2.3. Elastic Strain Rate

The total strain rate tensor is composed of two parts, namely,

$$\dot{\varepsilon}_{ij} = \dot{\varepsilon}^{e}_{ij} + \dot{\varepsilon}^{vp}_{ij} \tag{2-4}$$

where $\dot{\varepsilon}^{e}_{ij}$ denotes the elastic strain rate tensor and $\dot{\varepsilon}^{e}_{ij}$ is the viscoplastic strain rate tensor. Elastic strain rate tensor $\dot{\varepsilon}^{e}_{ij}$ can be broken down into

$$\dot{\varepsilon}^{e}_{ij} = \dot{e}^{e}_{ij} + \frac{1}{3}\dot{\varepsilon}^{e}_{v}\delta_{ij} \tag{2-5}$$

where $\dot{e}^{e}_{ij}$ is the deviatoric elastic strain rate tensor given by

$$\dot{e}^{e}_{ij} = \frac{1}{2G}\dot{S}_{ij} \tag{2-6}$$

in which S_{ij} is the deviatoric stress tensor given by

$$S_{ij} = \sigma'_{ij} - \sigma'_{m}\delta_{ij} \tag{2-7}$$

and G is the elastic shear modulus. Volumetric elastic strain rate tensor $\dot{\varepsilon}^{e}_{v}$ is given as

$$\dot{\varepsilon}^{e}_{v} = \dot{\varepsilon}^{e}_{11} + \dot{\varepsilon}^{e}_{22} + \dot{\varepsilon}^{e}_{33} \tag{2-8}$$

Volumetric elastic strain rate tensor $\dot{\varepsilon}^{e}_{v}$ follows the following relationship during the isotropic swelling process:

$$\dot{\varepsilon}^{e}_{v} = \frac{\kappa}{1+e}\frac{\dot{\sigma}'_{m}}{\sigma'_{m}} \tag{2-9}$$

where κ is the swelling index, σ'_{m} is the mean skeleton stress, and e is the void ratio. σ'_{m} denotes the mean skeleton stress given by

$$\sigma'_{m} = \frac{1}{3}\sigma'_{kk} \tag{2-10}$$

2.2.4. Strain Dependency of the Elastic Shear Modulus

The non-linearity of soil stiffness has been studied extensively for materials such as sand, clay, and gravel, and has been well summarized by Ishihara (1996). For cohesive soils, several empirical equations have been proposed by considering the dependency of the shear modulus on the effective confining stress (Kokusho et al., 1982). In the original configuration by Kimoto and Oka (2005), the change in the elastic shear modulus of the elasto-viscoplastic model is given by the square root function of the normalized mean skeleton stress as

$$G = G_0 \sqrt{\frac{\sigma'_m}{\sigma'_{m0}}} \tag{2-11}$$

in which G_0 is the initial shear modulus; it is definitely an important parameter in dynamic response analyses. It depends on the initial ratio and the initial confining stress and can be expressed empirically as

$$G_0 = Af\left(e_0\right)\left(\sigma'_{m0}\right)^n \tag{2-12}$$

where A and n are the material parameters and $f(e_0)$ is the function of initial void ratio e_0.

Equation (2-11) considers only the effect of the confining pressure, which can accurately approximate the variation in shear modulus at very small levels of strain. In problems concerned with large levels of strain, however, as demonstrated by the experimental results, the strain dependency of the shear modulus should be considered as well. Ogisako et al. (2007) have introduced a normalized shear modulus reduction function based on the viscoplastic shear strain in soft clay specimens and have proposed a hyperbolic equation for that expression, namely,

$$G = G_0\left(e_0\right)\frac{1}{\left(1+\alpha\left(\gamma^{vp}\right)^r\right)} \tag{2-13}$$

where α is the strain-dependent parameter, r is the experimental constant, and γ^{vp} is the accumulated viscoplastic shear strain given by an accumulation of the viscoplastic deviatoric strain rate as

$$\gamma^{vp} = \int \sqrt{de_{ij}^{vp} de_{ij}^{vp}} \tag{2-14}$$

2.2.5. Overconsolidation Boundary Surface

Overconsolidation boundary surface f_b is defined as the boundary between the normally consolidated (NC) region and the overconsolidated (OC) region by:

$$f_b = \bar{\eta}^*_{ij(0)} + M^*_m \ln\left(\frac{\sigma'_m}{\sigma'_{mb}}\right) = 0 \tag{2-15}$$

where $f_b < 0$ indicates the overconsolidated region and $f_b \geq 0$ shows the normally consolidated region. $\bar{\eta}^*_{ij}$ is the relative stress ratio defined as:

$$\bar{\eta}^*_{(0)} = \left\{\left(\bar{\eta}^*_{ij} - \bar{\eta}^*_{ij(0)}\right)\left(\bar{\eta}^*_{ij} - \bar{\eta}^*_{ij(0)}\right)\right\}^{\frac{1}{2}} \tag{2-16}$$

in which subscript (0) denotes the initial state before deformation and η^*_{ij} is the stress ratio tensor. σ'_{mb} is the hardening parameter, which controls the size of the OC boundary surface. M^*_m is the value for $\eta^* = \sqrt{\eta^*_{ij}\eta^*_{ij}}$ at the critical state when the volumetric strain increment changes from compression to dilation. This value is generally a function of Lode's angle, and any kind of failure criterion can be used, such as Mohr-Coulomb's failure criterion. Adopting Mohr-Coulomb's criterion, M^*_m is defined by friction angle ϕ. In conventional cyclic triaxial tests, the stress path follows the compression and the extension; hence, we can characterize the failure under the triaxial cyclic tests by the stress ratio at triaxial compression failure state M^*_{mc} and the stress ratio at extension failure state M^*_{me}. If the material follows the Mohr-Coulomb criterion, M^*_m is related to internal frictional angle ϕ as

$$M^*_{mc} = \sqrt{\frac{2}{3}}\frac{6\sin\phi}{3-\sin\phi} \quad , \qquad M^*_{me} = \sqrt{\frac{2}{3}}\frac{6\sin\phi}{3+\sin\phi} \tag{2-17}$$

However, we determined M^*_{mc} and M^*_{mc} directly from the experimental results because it is not necessary to identify the failure criterion at this stage. Naturally, we have to use a specific criterion for solving boundary value problems.

For sand, due to material anisotropy, the method of sample preparation, the degree of compaction, aging, etc., the initial values for σ'_{mb} and σ'_{mbi} are not always equal to initial mean skeleton stress σ'_{m0}. Therefore, it is appropriate to define the quasi-overconsolidation ratio as

$$OCR'^{*} = \frac{\sigma'_{mbi}}{\sigma'_{m0}} \tag{2-18}$$

The overconsolidation boundary surface described in Equation (2-14) can be written in the triaxial stress state as follows:

$$f_b = \left| \frac{q}{\sigma'_m} - \frac{q}{\sigma'_{m0}} \right| + M^*_m ln \frac{\sigma'_m}{\sigma'_{mb}} = 0 \tag{2-19}$$

in which q is the deviator stress ($q = \sigma'_{11} - \sigma'_{33}$), $\sigma'_{22} = \sigma'_{33}$. In order to describe the structural degradation of natural clay, strain-softening with viscoplastic strain is introduced into the hardening parameter in addition to strain hardening with the viscoplastic volumetric strain. Meanwhile, to describe the suction effect, it is included in the value of σ'_{mb} as

$$\sigma'_{mb} = \sigma'_{mau} \exp\left(\frac{1+e}{\lambda - \kappa} \varepsilon^{vp}_{kk} \right) \tag{2-20}$$

$$\sigma'_{mau} = \sigma'_{ma} \left[1 + S_I \exp\left\{ -s_d \left(\frac{P^C_i}{P^C} - 1 \right) \right\} \right] \tag{2-21}$$

where ε^{vp}_{kk} is the viscoplastic volumetric strain, λ and κ are the compression and the swelling indexes, respectively, and e_0 is the initial void ratio. σ'_{ma} is a strain-softening parameter used to describe the structural degradation effect, which is assumed to decrease with an increase in viscoplastic strain, namely,

$$\sigma'_{ma} = \sigma'_{maf} + \left(\sigma'_{mai} - \sigma'_{maf} \right) \exp\left(-\beta z \right) \tag{2-22}$$

where z is the accumulation of the second invariant of the viscoplastic strain rate defined as

$$z = \int_0^t \dot{z} dt \quad \text{in which } \dot{z} = \sqrt{\dot{\varepsilon}^{vp}_{ij} \dot{\varepsilon}^{vp}_{ij}} \tag{2-23}$$

In Equation (2-21), S_I is the strength ratio of unsaturated soils when the value for suction P^C equals P_i^C, and S_d controls the decreasing ratio of strength with decreasing suction. The term P_i^C is set to be the initial value of suction. At the initial state, when $P^C = P_i^C$, the strength ratio of the unsaturated soil to the saturated soil is $1+S_I$ and it decreases with a decline in suction. The change in hardening parameter with the change in suction and the effect of parameter S_d is shown in Figure 2.1.

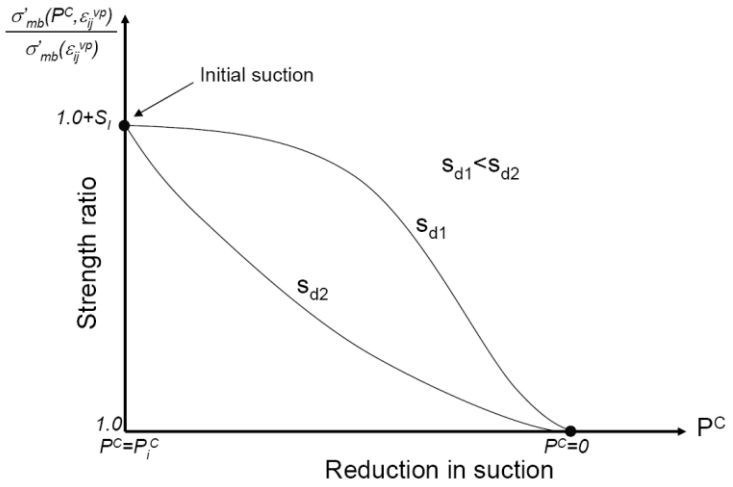

Figure 2.1. Strength degradation due to the reduction in suction

In Equation (2-22), σ'_{mai} and σ'_{maf} are the initial and the final values for σ'_{ma}, respectively, β is a material parameter controlling the rate of structural changes, and z is the accumulation of the second invariant of viscoplastic strain rate ε_{ij}^{vp}. Since the viscoplastic strain is equal to zero at the initial state, we can obtain a consolidation yield stress for σ'_{mbi} equal to $\sigma'_{mai}(1+S_I)$.

2.2.6. Static Yield Function

The static yield function is obtained by considering the nonlinear kinematic hardening rule for changes in the stress ratio, the mean effective stress, and the viscoplastic volumetric strain, as

$$f_y = \bar{\eta}^*_{(x)} + \tilde{M}^* \left(\ln \frac{\sigma'_{mk}}{\sigma'^{(s)}_{my}} + \left| \ln \frac{\sigma'_m}{\sigma'_{mk}} - y^*_{m1} \right| \right) = 0 \qquad (2\text{-}24)$$

$$\bar{\eta}_{\chi}^{*} = \left\{ \left(\eta_{ij}^{*} - \chi_{ij}^{*} \right) \left(\eta_{ij}^{*} - \chi_{ij}^{*} \right) \right\}^{\frac{1}{2}} \tag{2-25}$$

in which σ'_{mk} is the unit value of the mean effective stress, y_{m1}^{*} is the scalar kinematic hardening parameter, and $\sigma_{my}^{\prime(s)}$ denotes the static hardening parameter. χ_{ij}^{*} is the back stress parameter, which has the same dimensions as stress ratio η_{ij}^{*}. Incorporating strain softening for the structural degradation, the hardening rule can be expressed as

$$\sigma_{my}^{\prime(s)} = \frac{\sigma'_{mau}}{\sigma'_{mai}} \sigma_{myi}^{\prime(s)} \tag{2-26}$$

Note that Equation (2-26) is different from the one presented by Sawada (2008). In Sawada's formulation, the hardening rule for $\sigma_{my}^{\prime(s)}$ includes the effect of volumetric strain twice (Mirjalili, 2010). Hence, it has been modified in the current formulation by replacing σ'_{mb} with σ'_{mau}.

2.2.7. Viscoplastic Potential Function

In the same manner as for the static yield function, viscoplastic potential function f_P is given by

$$f_p = \bar{\eta}_{\chi}^{*} + \tilde{M}^{*} \left(ln \frac{\sigma'_{mk}}{\sigma'_{mp}} + \left| ln \frac{\sigma'_{m}}{\sigma'_{mk}} - y_{m1}^{*} \right| \right) = 0 \tag{2-27}$$

Dilatancy coefficient $\tilde{M}^{*}$ is defined separately for the normally consolidated region (NC) and the overconsolidated region (OC) as

$$\tilde{M}^{*} = \begin{cases} \tilde{M}_{m}^{*} & : \text{NC Region} \\ \left(\dfrac{\sigma_{m}^{*}}{\sigma'_{mc}} \right) \tilde{M}_{m}^{*} & : \text{OC Region} \end{cases} \tag{2-28}$$

where σ'_{mc} is the mean effective stress at the intersection of the overconsolidation boundary surface and the σ'_{m} axis, which is defined by

$$\sigma'_{mc} = \sigma'_{mb} \exp\left(\frac{\sqrt{\eta^*_{ij(0)} \eta^*_{ij(0)}}}{\tilde{M}^*_m} \right) \tag{2-29}$$

In addition, σ^*_m denotes the mean effective stress at the intersection of the surface, which has the same shape as f_b, and is given by

$$\sigma^*_m = \sigma'_m \exp\left(\frac{\bar{\eta}^*_\chi}{M^*_m} \right) \tag{2-30}$$

The effect of the decrease in suction on the shrinkage of the overconsolidation boundary surface, f_b, the static yield function, f_y, and the viscoplastic potential function, f_p, for $\eta^*_{ij(0)} = 0$, is illustrated schematically in the $\sigma'_m - \sqrt{2J_2}$ space (Figure 2.2). It can be seen that σ'_{mb} and $\sigma'^{(s)}_{my}$ decrease with decreasing suction due to wetting. The increments in viscoplastic strain for the overstress type of model depend on the difference between the current stress state and the static yield stress state. Therefore, the shrinkage of f_y due to wetting, is yielded in the viscoplastic strain increments.

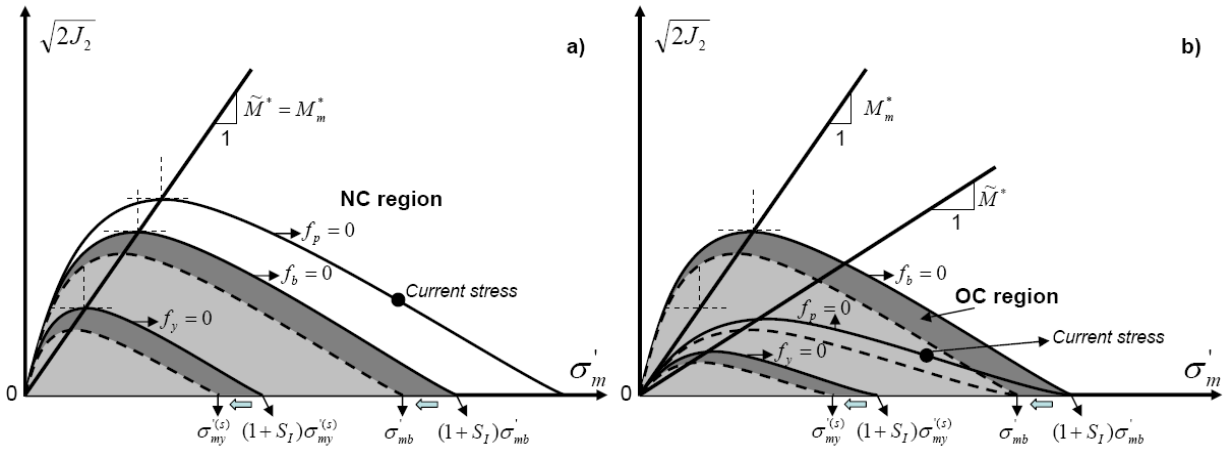

Figure 2.2. Shrinkage of the OC boundary surface, static yield function and potential function a) In the NC region, b) In the OC region

2.2.8. Kinematic Hardening Rule

The evolution equation for the nonlinear kinematic hardening parameter χ_{ij}^{*} is given by

$$d\chi_{ij}^{*} = B^{*}\left(A^{*}de_{ij}^{vp} - \chi_{ij}^{*}d\gamma^{vp}\right) \tag{2-31}$$

where A^{*} and B^{*} are material parameters, de_{ij}^{vp} is the viscoplastic deviatoric strain increment tensor, and $d\gamma^{vp} = \int\sqrt{de_{ij}^{vp}de_{ij}^{vp}}$ is the viscoplastic shear strain increment tensor. A^{*} is related to the stress ratio at failure, namely, $A^{*} = M_{f}^{*}$, and B^{*} is proposed to be dependent on the viscoplastic shear strain as

$$B^{*} = \left(B_{max}^{*} - B_{1}^{*}\right)\exp\left(-C_{f}\gamma_{(n)}^{vp*}\right) + B_{1}^{*} \tag{2-32}$$

in which B_{1}^{*} is the lower boundary of B^{*}, C_{f} is the parameter controlling the amount of reduction, and $\gamma_{(n)r}^{vp*}$ is the accumulated value of the viscoplastic shear strain between two sequential stress reversal points in the previous cycle. B_{max}^{*} is the maximum value for parameter B^{*}, proposed by Oka et al. (1999) as

$$B_{max}^{*} = \begin{cases} B_{0}^{*} & : \text{Before reachning failure line} \\ \dfrac{B_{0}^{*}}{1 + \dfrac{\gamma_{(n)max}^{vp*}}{\gamma_{(n)r}^{vp*}}} & : \text{After reachning failure line} \end{cases} \tag{2-33}$$

in which B_{0}^{*} is the initial value for B^{*}, $\gamma_{(n)max}^{vp*}$ is the maximum value for $\gamma_{(n)}^{vp*}$ in past cycles, and $\gamma_{(n)r}^{vp*}$ is the viscoplastic reference strain. In order to improve the predicted results under cyclic loading conditions, scalar nonlinear kinematic hardening parameter y_{m1}^{*} is introduced as

$$dy_{m1}^{*} = B_{2}^{*}\left(A_{2}^{*}de_{v}^{vp} - y_{m1}^{*}\left|d\varepsilon_{v}^{vp}\right|\right) \tag{2-34}$$

where A_2^* and B_2^* are material parameters, and $d\varepsilon_v^{vp}$ is the increment in viscoplastic volumetric strain. The values for A_2^* and B_2^* are determined by a data-adjusting method from the laboratory test data. The relation between scalar nonlinear kinematic hardening y_{m1}^* and viscoplastic volumetric strain $d\varepsilon_v^{vp}$ is shown in Figure 2.3.

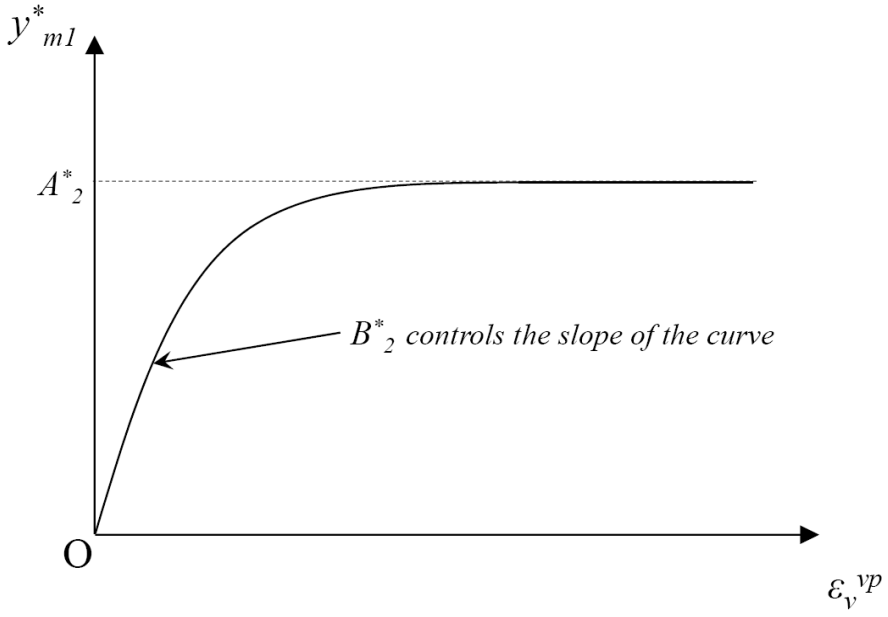

Figure 2.3. Scalar nonlinear kinematic hardening function y_{m1}^*

2.2.9. Viscoplastic Flow Rule

Based on the overstress type of viscoplastic theory, initially adopted by Perzyna (1963), the viscoplastic strain rate tensor is defined as

$$\dot{\varepsilon}_{ij}^{vp} = C_{ijkl}\left\langle \Phi\left(f_y\right)\right\rangle \frac{\partial f_p}{\partial \sigma'_{kl}} \tag{2-35}$$

$$\left\langle \Phi\left(f_y\right)\right\rangle = \begin{cases} \Phi\left(f_y\right) & : f_y > 0 \\ 0 & : f_y \le 0 \end{cases} \tag{2-36}$$

$$C_{ijkl} = a\delta_{ij}\delta_{kl} + b\left(\delta_{ik}\delta_{jl} + \delta_{il}\delta_{jk}\right) \tag{2-37}$$

where $\langle\ \rangle$ are Macaulay's brackets, $\Phi\left(f_y\right)$ is the rate-sensitive material function, and C_{ijkl} is a fourth order isotropic tensor. a and b in Equation (2-37) are material constants. Material function $\Phi\left(f_y\right)$ is determined as

$$\Phi\left(f_y\right)=\sigma'_m\ \exp\left\{m'\left(\bar{\eta}^*_\chi+\tilde{M}^*\left(ln\frac{\sigma'_{mk}}{\sigma'_{mau}}+\left|ln\frac{\sigma'_m}{\sigma'_{mk}}-y^*_{m1}\right|\right)\right)\right\} \tag{2-38}$$

in which m' is the viscoplastic parameter. Finally, by adding Equation (2-36) to Equation (2-39), viscoplastic deviatoric strain rate $\dot{e}^{vp}_{ij}$ and viscoplastic volumetric strain rate $\dot{\varepsilon}^{vp}_v$ can be expressed as

$$\dot{\varepsilon}^{vp}_{ij}=C_1\ \exp\left\{m'\left(\bar{\eta}^*_\chi+\tilde{M}^*\left(\ln\frac{\sigma'_{mk}}{\sigma'_{mau}}+\left|\ln\frac{\sigma'_m}{\sigma'_{mk}}-y^*_{m1}\right|\right)\right)\right\}\frac{\eta^*_{ij}-\chi^*_{ij}}{\bar{\eta}^*_\chi} \tag{2-39}$$

$$\dot{\varepsilon}^{vp}_v=C_2\ \exp\left\{m'\left(\bar{\eta}^*_\chi+\tilde{M}^*\left(\ln\frac{\sigma'_{mk}}{\sigma'_{mau}}+\left|\ln\frac{\sigma'_m}{\sigma'_{mk}}-y^*_{m1}\right|\right)\right)\right\}\left\{\tilde{M}^*\frac{\ln\frac{\sigma'_m}{\sigma'_{mk}}-y^*_{m1}}{\left|\ln\frac{\sigma'_m}{\sigma'_{mk}}-y^*_{m1}\right|}-\frac{\eta^*_{mn}\left(\eta^*_{mn}-\chi^*_{mn}\right)}{\bar{\eta}^*_\chi}\right\} \tag{2-40}$$

in which $C_1=2b$ and $C_2=3a+2b$ are the viscoplastic parameters for the deviatoric and the volumetric strain components, respectively.

2.2.10. Results of Test Simulations

In this section, the results of cyclic triaxial test simulations performed on Torishima clay are presented. Table 2.1 shows the material properties used for this analysis.

The parameters presented here for clay, which are used for the dynamic analysis of embankments in the next chapters, are determined considering the difference between the viscoplastic parameters based on the values measured in the laboratory at Torishima, Osaka and those measured in the field, i.e., Leroueil et al. (1983).

Simulations were performed for different cyclic stress ratio (CSR) values. Shown in Figure 2.4 is the cyclic strength curve for the Torishima clay used in this study.

Figure 2.5 shows the deviator stress versus mean effective stress along with the deviator stress versus axial strain results for the triaxial test simulations. The figure also shows the excess pore-water pressure (Excess PWP) versus the number of cycles for the cyclic stress ratio=0.55.

Table 2.1. Material Parameters of Torishima Clay

	Elasto-viscoplastic Clay
Density $\rho(t/m^3)$	1.66
Water specific weight γ_w (kn/m3)	9.81
Coefficient of permeability K^w_s (m/s)	5.87×10^{-10}
Initial void ratio e_0	1.25
Compression index λ	0.341
Swelling index κ	0.019
Initial elastic shear modulus ratio G_0/σ'_{m0}	400
Stress ratio at critical state M^*_m	1.24
Hardening parameters B^*_0, B^*_1, C_f	500,100,5
Structural parameters n, β	0.30,3.6
Dilatancy parameters D^*_0, n	
Viscoplastic parameter m'	24.68
Viscoplastic parameter C_1(1/s)	1.00×10^{-11}
Viscoplastic parameter C_2(1/s)	3.83×10^{-12}
Scalar hardening parameters A^*_2, B^*_2	5.9,1.8
Strain-dependent parameters α', r	10,0.4

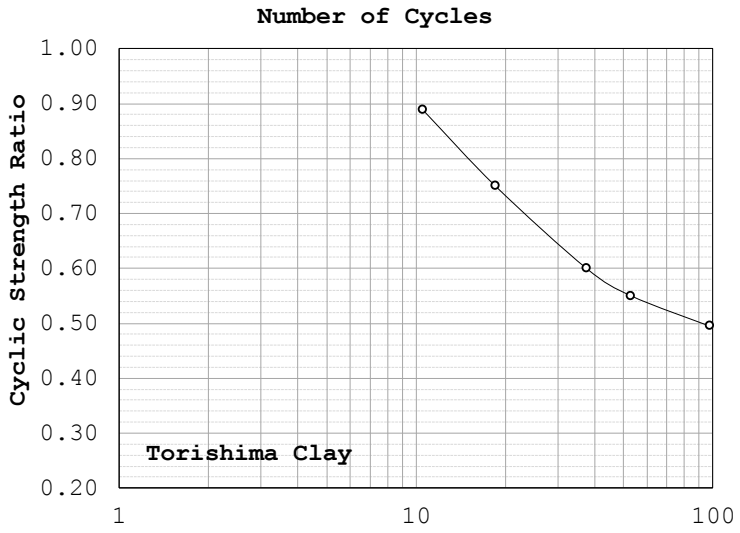

Figure 2.4. Cyclic strength curve of Torishima Clay

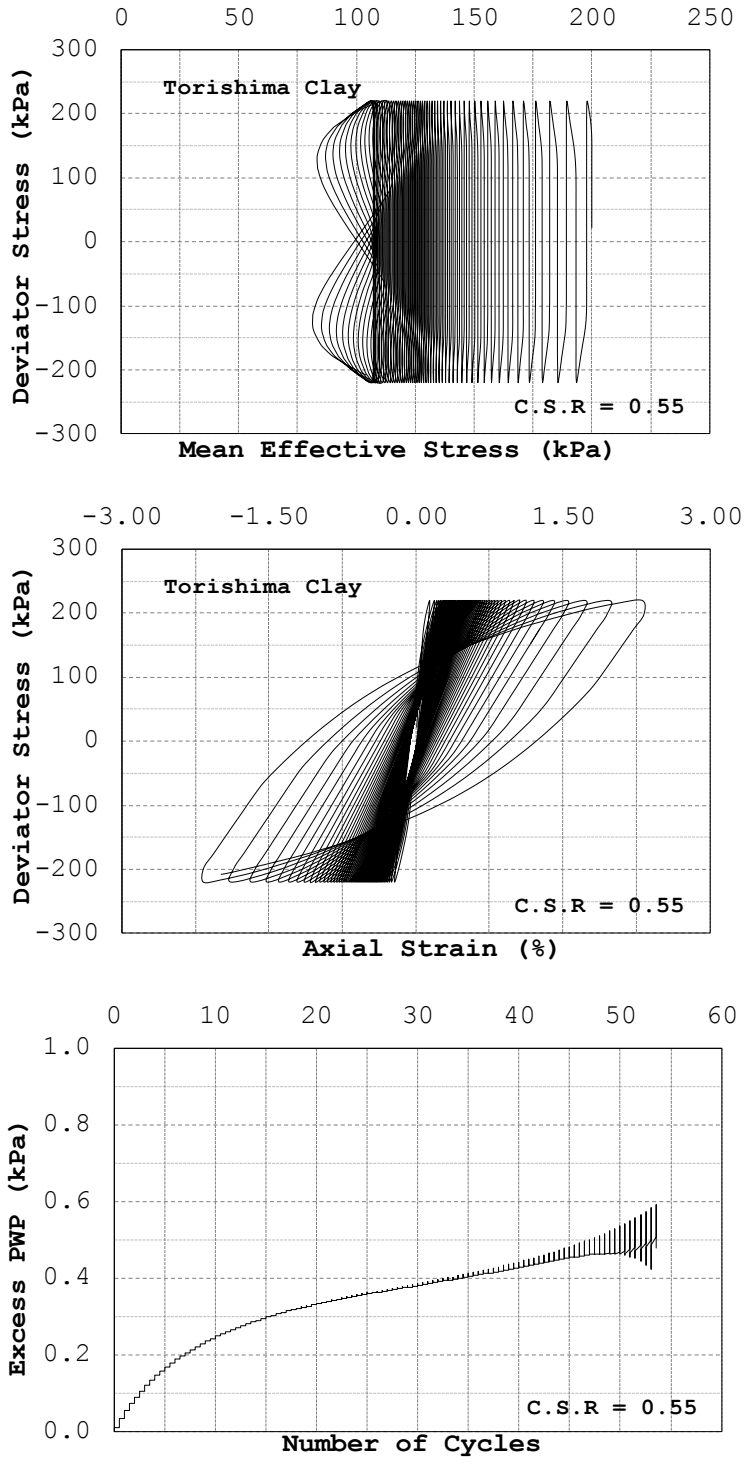

Figure 2.5. Results of cyclic triaxial test simulations on Torishima clay for C.S.R = 0.55 and 53 cycles

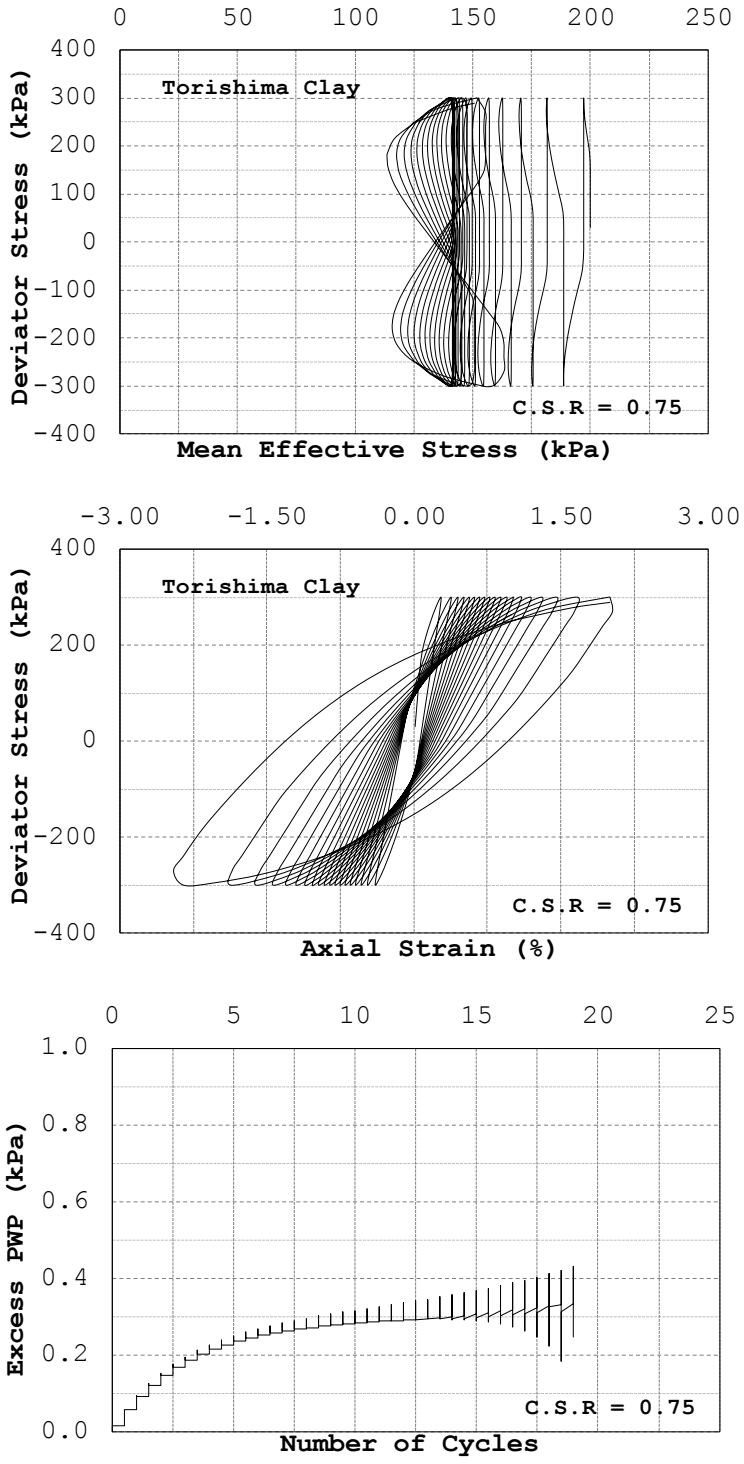

Figure 2.6. Results of cyclic triaxial test simulations on Torishima clay for C.S.R = 0.75 and 18.5 cycles

2.3. Cyclic Elasto-plastic Model for Sand

2.3.1. Introduction

This section presents the cyclic elasto-plastic model used for sand. This model has been developed based on the nonlinear kinematic hardening rule by Oka et al. (1999).

The following assumptions have been made in the formulation of this model:

- Elasto-plastic theory
- Non-associated flow rule
- Overconsolidation boundary surface
- Nonlinear kinematic hardening
- Degradation of shear modulus with plastic strain
- Fading memory of the initial anisotropy

2.3.2. Overconsolidation Boundary Surface

The overconsolidation boundary surface is defined as

$$f_b = \bar{\eta}^*_{(0)} + M^*_m \ln\left(\sigma'_m / \sigma'_{mb}\right) = 0 \tag{2-41}$$

$$\bar{\eta}^*_{(0)} = \left\{\left(\eta^*_{ij} - \eta^*_{ij(0)}\right)\left(\eta^*_{ij} - \eta^*_{ij(0)}\right)\right\}^{\frac{1}{2}} \tag{2-42}$$

where η^*_{ij} is the stress ratio defined as $\eta^*_{ij} = S_{ij} / \sigma'_m$, $\eta^*_{ij(0)}$ is the value for η^*_{ij} at the end of consolidation, σ'_m is the mean effective stress, S_{ij} is the deviatoric stress tensor, and M^*_m is the value of the stress ratio expressed by $\sqrt{\eta^*_{ij}\eta^*_{ij}}$ when the maximum volumetric strain during shearing takes place and which could be called the phase transformation stress ratio, and σ'_{mb} is obtained as

$$\frac{d\sigma'_{mb}}{\sigma'_{mb}} = \frac{\lambda - \kappa}{1+e} d\varepsilon_v^p \tag{2-43}$$

$$\sigma'_{mb} = \sigma'_{mbi} \exp(\frac{1+e}{\lambda - \kappa} \varepsilon_v^p) \tag{2-44}$$

in which σ'_{mbi} is the initial value for σ'_{mb} determined based on the volumetric change characteristics of soils by the quasi overconsolidation ratio as

$$OCR^* = \sigma'_{mbi} / \sigma'_{mc} \tag{2-45}$$

σ'_{mc}, which is the mean effective stress at the intersection of the overconsolidation boundary surface and the σ'_m axis, can be obtained as

$$\sigma'_{mc} = \sigma'_{mb} \exp(\frac{\eta^*_{(0)}}{M^*_m}) \tag{2-46}$$

$$\eta^*_{(0)} = \sqrt{\eta^*_{ij(0)} \eta^*_{ij(0)}} \tag{2-47}$$

The yield function for changes in the stress ratio is denoted as

$$f_{y1} = \bar{\eta}^*_\chi - k = 0 \tag{2-48}$$

$$\bar{\eta}^*_\chi = \left\{ \left(\eta^*_{ij} - \chi^*_{ij} \right) \left(\eta^*_{ij} - \chi^*_{ij} \right) \right\}^{\frac{1}{2}} \tag{2-49}$$

in which k is a parameter for controlling the size of the elastic region and χ^*_{ij} is the nonlinear kinematic hardening parameter. The evolution equation for the hardening parameter is defined by

$$d\chi^*_{ij} = B^* \left(A^* de^p_{ij} - \chi^*_{ij} d\gamma^p \right) \tag{2-50}$$

$$d\gamma^p = \sqrt{de^p_{ij} de^p_{ij}} \tag{2-51}$$

in which A^* and B^* are material parameters, de^p_{ij} is the plastic deviatoric strain increment tensor, and $d\gamma^p$ is the plastic shear strain increment tensor. A^* is related to the stress ratio at failure, namely, $A^* = M^*_f$, and B^* is related to the viscoplastic shear strain as

$$B^* = \left(B^*_{\max} - B^*_1\right)\exp\left(-C_f \gamma^{vp*}_{(n)}\right) + B^*_1 \tag{2-52}$$

in which B^*_1 is the lower boundary of B^*, C_f is the parameter controlling the amount of reduction, and $\gamma^{p*}_{(n)}$ is the accumulated plastic shear strain between two sequential stress reversal points in the previous cycle. $B^*_{\max}$ is the maximum value for parameter B^* defined by Oka et al. (1999) as

$$B^*_{\max} = \begin{cases} B^*_0 & \text{:Before Failure} \\ \dfrac{B^*_0}{1 + \gamma^{p*}_{(n)\max} \Big/ \gamma^{p*}_{(n)r}} & \text{:After Failure} \end{cases} \tag{2-53}$$

where B^*_0 is the initial value for B^*, $\gamma^{p*}_{(n)\max}$ is the maximum value for $\gamma^{p*}_{(n)}$ in past cycles, and $\gamma^{p*}_{(n)r}$ is the plastic reference strain.

Oka et al. (2004) suggested another rule for $B^*_{\max}$, namely,

$$B^*_{\max} = \begin{cases} B^*_0 & \text{:Before Failure} \\ \dfrac{B^*_0}{1 + \gamma^{p*}_{apc} \Big/ \gamma^{p*}_{apr}} & \text{:After Failure} \end{cases} \tag{2-54}$$

in which γ^{p*}_{apc} is the accumulated plastic shear strain after failure and γ^{p*}_{apr} is the plastic reference strain. The same type of equation is also applied to the degradation function of the elastic shear modulus, in which $\gamma^{E*}_{(n)r}$ and γ^{E*}_{apr} are used as the reference values instead of $\gamma^{p*}_{(n)r}$ and γ^{p*}_{apr}.

For changes in the mean effective stress, the following yield function is used:

$$f_{y2} = M^*_m \left|\ln\left(\sigma'_m / \sigma'_{mk}\right) - y^*_m\right| - R_d = 0 \tag{2-55}$$

where y^*_m is the scalar kinematic hardening parameter, σ'_{mk} is the unit value for the mean effective stress, and R_d is a scalar variable. The scalar kinematic hardening parameter, y^*_m, can be broken down into two terms, namely,

$$dy^*_m = dy^*_{m1} + dy^*_{m2} \tag{2-56}$$

The evolution equations for the scalar kinematic hardening parameter are assumed to be nonlinear for y_{m1}^{*} and linear for y_{m2}^{*} in this way

$$dy_{m1}^{*} = B_2^{*}\left(A_2^{*} d\varepsilon_v^{p} - y_{m1}^{*}\left|d\varepsilon_v^{p}\right|\right) \tag{2-57}$$

$$dy_{m2}^{*} = H_2^{*} d\varepsilon_v^{p} \tag{2-58}$$

where A_2^{*}, B_2^{*}, and H_2^{*} are the material parameters. For cyclic behavior under undrained conditions, the changes in mean effective stress are insignificant; hence, the second yield function can be disregarded for simplicity.

The second yield function Equation (2-55) was not used in the present analysis because liquefaction is dominated.

2.3.3. Plastic Potential Function

The plastic potential function is defined as

$$g = \bar{\eta}_{\chi}^{*} + \tilde{M}^{*} \ln\left(\sigma'_m / \sigma'_{mp}\right) = 0 \tag{2-59}$$

Dilatancy coefficient $\tilde{M}^{*}$ is defined separately for the normally consolidated (NC) region and the overconsolidated (OC) region. According to the new modification, the dilatancy coefficient is obtained as

$$\tilde{M}^{*} = \begin{cases} M_m^{*} & \text{:NC region} \\ \left(\sigma_m^{*} / \sigma'_{mc}\right) M_m^{*} & \text{:OC region} \end{cases} \tag{2-60}$$

in which σ_m^{*} denotes the mean effective stress at the intersection of the surface, given by

$$\sigma_m^{*} = \sigma'_m \ \exp\left(\frac{\bar{\eta}_{\chi}^{*}}{M_m^{*}}\right) \tag{2-61}$$

The generalized flow rule for the constitutive model, using fourth rank isotropic tensor H_{ijkl}, is expressed as

$$d\varepsilon_{ij}^{p} = H_{ijkl}\frac{\partial g}{\partial \sigma'_{kl}} \tag{2-62}$$

$$H_{ijkl} = a\delta_{ij}\delta_{kl} + b\left(\delta_{ik}\delta_{jl} + \delta_{il}\delta_{jk}\right) \tag{2-63}$$

where $d\varepsilon_{ij}^{p}$ is the plastic strain increment tensor and $d\sigma'_{kl}$ is the effective stress increment tensor. *a* and *b* are material constants.

The stress-dilatancy relation is obtained from the generalized flow rule as

$$\frac{d\varepsilon_{v}^{p}}{d\gamma_{v}^{p}} = D^{*}\left(\tilde{M}^{*} - \bar{\eta}_{\chi}^{*}\right) \tag{2-64}$$

in which $D^{*} = 3a/2b + 1$ is the dilatancy parameter controlling the ratio of the plastic deviatoric increment to the plastic deviatoric strain increment. The variation in D^{*} is given by

$$D^{*} = D_{0}^{*}\left(\tilde{M}^{*}/M_{m}^{*}\right)^{n_0} \tag{2-65}$$

In Equation (2-65), D_{0}^{*} and n_0 are material parameters

During cyclic loading in soils, the effect of the initial anisotropy decreases. The overconsolidation boundary surface depends on the initial anisotropy of the soil. This means that the existence of the initial anisotropy influences the shape of the overconsolidation boundary surface. Therefore, the initial anisotropy is assumed to fade during the cyclic loading. To consider this, coefficient ζ is used in the definition of σ'_{mc} as

$$\sigma'_{mc} = \sigma'_{mb}\,\exp\left(\zeta\frac{\bar{\eta}_{(0)}^{*}}{M_{m}^{*}}\right) \tag{2-66}$$

$$\zeta = \exp\left(-C_{d}\gamma_{cum}^{*}\right) \tag{2-67}$$

where γ_{cum}^{*} is the accumulative plastic shear strain and C_d is a constant that controls the rate of disappearance of anisotropy.

2.3.4. Results of Test Simulations

In this section, the results of cyclic triaxial test simulations performed on Akita sand are presented. Table 2.2 shows the material properties used for this analysis.

Simulations were performed for different cyclic stress ratios (CSR) and the results are shown herein. Figure 2.7 presents the cyclic strength curve of the Akita clay used in this study. Figures 2.8 and 2.9 also show the deviator stress versus mean effective stress along with the deviator stress versus axial strain results for the triaxial test simulations.

Table 2.2. Material Parameters of Akita Sand

	Elasto-plastic Sand
Density $\rho(t/m^3)$	1.8/2.0
Water specific weight γ_w (kn/m3)	9.81
Coefficient of permeability K^w_s (m/s)	2.25×10^{-4}
Initial void ratio e_0	0.8
Compression index λ	0.025
Swelling index κ	0.0003
Initial elastic shear modulus ratio G_0/σ'_{m0}	761
Stress ratio at phase transformation M^*_m	0.909
Stress ratio at failure M^*_f	1.229
Hardening parameters B^*_0, B^*_1, C_f	5000,300,1000
Structural parameters n,β	0.50,50
Dilatancy parameters D^*_0,n	1.0,4.0
Reference value of plastic strain γ_r^{p*}	0.0050
Reference value of plastic strain γ_r^{e*}	0.003

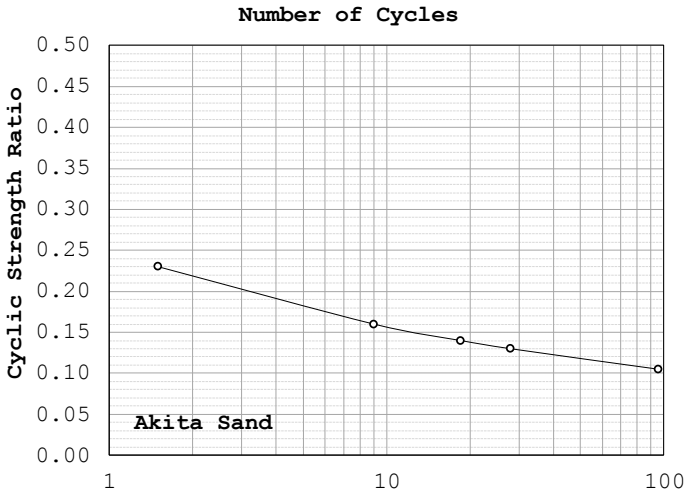

Figure 2.7. Cyclic strength curve of Akita sand

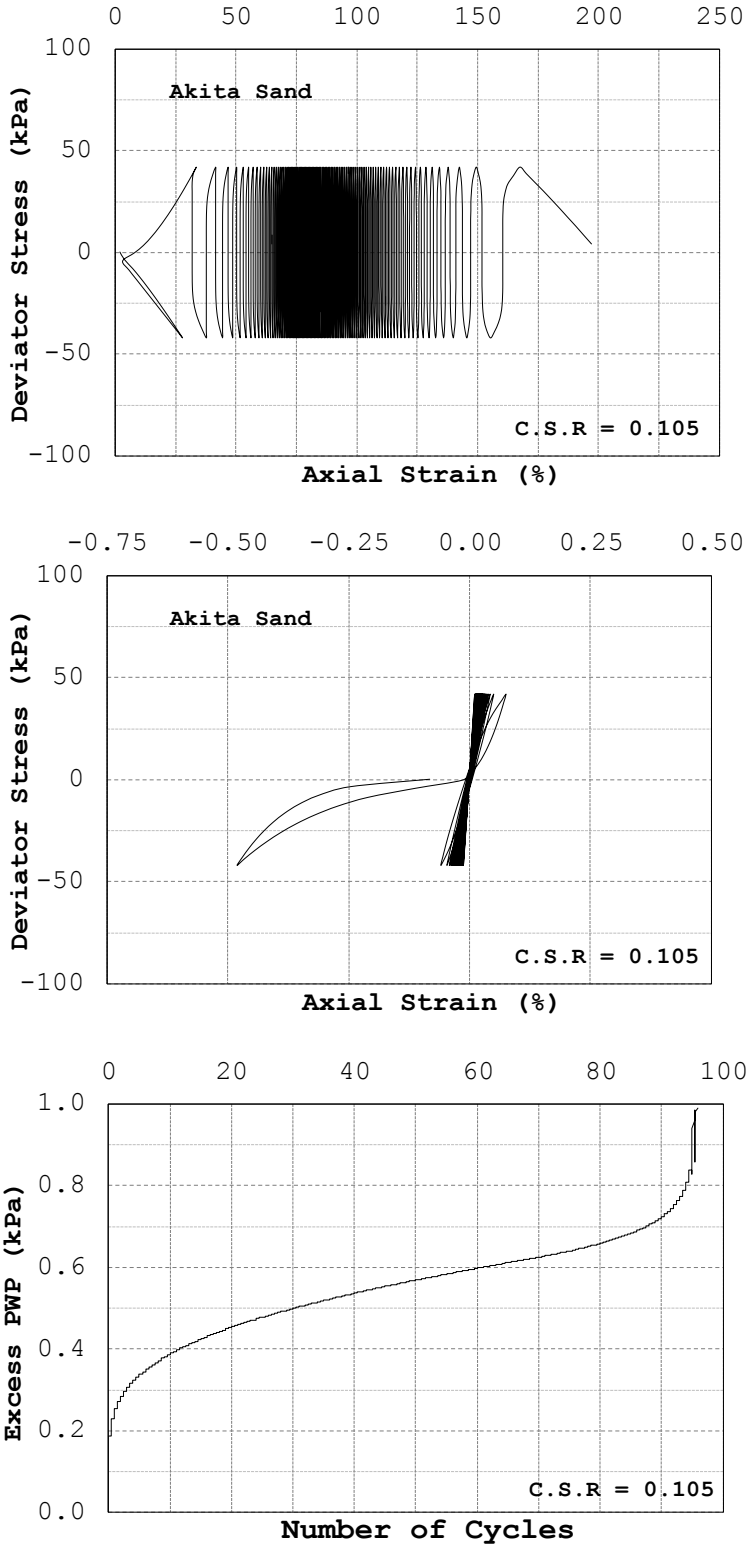

Figure 2.8. Results of cyclic triaxial test simulations on Akita sand for C.S.R = 0.10 and 95.5 cycles

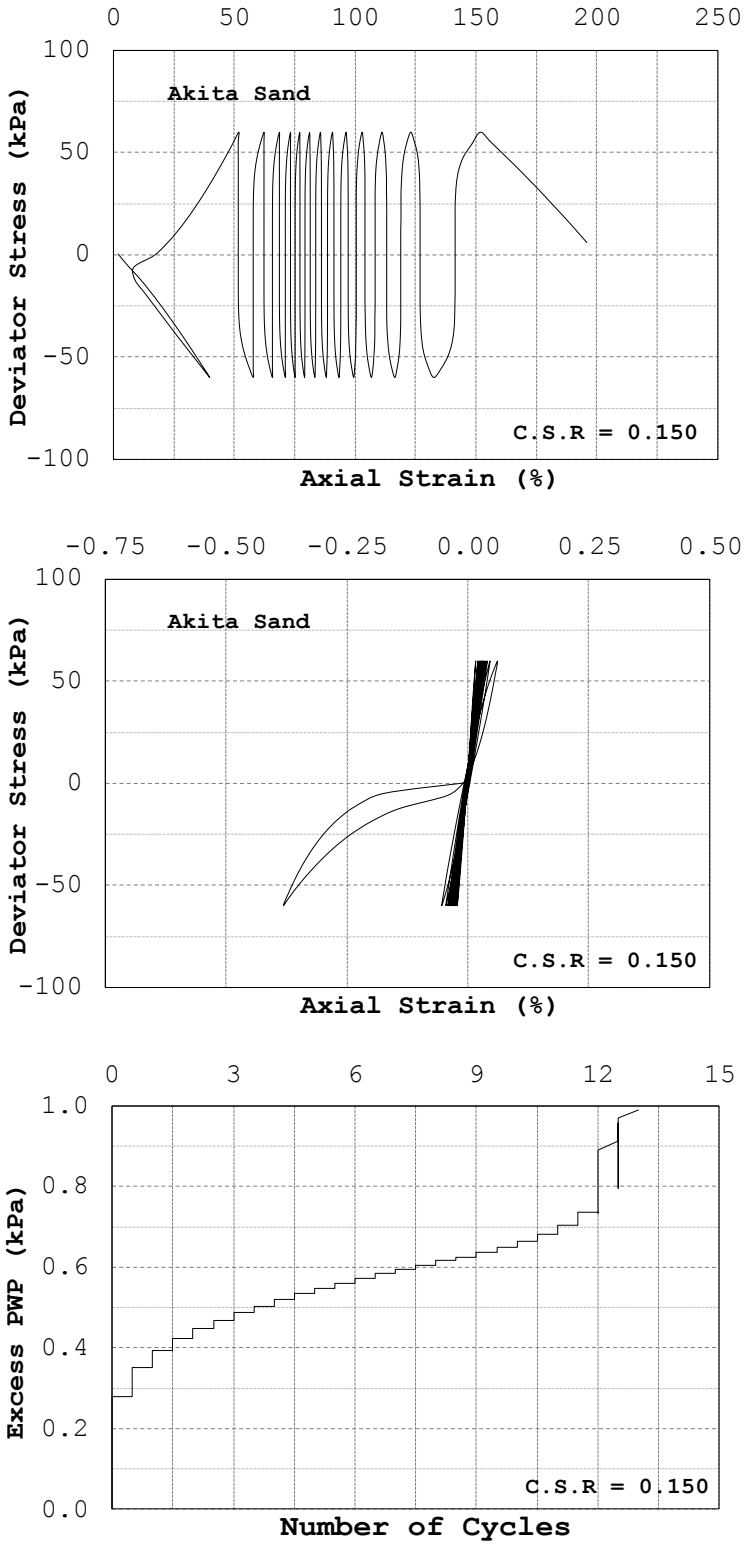

Figure 2.9. Results of cyclic triaxial test simulations on Akita sand for C.S.R = 0.15 and 12.5 cycles

2.4. Summary

In this chapter, two constitutive models for the simulation of clay and sand behaviors were presented. Both models are capable of considering unsaturated soil behavior and the structural degradation of soils. However, due to the lack of unsaturated parameters and experimental data, the simulations have been done on fully saturated soils.

The performances of the two models were examined by a simulation of cyclic triaxial tests, and the results were presented for different cyclic stress ratios. The model parameters for sand belonged to a medium dense sand or sand with a relatively large fines content. The sandy soil was slightly stronger than typical liquefiable loose sand. In addition, the parameters for clay were determined considering the difference between the viscoplastic parameters, based on the values measured in the laboratory at Torishima, Osaka and those measured in the field.

Chapter 3

FEM Formulation of Large Deformation Dynamic Analysis for Multiphase Soils

3.1. Introduction

In this research, a finite deformation FEM analysis for multiphase materials has been adopted to analyze river embankments during earthquakes. The finite deformation theory and the updated Lagrangian approach have been employed, along with the Jaumann rate of Cauchy stress for the weak form of the equilibrium equation (Oka et al., 2002; Kimoto et al., 2004). The theory of multiphase materials is an extension of Biot's two-phase mixture theory for saturated soils (Biot, 1941, 1962). The van Genutchen model was used as the constitutive equation between the water content and suction (van Genutchen, 1980).

Figure 3.1.Isotropic elements for soil skeleton and pore pressure.

Quadrilateral isoparametric eight-node elements with reduced Gaussian integration and four-node quadrilateral isoparametric elements have been used in the FEM finite deformation analysis for displacements and pore pressure, respectively. Figure 3.1 shows the elements and the Gaussian points for the pore pressure and the soil skeleton. The finite element formulation of the porous media analysis, based on the updated Lagrangian method, the discretization of the equilibrium equation, and the continuity equation are hereby explained.

3.2. Volume Fraction and Mass Density

The porous material consists of three continuous phases of solid (S), liquid (L), and gas (G).

$$V = \sum_{\alpha} V^{\alpha} \qquad (\alpha = S, W, G) \tag{3-1}$$

Hence, the volume fraction is defined as the ratio of the volume element to the total volume.

$$n^{\alpha} = \frac{V^{\alpha}}{V} \qquad (\alpha = S, W, G) \tag{3-2}$$

Soil porosity is

$$n = \sum_{\beta} n^{\beta} = \frac{V^{v}}{V} = \frac{V - V^{s}}{V} = 1 - n^{s} \qquad (\beta = W, G) \tag{3-3}$$

The degree of saturation is

$$s = \frac{V^{w}}{V^{w} + V^{G}} = \frac{V^{w}}{V^{v}} \tag{3-4}$$

And, in the end, the volume fraction can be defined as

$$n^{w} = sn \qquad n^{G} = (1 - s)n \tag{3-5}$$

Partial mass density ρ^{i} and realistic mass density ρ_{i} are

$$\rho^{\alpha} = \frac{M^{\alpha}}{V} \qquad and \qquad \rho_{\alpha} = \frac{M^{\alpha}}{V^{\alpha}} \tag{3-6}$$

The density of the mixture is

$$\rho = \sum_{\alpha} \rho^{\alpha} = \sum_{\alpha} \rho_{\alpha} n^{\alpha} \tag{3-7}$$

3.3. Hydraulic Properties of Unsaturated Soils

3.3.1 Soil-Water Characteristic Curve

The soil-water characteristic curve expresses the relationship between the amount of water in the soil and suction. It not only plays a major role in understanding the behavior of partially saturated soils, but it is also recognized as one part of the water phase constitutive relationship in geotechnical engineering. The soil-water characteristic curve (SWCC) can be assumed as a measure of the water-holding capacity (storage capacity) of soil at different levels of suction. In the current model, the van Genutchen (1980) equation has been used for the SWCC.

$$s_{re} = \left[1 + \left(\alpha P^{c}\right)^{n'}\right]^{-m} \tag{3-8}$$

in which α, m, and n' are the material parameters with the relation

$$m = 1 - 1/n' \tag{3-9}$$

and s_{re} is the effective degree of saturation as

$$s_{re} = \left(\frac{s - s_{min}}{s_{max} - s_{min}}\right) \tag{3-10}$$

in which s_{min} and s_{max} are the minimum and the maximum degrees of saturation, respectively.

3.3.2 Unsaturated Permeability of Soils

In the present study, k^{W} and k^{G} represent the coefficients of permeability for the water and the gas phases, respectively. Here, the permeability is a function of the void ratio and the degree of saturation. They can be functions of any two of three possible volume-mass properties, namely, degree of saturation, void ratio, and water content (Lambe and Whitman, 1969; Lloret and Alonso, 1980).

The van Genutchen type of permeability describes the effect of the degree of saturation of soils on the permeability as

$$k^W = k_s^W s_{re}^a \left\{1 - \left(1 - s_{re}^{1/m}\right)^m\right\}^2, \qquad k^G = k_s^G \left(1 - s_{re}\right)^b \left\{\left(1 - s_{re}^{1/m}\right)\right\}^{2m} \tag{3-11}$$

Nevertheless, these equations show some numerical instabilities when the saturation approaches 1. To overcome this problem, Garcia et al. (2010) implemented a modified form of the equations, namely,

$$k^W = k_s^W s_{re}^a \left\{1 - \left(1 - s_{re}^{1/m}\right)^{n'}\right\}^2, \qquad k^G = k_s^G \left(1 - s_{re}\right)^b \left\{\left(1 - s_{re}^{1/m}\right)^{n'}\right\} \tag{3-12}$$

where a and b are material parameters, and m & n' are parameters of the van Genutchen equation. k_s^W and k_s^G are related to void ratio e in this form

$$k_s^W = k_{s0}^W \exp\left[\left(e - e_0\right)/C_k\right], \qquad k_s^G = k_{s0}^G \exp\left[\left(e - e_0\right)/C_k\right] \tag{3-13}$$

in which k_{s0}^W and k_{s0}^G correspond to the values for k_s^W and k_s^G at $e = e_0$. C_k is a material constant reflecting the changes in permeability due to the changes in void ratio.

3.4. Conservation of Mass

With the balance of mass for each phase, using the Eulerian framework and ignoring the mass exchange among phases, we have

$$\frac{d^\alpha}{dt}\int_V \rho_\alpha n^\alpha dV = 0 \quad \left(\alpha, \beta = S, W, G\right) \tag{3-14}$$

in which V, ρ_α, and n^a are the volume, the mass density, and the volume fraction of each phase, respectively, and $\frac{d^\alpha}{dt}$ is the material time derivative with respect to phase α. Thus, Equation (3-14) yields

$$\int_V \left(\frac{d^\alpha}{dt}\left(\rho_\alpha n^\alpha\right) + \rho_\alpha n^\alpha \frac{\partial v_i^a}{\partial x_i} \right) dV = 0 \tag{3-15}$$

By transforming the current volume into reference volume $dV = JdV_0$, Equation (3-15) leads to

$$\int_{V0} \frac{d^\alpha}{dt} \rho_\alpha n^\alpha J dV_0 = 0 \ , \quad (\alpha, \beta = S, W, G) \tag{3-16}$$

where V_0 is the volume in the reference state and J is the Jacobian of the deformation, as described below.

$$\varepsilon_{pqr} \ J = \varepsilon_{ijk} \ \frac{\partial x_i}{\partial X_p} \ \frac{\partial x_j}{\partial X_q} \frac{\partial x_k}{\partial X_r} \tag{3-17}$$

The material derivative of Equation (3-17) gives

$$\frac{d^\alpha}{dt}\left(\frac{\partial x_i}{\partial X_j}\right) = \frac{\partial}{\partial X_j} \ \frac{d^\alpha x_i}{dt} \ = \ \frac{\partial v_i^\alpha}{\partial X_j} \tag{3-18}$$

and the material derivative of the Jacobian becomes

$$\frac{d^\alpha}{dt}\left(J\right) = v_{i,i}^\alpha J \tag{3-19}$$

Substituting Equation (3-19) into Equation (3-16), we obtain

$$\int_{V0} \left(\frac{d^\alpha \rho_\alpha n^\alpha}{dt} J + \rho_\alpha n^\alpha \dot{J}\right) dV_0 = \int_{V0} \left(\frac{d^\alpha \rho_\alpha n^\alpha}{dt} + \rho_\alpha n^\alpha v_{i,i}^\alpha\right) J dV_0 \ = 0 \tag{3-20}$$

From Equation (3-20) with an arbitrary V, namely, the local form of Equation (3-15), we have

$$\frac{d^\alpha}{dt}\left(\rho_\alpha n^\alpha\right) + \rho_\alpha n^\alpha v_{i,i}^\alpha = 0 \tag{3-21}$$

Assuming the coexistence of all the three phases at the same arbitrary points and using Equations (3-3), (3-5), and (3-21) we have

$$S \ : \ -\dot{n}\rho_S + (1-n)\rho_S v_{i,i}^S = 0 \tag{3-22}$$

$$W \ : \ \dot{n}s\rho_W + n\dot{s}\rho_W + ns\rho_W v^W_{i,i} = 0 \tag{3-23}$$

$$G \ : \ (1-s)\dot{n}\rho_G - n\dot{s}\rho_G + n(1-s)\dot{\rho}_G + n(1-s)\rho_G v^G_{i,i} = 0 \tag{3-24}$$

The superimposed dots in these equations denote the material time derivative. Dividing both sides of Equations (3-22) and (3-23) by $\frac{\rho_S}{s}$ and ρ_W, respectively, and summing them up yields

$$n\dot{s} + sv^S_{i,i} + ns(v^W_i - v^S_i)_{,i} = 0 \tag{3-25}$$

The relative velocity vectors for water and gas, with respect to the solid phase, are

$$\dot{w}^\beta_i = n^\beta(v^\beta_i - v^S_i) \qquad \beta = W,G \tag{3-26}$$

By substituting $\dot{w}^W_i$ into Equation (3-25), we will have the mass conservation equation for the water phase as

$$sD_{ii} + \dot{s}n = -\dot{w}^W_{i,i} \tag{3-27}$$

in which D_{ii} is the stretching tensor, namely,

$$D_{ij} = \frac{1}{2}(L_{ij} + L_{ji}) \qquad L_{ij} = v^S_{i,j} \tag{3-28}$$

With a similar procedure taken for the water phase, namely, dividing both sides of Equations (3-22) and (3-23) by $\frac{\rho_S}{(1-s)}$ and ρ_G, respectively, we obtain

$$-n\dot{s} + n(1-s)\frac{\dot{\rho}_G}{\rho_G} + (1-s)v^S_{i,i} + n(1-s)(v^G_i - v^S_i)_{,i} = 0 \tag{3-29}$$

And, the final equation of mass conservation for the gas phase yields

$$(1-s)D_{ii} - n\dot{s} + (1-s)n\frac{\dot{\rho}_G}{\rho_G} = -\dot{w}^G_{i,i} \tag{3-30}$$

3.5. Conservation of Linear Momentum

In simple terms, the Conservation of Linear Momentum is a principle for which the total linear momentum of an isolated system remains constant regardless of changes within the system. In other words, for any part of a body, the change in linear momentum is equal to the sum of the forces acting on that part. In the Eulerian framework, it is expressed as

$$\int_{\Gamma} T_{ji}^{\alpha} n_j d\Gamma + \int_V \rho_\alpha n^\alpha b_i dV + \int_V \sum_\gamma h_i^{\alpha\gamma}\, dV = \frac{d^\alpha}{dt}\int_V \rho_\alpha n^\alpha v_i^\alpha\, dV \quad (\alpha,\gamma = S,W,G) \tag{3-31}$$

In Equation (3-23), Γ and V are the area of the current state and its volume, respectively. T^α is the partial Cauchy stress, n_j is the unit normal vector to Γ, b is the body force per unit mass, and $h^{\alpha\gamma}$ is the density of the internal force imposed by phase α on phase γ ($h^{\alpha\gamma} = -h^{\gamma\alpha}$) for every phase.

The right-hand side of this equation can be restated as

$$\frac{d^\alpha}{dt}\int_V \rho_\alpha n^\alpha v^\alpha dV = \int_V \rho_\alpha n^\alpha a_i^\alpha dV \tag{3-32}$$

Acceleration vector a^α is

$$a^\alpha = \frac{d^\alpha v^\alpha}{dt} = \frac{\partial v_i^\alpha}{\partial t} + v^\alpha \frac{\partial v^\alpha}{\partial x_i} \tag{3-33}$$

Using Gauss and Cauchy's stress theorems, and considering Equation (3-32), Equation (3-31) becomes

$$\int_V T_{ji,j}^{\alpha} dV + \int_V \rho_\alpha b_i n^\alpha dV + \int_V \sum_\gamma h^{\alpha\gamma} dV = \int_V \rho_\alpha n^\alpha a_i^\alpha dV \tag{3-34}$$

Given that V is arbitrary, Equation (3-34) becomes

$$T_{ji,j}^{\alpha} + \rho_\alpha n^\alpha b_i + \sum_\gamma h_i^{\alpha\gamma} = \rho_\alpha n^\alpha a_i^\alpha \quad (\alpha,\gamma = S,W,G) \tag{3-35}$$

Using the above equations, the momentum balance equation for each phase is

$$S\ :\ T^{S}_{ji,j}+\rho_S n^S b_i+h^{SW}_i+h^{SG}_i=\rho_S n^S a^S_i \tag{3-36}$$

$$W\ :\ T^{W}_{ji,j}+\rho_W n^W b_i+h^{WS}_i+h^{WG}_i=\rho_W n^W a^W_i \tag{3-37}$$

$$G\ :\ T^{G}_{ji,j}+\rho_G n^G b_i+h^{GS}_i+h^{GW}_i=\rho_G n^G a^G_i \tag{3-38}$$

Assuming that the interaction between liquid and gas phases is negligible gives

$$h^{WG}_i\simeq 0,\ \ h^{GW}_i\simeq 0 \tag{3-39}$$

Other interaction terms, h^{SW}_i and h^{SG}_i can be given as follows:

$$h^{SW}_i=\frac{n^W\gamma W}{k^W}\dot{w}^W_i \tag{3-40}$$

$$h^{SG}_i=\frac{n^G\gamma G}{k^G}\dot{w}^G_i \tag{3-41}$$

where $\dot{w}^W_i$ and $\dot{w}^G_i$ are the average velocity vectors of water and gas with respect to the solid skeleton, respectively. Using Equations (3-26), (3-37) & (3-38), we obtain

$$\rho_\beta n^\beta\left(a^S_i+\frac{1}{n^\beta}\ddot{w}^\beta_i\right)+h^{S\beta}_i=T^{\beta}_{ji,j}+\rho_\beta n^\beta b_i\quad\left(\beta=W,G\right) \tag{3-42}$$

in which $\ddot{w}^B_i$ is the acceleration vector of fluid phase with respect to solid skeleton.

Adopting a $u-p$ formulation, the relative acceleration of the fluid phases is negligible in comparison with that of the solid phase, and thus, Equation (3-42) yields

$$\rho_\beta n^\beta a^S_i+\frac{n^\beta\gamma_\beta}{k_\beta}\dot{w}^\beta_i=-n^\beta P^\beta_{,i}+\rho_\beta n^\beta b_i$$

or,

$$\dot{w}^\beta_i=\frac{k_\beta}{\gamma_\beta}\left(-P^\beta_{,i}-\rho_\beta a^S_i+\rho_\beta b_i\right) \tag{3-43}$$

3.6. Equation of Motion for the Whole Mixture

The derivation of the equation of motion for the whole mixture can be started by the summation of Equations (3-36) ~ (3-38) as

$$T_{ji,j} + \rho b_i = \rho_S n^S a_i^S + \rho_W n^W a_i^W + \rho_G n^G a_i^G \tag{3-44}$$

where T_{ji} is the total Cauchy stress tensor obtained from the accumulation of the partial stresses T_{ji}^{α}.

$$T_{ji} = \sum_{\alpha} T_{ji}^{\alpha} \qquad (\alpha = S, W, G), \text{ and } \rho = \rho_S n^S + \rho_W n^W + \rho_G n^G \tag{3-45}$$

Equation (3-44) can be rewritten as

$$T_{ji,j} + \rho b_i = \rho_S a_i^S + \rho_W n^W \left(a_i^S + \frac{\ddot{w}^W}{n^W} \right) + \rho_G n^G \left(a_i^S + \frac{\ddot{w}^G}{n^G} \right) \tag{3-46}$$

where $\ddot{w}_i^W$ and $\ddot{w}_i^G$ are the average acceleration vectors of water and gas with respect to the solid skeleton, respectively.

By disregarding the relative accelerations between the solid phase and other phases, the equation of motion for the whole mixture is

$$T_{ji,j} + \rho b_i = \rho_S a_i^S \tag{3-47}$$

3.7. Continuity Equations for Fluids

Continuity equations for the fluid phases can be obtained from the conservation of momentum and the mass equations. Substituting Equation (3-43) into Equation (3-27) gives

$$\dot{w}_i^{\beta} = \frac{k^W}{\gamma_W} \left(-P_{,ii}^W - \rho_W a_{i,i}^S + \rho_W b_{i,i} \right) + s D_{ii} + \dot{s} n = 0 \tag{3-48}$$

By using the relation $a_{i,i}^S = \dot{D}_{ii}$ and assuming that the body force is homogeneously distributed in the medium ($b_{i,i} = 0$), Equation (3-48) yields the continuity equation for the liquid phase as

$$\rho_W D_{ii} + P^W_{,ii} - \frac{\gamma_W}{k^W}(sD_{ii} + \dot{s}n) = 0 \tag{3-49}$$

For the gas phase, the substitution of Equation (3-43) into Equation (3-30) gives

$$\rho_G \dot{D}_{ii} + P^G_{,ii} - \frac{\gamma_G}{k^G}\left\{(1-s)D_{ii} - \dot{s}n + (1-s)n\frac{\dot{\rho}_G}{\rho_G}\right\} = 0 \tag{3-50}$$

The equations for the ideal gases are

$$\rho_G = \frac{MP^G}{R\theta} \qquad \& \qquad \dot{\rho}_G = \frac{M}{R}\left(\frac{\dot{P}^G}{\theta} - \frac{P^G\dot{\theta}}{\theta^2}\right) \tag{3-51}$$

where M is the molecular weight of gas, R is the gas constant, and θ is the temperature.

Manipulating Equation (3-51) gives

$$\frac{\dot{\rho}_G}{\rho_G} = \frac{\dot{P}^G}{P^G} - \frac{\dot{\theta}}{\theta} \tag{3-52}$$

Assuming that the temperature remains constant leads to

$$\frac{\dot{\rho}_G}{\rho_G} = \frac{\dot{P}^G}{P^G} \tag{3-53}$$

Finally, the continuity equation for the gas phase is

$$\rho_G \dot{D}_{ii} + P^G_{,ii} - \frac{\gamma_G}{k^G}\left\{(1-s)D_{ii} - \dot{s}n + (1-s)n\frac{\dot{P}_G}{\dot{P}_G}\right\} = 0 \tag{3-54}$$

3.8. Equation of Motion in Lagrangian Form

Time-dependent large deformation problems are usually better described in Lagrangian form rather than in the Eulerian framework. Should the equation of motion for the whole mixture be written in Lagrangian scheme, it will yield

$$\int T_{ji,j} dV = \int \rho(a_i - b_i) dV \tag{3-55}$$

The Cauchy stress tensor can be related to the nominal stress tensor in the following way:

$$\int T_{ji} n_j d\Gamma = \int \Pi_{ji} N_j d\Gamma_0 \tag{3-56}$$

Γ_0 and N_j are the area of reference surface and its unit outward normal vector, respectively. Using the Gauss theorem, Equation (3-56) yields

$$\int T_{ji} d\Gamma = \int \Pi_{ji} d\Gamma_0 \tag{3-57}$$

The nominal stress or ρ_0 is

$$\rho_0(X) = \frac{M\ (current\ state)}{V\ (reference\ state)} \qquad \text{and} \qquad \rho_0 dV_0 = \rho dV \tag{3-58}$$

Using Equations (3-57), (3-58), and (3-55), we obtain

$$\int_{V_0} \Pi_{ji,j} dV_0 = \int_{V_0} \rho_0(a_i - b_i) dV_0 \tag{3-59}$$

which for an arbitrary volume becomes

$$\Pi_{ji,j} = \rho_0(a_i - b_i) \tag{3-60}$$

It should be noted that in this equation, a_i and b_i refer to the current state rather than the reference state.

3.9. Tangent Stiffness Method

The tangent stiffness method is one of the simple solutions to nonlinearity problems in engineering. In the present approach, the incremental stiffness matrix is assumed to be constant over each increment; it is calculated using the current stress state.

In this section, the tangent stiffness method is used with the Jaumann rate of Cauchy stress. Pierce et al. (1984) reported that for a parameter θ between 0.5 and 1.0, the analysis of viscous and rate-dependent materials is stable and accurate.

The viscoplastic stretching tensor is given as

$$D_{ij}^{vp} = C_{ijkl} \left\langle \Phi(f_y) \right\rangle \frac{\partial f_p}{\partial T'_{kl}} \tag{3-61}$$

in which $\Phi(f_y)$ is a function of T'_{ij} and kinematic hardening parameters y^*_{m1} and χ^*_{m1}. Hence, the time derivative of the so-called material function is

$$\dot{\Phi}(f_y) = \frac{\partial \Phi}{\partial T'_{ij}} \dot{T}'_{ij} + \frac{\partial \Phi}{\partial y^*_{m1}} \dot{y}^*_{m1} + \frac{\partial \Phi}{\partial \chi^*_{ij}} \dot{\chi}^*_{ij} \tag{3-62}$$

The relationship between Cauchy's stress and the Jaunmann rate of Cauchy stress is given as

$$\hat{T}'_{ij} = \dot{T}'_{ij} + T'_{ik} W_{kj} - W_{ik} T'_{kj} \tag{3-63}$$

in which W_{ij} is the spin tensor. Using scalar parameters A and B and symmetric tensor U_{ij}, we have

$$\frac{\partial \Phi}{\partial T'_{ij}} \dot{T}' = \frac{\partial \Phi}{\partial T'_{ij}} (\dot{T}'_{ij} + T'_{ik} W_{kj} - W_{ik} T'_{kj}) \tag{3-64}$$

$$= \frac{\partial \Phi}{\partial T'_{ij}} \dot{T}'_{ij} + \frac{\partial \Phi}{\partial T'_{ij}} (T'_{ik} W_{kj} - W_{ik} T'_{kj}) \tag{3-65}$$

$$= \frac{\partial \Phi}{\partial T'_{ij}} \dot{T}'_{ij} + (AU_{ij} + B\delta_{ij})(T'_{ik}W_{kj} - W_{ik}T'_{kj}) \tag{3-66}$$

By $(T'_{ik}W_{kj} - W_{ik}T'_{kj}) = 0$, we have

$$\frac{\partial \Phi}{\partial T'_{ij}} \hat{T}'_{ij} = \frac{\partial \Phi}{\partial T'_{ij}} \dot{T}'_{ij} \tag{3-67}$$

The substitution of Equation (3-67) into Equation (3-62) yields

$$\dot{\Phi}(f_y) = \frac{\partial \Phi}{\partial T'_{ij}} \hat{T}'_{ij} + \frac{\partial \Phi}{\partial y^*_{m1}} \dot{y}^*_{m1} + \frac{\partial \Phi}{\partial \chi^*_{ij}} \dot{\chi}^*_{ij} \tag{3-68}$$

By $\Phi_{t+\nabla t} = \Phi_t + \Delta\Phi = \Phi_t + \Delta t\dot{\Phi}_t$ for the tangent stiffness parameter, we obtain

$$\Phi = (1-\theta)\Phi_t + \theta\Phi_{t+\nabla t} \tag{3-69}$$

Summarizing Equations (3-68) and (3-69), we obtain

$$\Phi = (1-\theta)\Phi_t + \theta\left\{\Phi_t + \frac{\partial \Phi}{\partial T'_{ij}} \hat{T}'_{ij}\,\Delta t + \frac{\partial \Phi}{\partial y^*_{m1}} \dot{y}^*_{m1}\Delta t + \frac{\partial \Phi}{\partial \chi^*_{ij}} \dot{\chi}^*_{ij}\Delta t\right\} \tag{3-70}$$

Using the Jaunmann rate of Cauchy stress tensor, the constitutive equation is rewritten as

$$\hat{T}'_{ij} = C^e_{ijkl}(D_{kl} - D^{vp}_{kl}) \tag{3-71}$$

$$= C^e_{ijkl}(D_{kl} - C_{klmn}\Phi\frac{\partial f_p}{\partial T'_{mn}}) \tag{3-72}$$

The kinematic hardening parameters are

$$\dot{y}^*_{m1} = B^*_2(A^*_2 D^{vp}_{kk} - y^*_{m1}\left|D^{vp}_{kk}\right|) \tag{3-73}$$

$$\chi_{ij}^{*} = B^{*}\left\{A^{*}D_{kk}'^{vp} - \chi_{ij}^{*}(D_{mn}'^{vp}.D_{mn}'^{vp})^{1/2}\right\} \tag{3-74}$$

in which D_{kk}^{vp} and $D_{kk}'^{vp}$ are the viscoplastic volumetric and deviatoric stretching tensors, respectively. Assuming C_{ijkl}^{e} is an isotropic fourth order tensor, we have

$$D_{kk}^{vp} = C_{kkij}\Phi\frac{\partial f_p}{\partial T_{ij}'} \tag{3-75}$$

$$D_{kk}'^{vp} = \left(D_{ij}^{vp} - \frac{1}{3}D_{kk}^{vp}\delta_{ij}\right) = C_{ijkl}\Phi\frac{\partial f_p}{\partial S_{kl}} \tag{3-76}$$

Substituting the above equations into Equation (3-70) gives

$$\Phi = (1-\theta)\Phi_t + \theta\left\{\begin{array}{l}\Phi_t + \dfrac{\partial\Phi}{\partial T_{ij}'}\widehat{T}_{ij}'\ C_{ijkl}^{e}(D_{kl} - D_{kl}^{vp})\Delta t + \dfrac{\partial\Phi}{\partial y_{m1}^{*}}\dot{y}_{m1}^{*}B_2^{*}(A_2^{*}D_{kk}^{vp} - y_{m1}^{*}\left|D_{kk}^{vp}\right|)\Delta t \\ \qquad\qquad + \dfrac{\partial\Phi}{\partial\chi_{ij}^{*}}B^{*}\left\{A^{*}D_{ij}'^{vp} - \chi_{ij}^{*}(D_{mn}'^{vp}D_{mn}'^{vp})^{1/2}\right\}\Delta t\end{array}\right\} \tag{3-77}$$

$$\begin{aligned}\rightarrow \Phi &= \Phi_t + \theta C_{ijkl}^{e}D_{kl}\Delta t \\ &\quad - \theta\ \Delta\nabla t\Phi\frac{\partial\Phi}{\partial T_{ij}'}C_{ijkl}^{e}C_{klmn}\frac{\partial f_p}{\partial T_{mn}'} \\ &\quad + \theta\ \Delta t\Phi\frac{\partial\Phi}{\partial y_{m1}^{*}}B_2^{*}\left(A_2^{*}C_{kkij}\frac{\partial f_p}{\partial T_{ij}'} - y_{m1}^{*}\left|C_{kkij}\frac{\partial f_p}{\partial T_{ij}'}\right|\right) \\ &\quad + \theta\ \Delta t\Phi\frac{\partial\Phi}{\partial\chi_{ij}^{*}}B^{*}\left\{A^{*}C_{ijkl}\frac{\partial f_p}{\partial S_{kl}} - \chi_{ij}^{*}\left(C_{mnpq}\frac{\partial f_p}{\partial S_{pq}}C_{mnrs}\frac{\partial f_p}{\partial S_{rs}}\right)^{1/2}\right\}\end{aligned} \tag{3-78}$$

By assuming

$$\xi' = \left(\theta\ \nabla t\right)\left\{\begin{array}{l} \dfrac{\partial \Phi}{\partial T'_{ij}} C^e_{ijkl} C_{klmn} \dfrac{\partial f_p}{\partial T'_{ij}} - \dfrac{\partial \Phi}{\partial y^*_{m1}} B^*_2 \left(A^*_2 C_{kkij} \dfrac{\partial f_p}{\partial T'_{ij}} - y^*_{m1} \left| C_{kkij} \dfrac{\partial f_p}{\partial T'_{ij}} \right| \right) \\ -\dfrac{\partial \Phi}{\partial \chi^*_{ij}} B^* \left(A^* C_{ijkl} \dfrac{\partial f_p}{\partial S_{kl}} - \chi^*_{ij} \left(C_{mnpq} \dfrac{\partial f_p}{\partial S_{pq}} C_{mnrs} \dfrac{\partial f_p}{\partial S_{rs}} \right) \right)^{1/2} \end{array}\right\} \tag{3-79}$$

we have

$$\Phi = \frac{1}{1+\xi'}\left\{ \Phi_t + \left(\theta\ \Delta t\right) \frac{\partial \Phi}{\partial T'_{ij}} C^e_{ijkl} D_{kl} \right\} \tag{3-80}$$

The substitution of Equation (3-80) into Equation (3-61) gives

$$D^{vp}_{ij} = C_{ijkl} \frac{1}{1+\xi'}\left\{ \Phi_t + \left(\theta\ \Delta t\right) \frac{\partial \Phi}{\partial T'_{pq}} C^e_{pqrs} D_{rs} \right\} \frac{\partial f_p}{\partial T'_{kl}} \tag{3-81}$$

The substitution of Equation (3-81) into Equation (3-71) yields

$$\begin{aligned} \hat{T}'_{ij} &= C^e_{ijkl}\left(D_{kl} - C_{klmn} \frac{1}{1+\xi'}\left\{ \Phi_t + \left(\theta\ \Delta t\right) \frac{\partial \Phi}{\partial T'_{pq}} C^e_{pqrs} D_{rs} \right\} \frac{\partial f_p}{\partial T'_{mn}} \right) \\ &= \left[C^e_{ijkl} - C^e_{ijrs} C_{rsmn} \frac{\partial f_p}{\partial T'_{kl}} \frac{1}{1+\xi'} \left(\theta\ \Delta t\right) \frac{\partial \Phi}{\partial T'_{pq}} C^e_{pqkl} \right] D_{kl} - C^e_{ijkl} C_{klmn} \frac{\partial f_p}{\partial T'_{mn}} \frac{1}{1+\xi'} \Phi_t \end{aligned} \tag{3-82}$$

In the end, tangential stiffness matrix C^{tan}_{ijkl} and relaxation stress Q_{ij} are

$$C^{tan}_{ijkl} = C^e_{ijkl} - C^e_{ijrs} C_{rsmn} \frac{\partial f_p}{\partial T'_{mn}} \frac{1}{1+\xi'} \left(\theta\ \Delta t\right) \frac{\partial \Phi}{\partial T'_{pq}} C^e_{pqkl} \tag{3-83}$$

$$Q_{ij} = C^e_{ijkl} C_{klmn} \frac{\partial f_p}{\partial T'_{mn}} \frac{1}{1+\xi'} \Phi_t \tag{3-84}$$

And finally,

$$\hat{T}'_{ij} = C^{tan}_{ijkl} D_{kl} - Q_{ij} \tag{3-85}$$

3.10. Time Discretization of the Governing Equations

In the present formulation, the Newmark β method has been used for the discretization on the time domain. Using that method, the displacements and velocities of the soil skeleton can be approximated as

$$\{u_N\}_{t+\Delta t} = (\Delta t)\{u_N\}_t + \frac{(\Delta t)^2}{2}\{a_N\}_t + \beta(\Delta t)^2\left(\{a_N\}_{t+\Delta t} - \{a_N\}_t\right) \tag{3-86}$$

$$\{u_N\}_{t+\Delta t} = \{u_N\}_t + (\Delta t)\{a_N\}_t + \gamma(\Delta t)\left(\{a_N\}_{t+\Delta t} - \{a_N\}_t\right) \tag{3-87}$$

in which Δt is the time increment, and β & γ are Newmarks' parameters. Using Equations (3-86) and (3-87) and substituting them into a backward finite difference method gives

$$\begin{aligned}
&\{M\}_{t+\Delta t} + (\Delta t)\{a_N\}_{t+\Delta t} + \gamma(\Delta t)\left\{\left([K]_{t+\Delta t} + [K_L]_{t+\Delta t}\right)(\Delta t) + [R]_{t+\Delta t}\right\}\{a_N\}_{t+\Delta t} \\
&\quad -(-A_s + s)[K_v]_{t+\Delta t}\{P_N^W\}_{t+\Delta t} \\
&\quad -\left(A_s + (1-s)\right)[K_v]_{t+\Delta t}\{P_N^G\}_{t+\Delta t} \\
&\quad = \{F\}_{t+\Delta t} - \{T^*\}_t\{T_W\}_t \\
&\quad -(-A_s + s)[K_v]_{t+\Delta t}\{P_N^W\}_t \\
&\quad -\left(A_s + (1-s)\right)[K_v]_{t+\Delta t}\{P_N^G\}_t \\
&\quad -\left\{\left([K]_{t+\Delta t} + [K_L]_{t+\Delta t}\right)(\Delta t) + [R]_{t+\Delta t}\right\}\left[(\Delta t)(1-\gamma)\{a_N\}_t + \{u_N\}_t\right]
\end{aligned} \tag{3-88}$$

Equation (3-88) is the final discretized equation of motion; it gives the gas and liquid forms by simple substitutions.

3.11. Final Form of Governing Equations

Using Equation (3-88), the matrix form of the final governing equations is

$$[A]\{x\} = \{B\} \tag{3-89}$$

in which

$$[A]=\begin{bmatrix} \{M\}_{t+\Delta t} & & \\ +\gamma(\Delta t)\left\{\left([K]_{t+\Delta t}+[K_L]_{t+\Delta t}\right)(\Delta t)+[R]_{t+\Delta t}\right\} & -(-A_s+s)[K_v]_{t+\Delta t} & -\left(A_s+(1-s)\right)[K_v]_{t+\Delta t} \\ \Delta t\left(\rho_W-\dfrac{\gamma_W(\Delta t)\gamma}{\kappa^W}s\right)[K_v]^T_{t+\Delta t} & -(\Delta t)\ [K_h]_{t+\Delta t}+\left(\dfrac{\gamma_W}{\kappa^W}\right)n\ \dfrac{\partial s}{\partial P^C}[K_n]_{t+\Delta t} & -\left(\dfrac{\gamma_W}{\kappa^W}\right)n\dfrac{\partial s}{\partial P^C}[K_n]_{t+\Delta t} \\ \Delta t\left(\rho_G-\dfrac{\gamma_G(\Delta t)\gamma}{\kappa^G}(1-s)\right)[K_v]^T_{t+\Delta t} & -\left(\dfrac{\gamma_G}{\kappa^G}\right)n\dfrac{\partial s}{\partial P^C}[K_n]_{t+\Delta t} & -(\Delta t)\ [K_h]_{t+\Delta t} \\ & & +\dfrac{\gamma_G}{\kappa^G}n\left(\dfrac{\partial s}{\partial P^C}[K_n]_{t+\Delta t}-(1-s)\left[K_c^P\right]_{t+\Delta t}\right) \end{bmatrix} \tag{3-90}$$

$$\{x\}=\begin{Bmatrix} [a_N]_{t+\Delta t} \\ \left[P_N^W\right]_{t+\Delta t} \\ \left[P_N^G\right]_{t+\Delta t} \end{Bmatrix} \tag{3-91}$$

$$\{B\}=\begin{Bmatrix} \{F\}_{t+\Delta t}-\{T^*\}_t-(\Delta t)\{T_W\}_t-\left(\left([K_T]_{t+\Delta t}+[K_L]_{t+\Delta t}\right)\Delta t+[R]_{t+\Delta t}\right)\left[(\Delta t)(1-\gamma)[a_N]_t+[U_N]_t\right] \\ -(-A_s+s)[K_v]_{t+\Delta t}\left\{P_N^W\right\}_t-\left(A_s+(1-s)\right)[K_v]_{t+\Delta t}\left\{P_N^G\right\}_t \\ -(\Delta t)\{q^W\}_{t+\Delta t}+(\Delta t)\left(\dfrac{\gamma_W}{\kappa^W}\right)s\dfrac{\partial s}{\partial P^C}[K_v]^T_{t+\Delta t}\left(\Delta t(1-\gamma)\{a_N\}_t+\{u_N\}_t\right) \\ \left(\dfrac{\gamma_W}{\kappa^W}\right)n\dfrac{\partial s}{\partial P^C}[K_n]_{t+\Delta t}\left(\left\{P_N^W\right\}_t-\left\{P_N^G\right\}_t\right) \\ -(\Delta t)\{q^G\}_{t+\Delta t}+(\Delta t)\left(\dfrac{\gamma_G}{\kappa^G}\right)(1-s)[K_v]^T_{t+\Delta t}\left(\Delta t(1-\gamma)\{a_N\}_t+\{u_N\}_t\right) \\ \dfrac{\gamma_G}{\kappa^G}n\dfrac{\partial s}{\partial P^C}[K_n]_{t+\Delta t}\left(\left\{P_N^G\right\}_t-\left\{P_N^W\right\}_t\right)-\dfrac{\gamma_G}{\kappa^G}n(1-s)\left[K_c^P\right]_{t+\Delta t}\left\{P_N^G\right\}_t \end{Bmatrix} \tag{3-92}$$

3.12. Program COMVI2D-DY

Studies on the numerical analysis of liquefaction have been continuously in progress since what was seen with the Niigata (1964) and Alaska (1964) earthquakes. The number of programs that have been developed for predicting and analyzing earthquake-induced liquefaction is enormous. Oka et al. (1994) proposed an infinitesimal effective stress liquefaction analysis program, called "LIQCA2D", which was later extended to a large deformation three-dimensional liquefaction analysis program, "LIQCA3D-FD", with an elasto-plastic constitutive model. Using the same ideas, and based on the response to the same needs, besides the demand to consider the unsaturated soil behavior, much effort was devoted to the development of "COMVI3D-DY011" and "COMVI2D-DY013" by Mirjalili (2010) and Shahbodaghkhan (2011); this research was based on the new formulation herein mentioned. The main features of these codes are as follows:

- Elasto-plastic & elasto-viscoplastic models for soil
- Unsaturated 3-phase models
- 2-dimensional and 3-dimensional
- Dynamic/Transient loading
- Finite deformation analysis

In this program, Newmark's β method is used for the discretization of time. Rayleigh's damping is also adopted; it is proportional to the initial stiffness and mass matrix.

It must be mentioned that, although the code is fully capable of performing dynamic coupled analyses of multiphase materials, since the gas phase is highly compressible (Kato, 2011), the pore-air pressure has been assumed to be zero in the analysis of embankments. This has been done for the sake of simplification, to reduce the computation time, and due to the fact that the effect of the pore-air pressure is negligible in drained conditions.

3.13. Summary

The finite element formulation of a finite deformation dynamic analysis method of multiphase materials was presented in the present chapter and details on the volume fractions, the hydraulic properties of unsaturated soils, the conservation of mass & linear momentum, the equation of motion, continuity equations, and the time discretization method were presented. For the constitutive equation between saturation and suction, the van Genuchten type of equation was employed. As for the discretization in the time domain, Newmark's β method was used and Rayleigh's damping was also adopted, which is proportional to the initial stiffness and mass matrix. In addition, Program COMVI2D-DY, which was developed for the two-dimensional finite deformation dynamic analyses of multiphase elasto-plastic and elasto-viscoplastic materials, was presented.

Chapter 4

Effect of Ground Profile and Earthquake Motion on the Dynamic Behavior and Damage Patterns of River Embankments

4.1. Introduction

Many soil infrastructures, such as river dikes, river embankments, roadway foundations, etc., were damaged by the 2011 off the Pacific Coast of Tohoku Earthquake. River dikes and related structures were damaged at many sites in the Tohoku and Kanto regions. As has been studied by several researchers, such as Oka et al. (2012), the two main causes of the river embankment damage in the above earthquake were the ground profiles, including water tables in embankments, and the long duration of the earthquake. In this chapter, we will study these points by numerical simulations based on the dynamic finite deformation theory and the cyclic constitutive models for sand and clay.

The main issues that provoked the need for this analysis are listed below:

- The analysis of cases related to liquefaction requires a formulation capable of accommodating large deformations caused by this phenomenon. The finite deformation theory and the updated Lagrangian analysis method seem to be more appropriate for the analysis of large deformation nonlinear behavior. The infinitesimal method is not reliable enough for post-failure analyses.

- The parameters used in the models by Oka et al. (2012) for clay are assumed to be soft. This is because they were assessed through experiments, while seismic loadings need to assume stiffer materials. The clay model used in this analysis is neither too soft to settle under its own weight load, nor too stiff to cause a divergence from the realistic observations.

- The reason for assuming soft clay foundations beneath the embankments is that the soft clay deposits affect the earthquake-resistant characteristics through consolidation, amplification, and deformability. The embankments of the Eai River, the Naruse River, and the Yoshida River, which were damaged by the 2011 Tohoku Earthquake, were underlain by soft soil deposits with a thickness of about 10 m. The soft soil deposits consist of clay, fines, and silt, e.g., the soft soil deposit of the dike of the Yoshida River at Yamazaki consists of soft clay, including silt and sand (General Report on the 1978 Miyagi-Oki Earthquake, Investigation Committee of the 1978 Miyagiken-Oki Earthquake at Tohoku Branch of JSCE, 1980).

The results show different failure patterns and damage modes caused by the long duration earthquake and the induced liquefaction. Moreover, it was observed that when part of an embankment body is saturated, the damage is magnified and the patterns of failure and deformation are different from the conventional circular failure pattern assumed in practical geotechnics.

4.2. Numerical Model

4.2.1. Embankment-Foundation Model

In the numerical analysis, four typical patterns of embankment-foundation profiles are used considering the damage patterns observed in the 2011 off the Pacific Coast of Tohoku Earthquake. The four patterns of the ground are illustrated in Figure 4.1. These patterns are same as the ones used in Oka et al. (2012). The water table is at the surface of the foundation ground in Types 1, 2, and 4; however, it is 1.5 m above the ground for Type 3. In Type 1, the embankment is made of sandy soil and it is lying on a saturated clay layer. Type 2 corresponds to the case in which the bottom of the embankment has settled into the clayey foundation and is below the water table. Type 3 illustrates the settlement of the embankment into the soft foundation, while the water table is inside the embankment body. This is the typical case of severe damage induced by the 2011 Tohoku Earthquake and reported by Sasaki (1994) and Oka et al. (2012) to be very weak against earthquakes. Finally, Type 4 is an embankment on a saturated sandy layer lying on a clay layer.

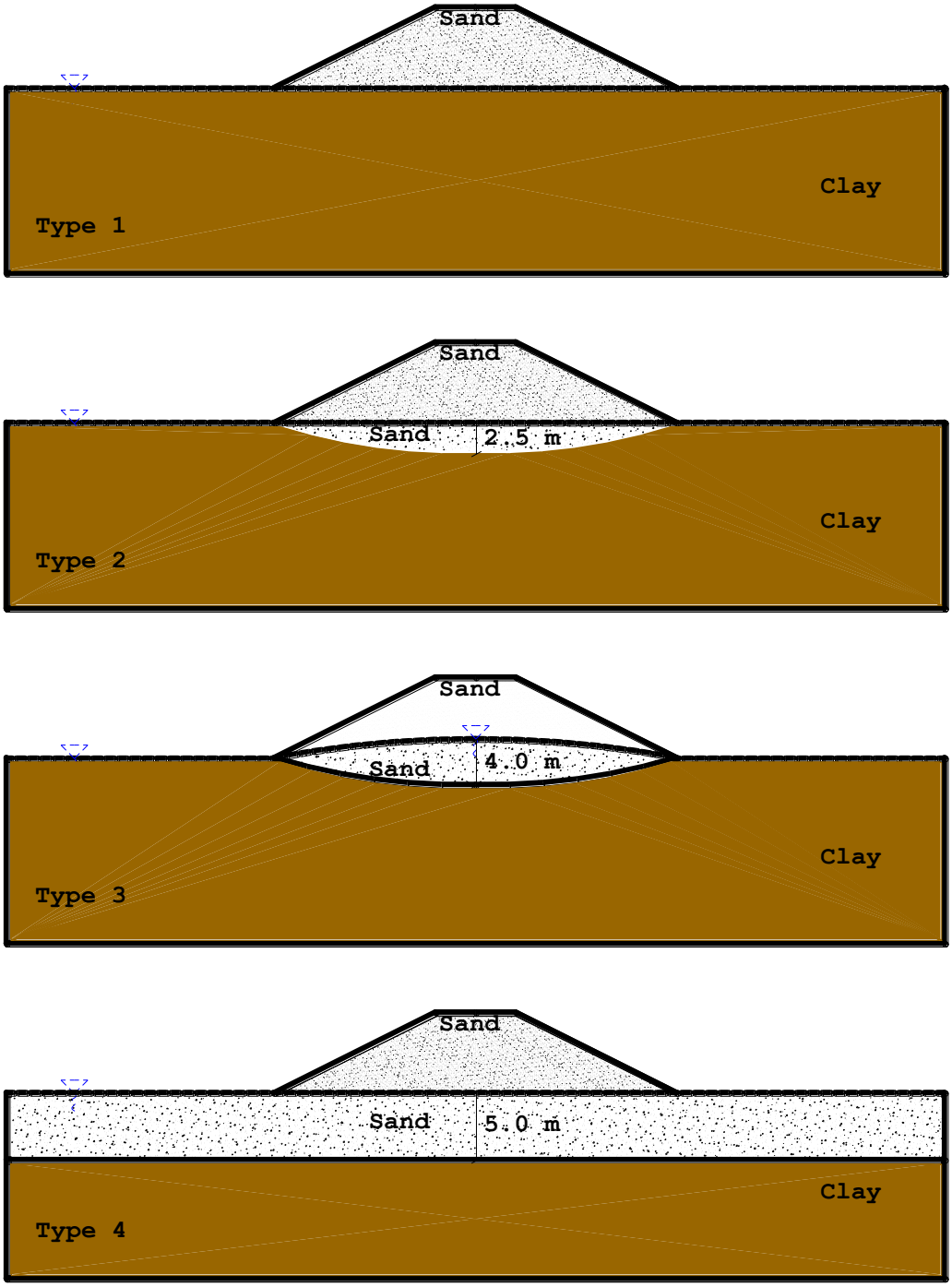

Figure 4.1. Soil profiles and water tables

We adopted soil profiles of clay layers because many levee-foundation systems damaged by the 2011 Tohoku Earthquake in Miyagi Prefecture included clay layers. Moreover, the embankment body outside the saturated zone was assumed to be dry as there was no data for unsaturated soil. However, in the dynamic analysis, it is possible to take the unsaturated soil behavior into account (i.e., Oka et al., 2011).

4.2.2. Input Accelerations

Figure 4.2 shows the input earthquake motion records used in this analysis. Input 1 is the acceleration-time profile obtained during the 1995 Kobe Earthquake and recorded at a depth of 33 m at the Higashi-Kobe Bridge with a maximum acceleration of 446 gal. Input 2 is the earthquake record of MYGH06 at a depth of 80 m at Tajiri by KiK-net, 2011, which had a maximum acceleration of 155 gal and duration of 250 sec.

Input 1 – 1995 Hyogoken Nanbu Earthquake at Higashi Kobe Ohashi (Bridge) Transverse Component (MLIT, 2011)

Max: 445.9 gal

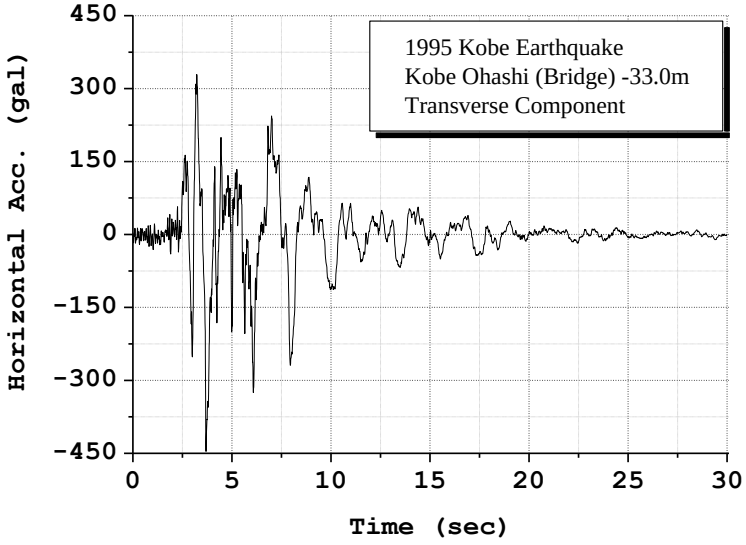

Input 2 – 2011 off the Pacific Coast of Tohoku at Tajiri MYGH06-NS Component (KIK-net)

Max: 155.2 gal

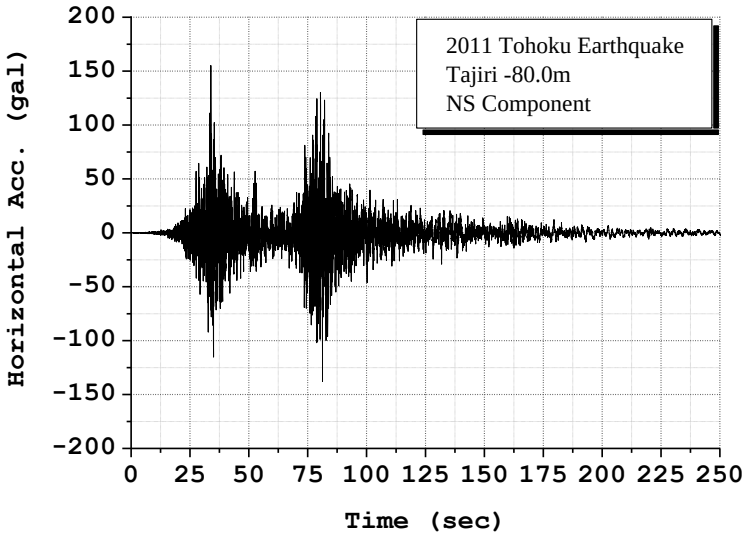

Figure 4.2. Input accelerations used for the analysis

Shown in Figure 4.3 is the acceleration response spectrum for the two input earthquake waves. The dominant period of Input 2 is around 0.2-0.3 sec, while that of Input 1 is around 1.0 sec. This indicates that the dominant period of the 2011 Tohoku Earthquake is smaller than that of the 1995 Kobe Earthquake. The other feature is that the duration of Input 2 is longer than that of Input 1 (250 sec), although its maximum acceleration is smaller than that of Input 1.

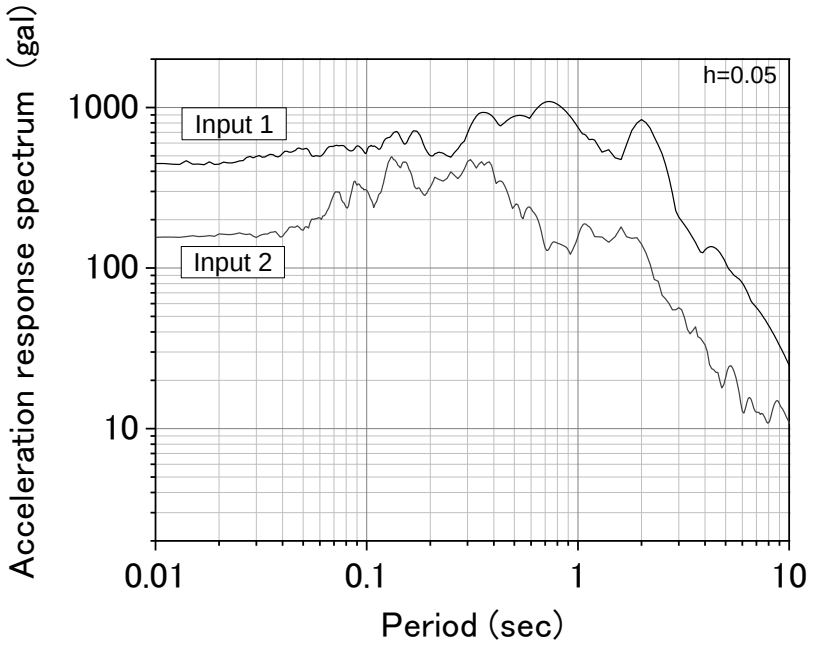

Figure 4.3. Acceleration response spectrum of the input motions

4.2.3. FEM Model

The FEM model used in this analysis consists of 880 eight-node 2D isoparametric elements. For the lateral boundary conditions, equal displacement between nodes was adopted. Figure 4.4 shows the left half of the model. In order to reduce the boundary effects, semi-infinite elements were used on the left and right ends, each being 150 meters long.

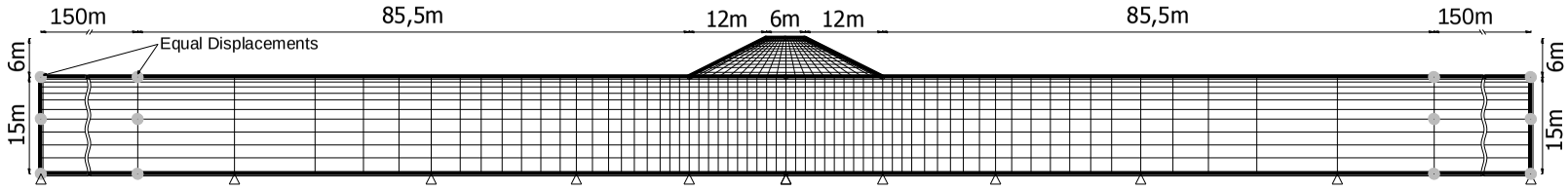

Figure 4.4. Finite element mesh and boundary conditions

4.2.4. Material Properties

Table 4.1 shows the material properties used for this analysis.

Table 4.1. Material Properties of Akita Sand and Torishima Clay

	Elasto-plastic Sand	Elasto-viscoplastic Clay
Density $\rho(t/m^3)$	1.8/2.0	1.66
Water specific weight γ_w (kn/m^3)	9.81	9.81
Coefficient of permeability K_{ws} (m/s)	2.25×10^{-4}	5.87×10^{-10}
Initial void ratio e_0	0.8	1.25
Compression index λ	0.025	0.341
Swelling index κ	0.0003	0.019
Initial elastic shear modulus ratio G_0/σ'_{m0}	761	400
Stress ratio at critical state (clay)/phase transformation (sand) M^*_m	0.909	1.24
Stress ratio at failure M^*_f	1.229	1.24
Hardening parameters B^*_0, B^*_1, C_f	5000,300,1000	500,100,5
Structural parameters n,β	0.50,50	0.30,3.6
Dilatancy parameters D^*_0,n	1.0,4.0	
Reference value of plastic strain γ_r^{p*}	0.0050	
Reference value of plastic strain γ_r^{e*}	0.003	
Viscoplastic parameter m'		24.68
Viscoplastic parameter C_1(1/s)		1.00×10^{-11}
Viscoplastic parameter C_2(1/s)		3.83×10^{-12}
Scalar hardening parameters A^*_2, B^*_2		5.9,1.8
Strain-dependent parameters α',r		10,0.4

Elasto-viscoplastic material has been used for the foundation model, while elasto-plastic material has been used for the sandy foundation and the embankment.

As for the discretization in the time domain, Newmark's β method is used as $\beta = 0.3025$ and $\gamma = 0.6$. Rayleigh's damping is also applied; it is proportional to the initial stiffness and mass matrix.

The visco-plastic parameters for clay, C_1 and C_2, are determined considering the difference between the results of the laboratory tests at Torishima, Osaka.

Cyclic strength curves for the soils are presented in Figure 4.5. Table 4.2 lists the simulated cases for different soil profiles with the clayey subsoil layers that were illustrated in Figure 4.1.

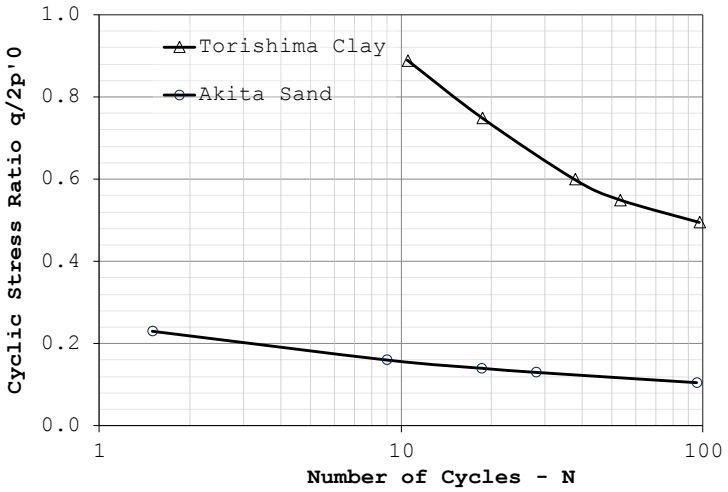

Figure 4.5. Cyclic strength curves of materials

Table 4.2. Different Analysis Cases

	Input 1 (Kobe)	Input 2 (Tohoku)
Type 1	Case 1-1	Case 2-1
Type 2	Case 1-2	Case 2-2
Type 3	Case 1-3	Case 2-3
Type 4	Case 1-4	Case 2-4

4.2.5. Initial Conditions

There is no doubt that initial conditions and loading history play an important role in the behavior of geotechnical structures. In relation to this important fact, the initial conditions of each model were carefully simulated using program ini2d11 developed by the LIQCA Research and Development Group. The initial mean effective stress and the initial pore-water pressure distributions for the model are shown in Figures 4.6 and 4.7, respectively.

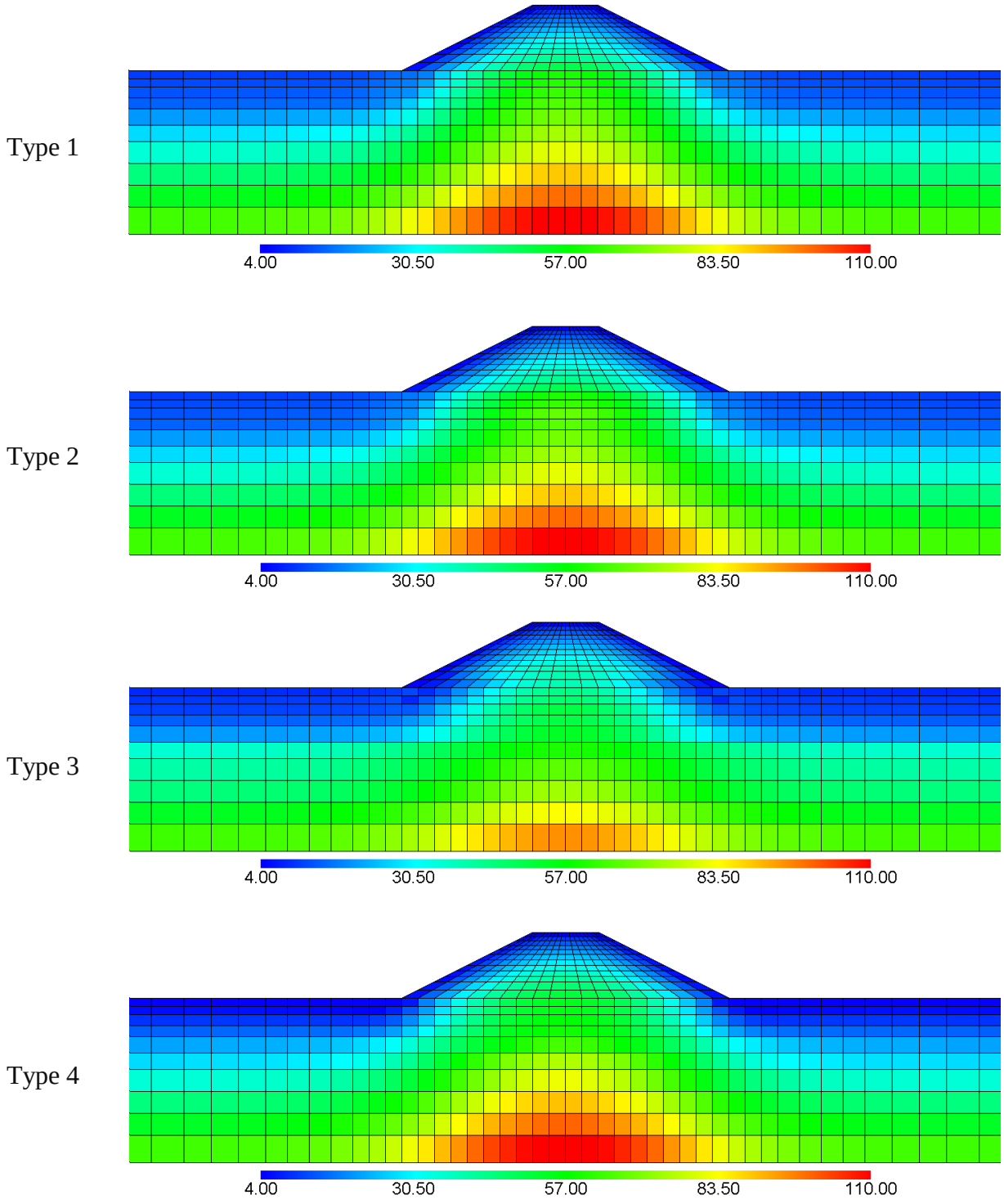

Figure 4.6. Distribution of initial mean effective stress

Type 1

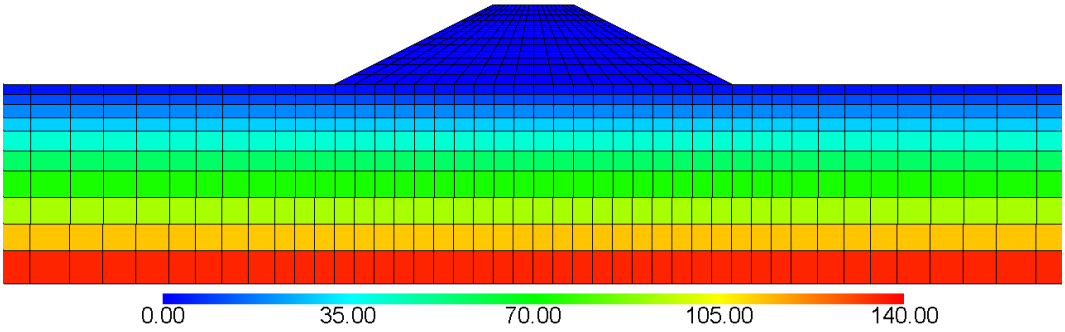

Type 2

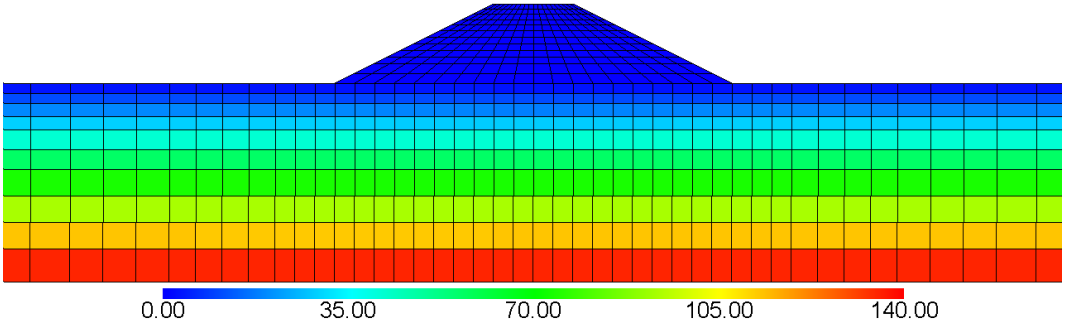

Type 3

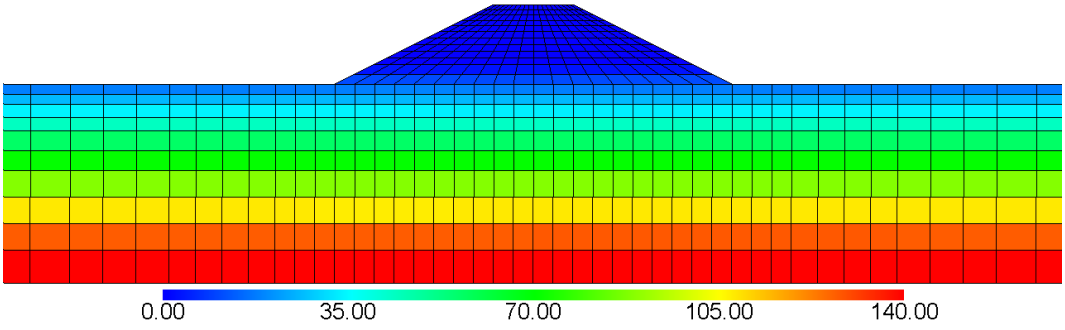

Type 4

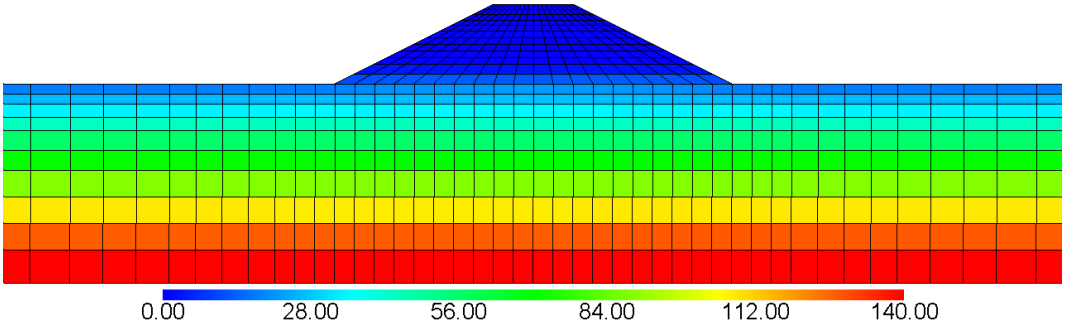

Figure 4.7. Distribution of initial pore-water pressure

4.3. Results

4.3.1. Displacement-Time Profiles

The vertical displacement-time profile at the crest of the embankment (Point 1), the horizontal displacement-time profile at the toe of the embankment (Point 2), and the vertical displacement-time profile off the toe of the embankment (Point 3) are shown in Figure 4.8 for all cases. For the cases subjected to the 1995 Kobe Earthquake, the maximum settlement at the crest occurred in Case 1-2. It is notable, however, that the difference in settlements among Cases 1-1~1-4 is not very large and none of them undergoes severe damage. On the contrary, cases subjected to the 2011 Tohoku Earthquake show large settlements which are significantly due to the liquefaction of the foundation. As expected from the different field observation reports mentioned previously, Case 2-3 experienced the most severe levels of settlement, namely, the bottom of the embankment penetrated into the soft foundation under the groundwater table and parts of the embankment body were saturated with the trapped and/or flowing water.

Case 2-4, in which the embankment lies on a thick liquefiable loose sand layer, comes in second among the settlements and is followed by Case 2-2, in third place, in which part of the embankment has settled into the foundation, but there is no groundwater table inside the body. An interesting finding is that when the foundation is not likely to liquefy (i.e., Cases 1-1 and 2-1), settlement caused by stronger earthquake waves is larger even in regard to their short durations. As illustrated in Table 4.3, this is the only case in which the Δa (compression of the embankment body) caused by the 1995 Kobe Earthquake is larger than that caused by the 2011 Tohoku Earthquake. This fact cannot be generalized for all existing soil dikes and embankments, because it clearly goes back to the frequency contents of the input waves. For the simplified cases discussed in this analysis, however, one can clearly see that stronger earthquakes with short durations are more likely to damage embankments with clayey foundations.

The other fact that can be found from the settlement-time profiles and the horizontal time-displacements is the reaction of embankments in compliance with the main shocks of the earthquake, particularly for the 2011 Tohoku Earthquake cases. For example, the displacements are obviously magnified by the main shocks of Input 2 at 33 and 81 seconds.

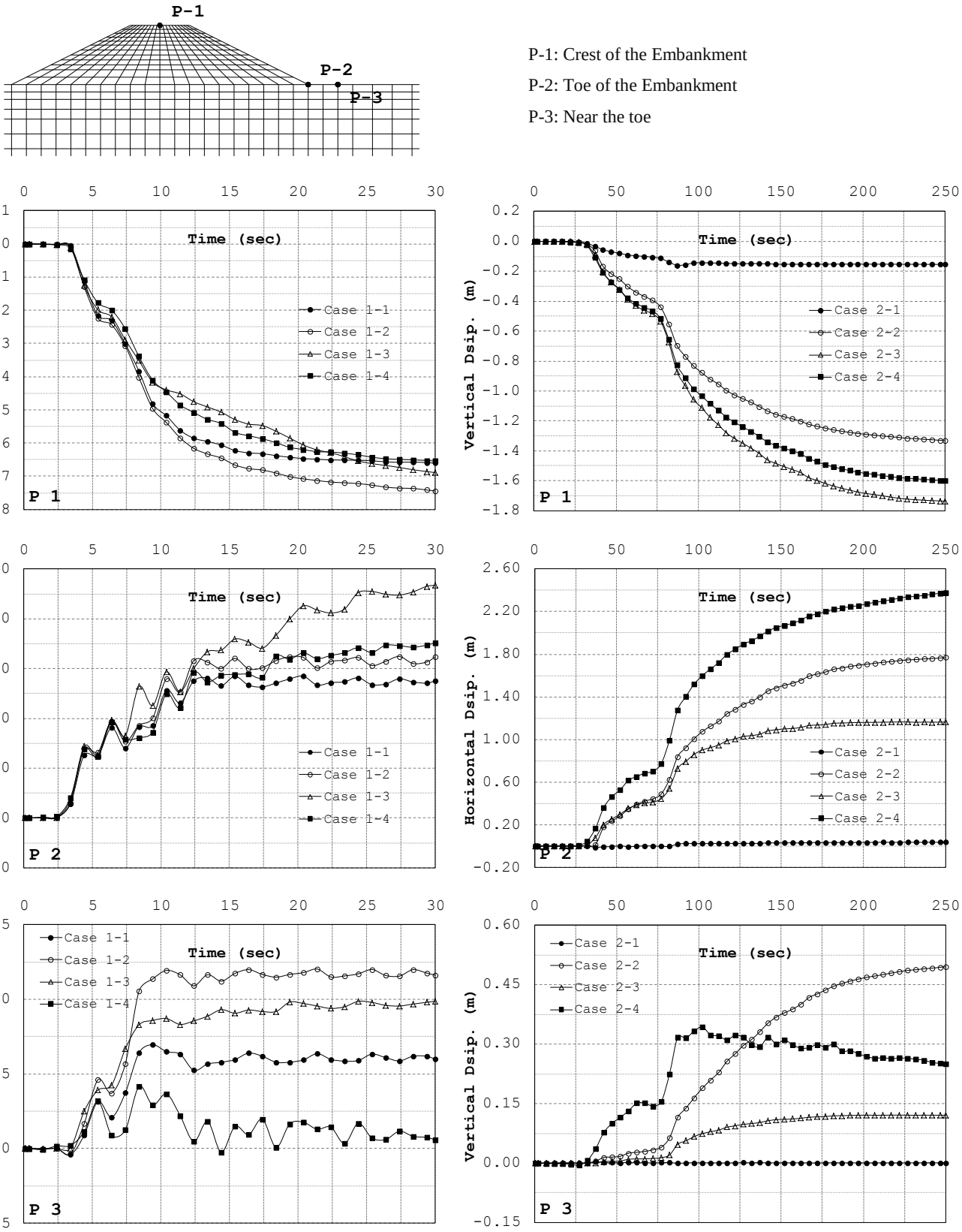

Figure 4.8. Displacement-time profiles at the crest and toe of the embankment

Table 4.3. Settlements and Compressions

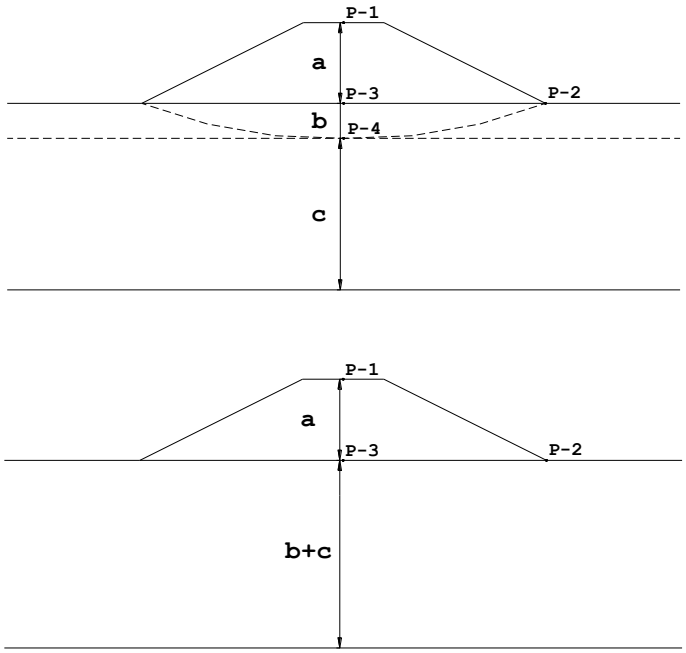

Case	2973-Y	2025-X	Δa %	Δb %	Δc %	Δ(b+c) %
Case 1-1	-0.661	0.551	3.30%	4.90%	2.72%	7.62%
Case 1-2	-0.745	0.647	3.93%	6.90%	2.69%	9.59%
Case 1-3	-0.689	0.934	4.97%	5.91%	1.95%	7.86%
Case 1-4	-0.654	0.704	3.39%	4.50%	2.71%	7.21%
Case 2-1	-0.154	0.035	2.57%	0.01%	0.00%	0.01%
Case 2-2	-1.332	1.768	16.39%	13.97%	0.00%	13.97%
Case 2-3	-1.737	1.163	16.88%	28.99%	0.00%	28.99%
Case 2-4	-1.599	2.379	10.79%	24.75%	2.67%	27.41%

dy: Vertical displacement
dx: Horizontal displacement

Another point that can be seen from the deformed shapes, the displacement-time profiles, and Table 4.3 is that most of the settlements that happen due to the 2011 Tohoku Earthquake are caused by the sandy layer rather than the soft clay layer. In all cases with a soft clay foundation (Cases 2-1~2-3), the displacements on top of the clay layer (Δc) are almost negligible. This means that in the cases with liquefiable loose sand, the clay layers remain almost intact and most of the energy is absorbed by the sand. On the contrary, in cases subjected to the 1995 Kobe Earthquake, the clayey foundation seems to share more of the total settlements of the crest.

Talking about horizontal displacements, the first point is the fact that the clay layers are less deformed by the 2011 Tohoku Earthquake with relatively smaller levels of magnitude than by a short

duration earthquake with a strong magnitude, like the 1995 Kobe Earthquake. The lateral displacement at the toe of the embankment in Case 2-1 is very small, while the displacement is as large as 55 cm in Case 1-1. For other cases, however, it is clearly seen that the flow of materials due to liquefaction in the cases subjected to the 2011 Tohoku Earthquake extends to 2.4 m for Case 2-4, in which the embankment is lying over a thick liquefied sand layer. For Case 2-3, in which the most severe settlements are seen, a bulging mode appears at the bottom of the embankment, but its lateral displacements are far smaller than those of Case 2-2, which comes in second with a lateral displacement of 1.8 m. This proves that the trapped water layer inside the embankment body causes a different mode of failure as it magnifies the crest settlements and causes bulging in the body rather than spreading.

3.0 meters to the right off the toe of the embankment, it is seen that the heaving behavior of this point is interesting. Case 2 shows the maximum heaving for both input earthquakes. This is practically considered to be due to the embankment penetration into the subsoil. Another interesting fact is that in Case 2-4, in which the sandy layer is almost completely liquefied, heaving is much greater than in the other cases for which this layer is not liquefied. While the heaving in Case 2-1 remains less than a centimeter, it heaves 25cm in Case 2-4. Case 2-3, in which the most severe damage occurs, does not show a large lateral flow or heaving at the toe. The heaving in Case 1-3 is less than 10 cm. Finally, since clay foundation layers do not absorb any significant energy or deformation in the 2011 Tohoku Earthquake, the heaving in Case 2-1 is seen to be absolutely negligible.

4.3.2. Deformations and Liquefaction

In the present section, the distribution of deformation vectors, the effective stress decreasing ratio (ESDR), the accumulated plastic shear strain ($\gamma^p = \int \left(de_{ij}^p de_{ij}^p \right)^{1/2}$), and the plastic volumetric strain (ε_{kk}^p) are presented for the deformed mesh.

It must be mentioned that since the behavior of the model at specific times, like exactly before and after the main shocks, is of great importance, the distribution of the parameters has been extracted at many points.

Figures 4.9 and 4.10 show the important time steps in the 1995 Kobe Earthquake and the 2011 Tohoku Earthquake, respectively.

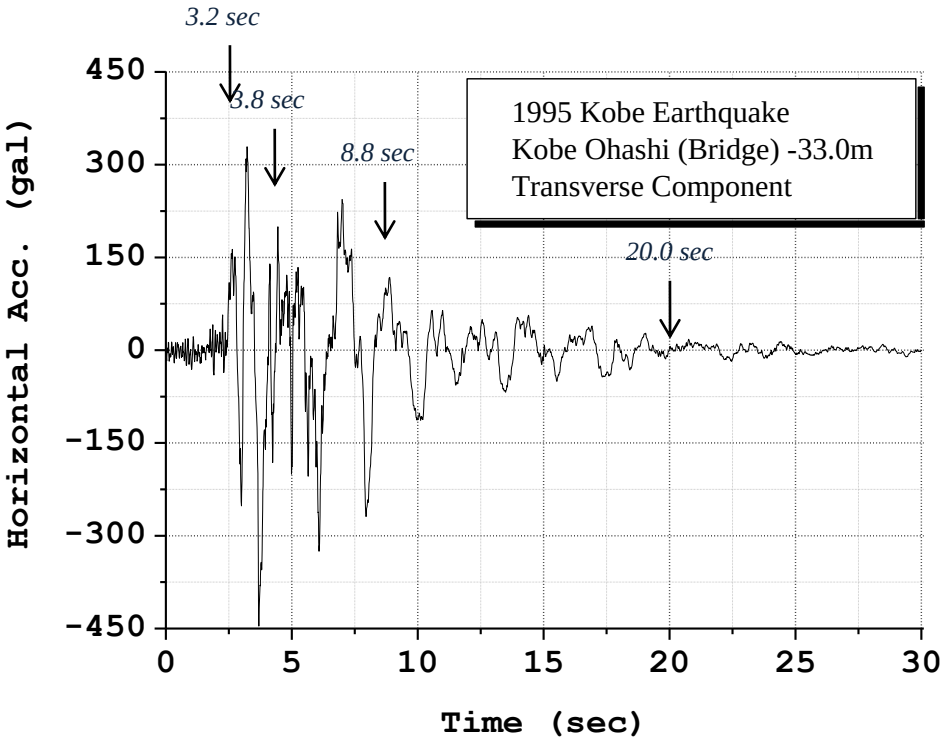

Figure 4.9. Important time steps of 1995 Kobe Earthquake

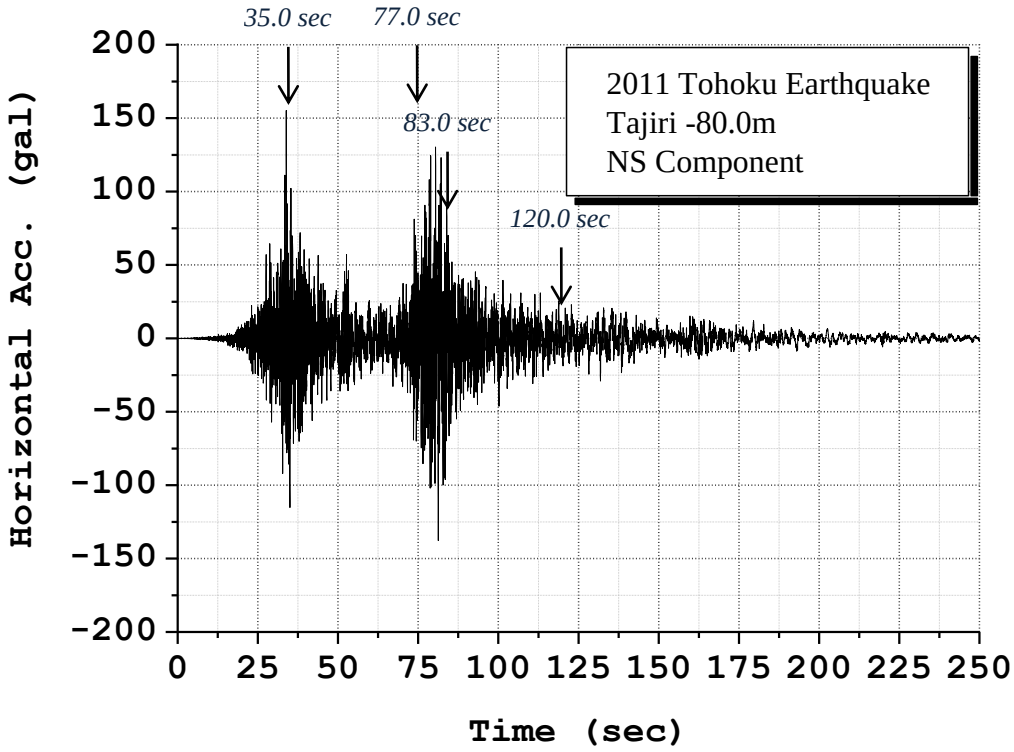

Figure 4.10. Important time steps of 2011 Tohoku Earthquake

- ***Displacement vectors, accumulated plastic strain, and ESDR for Cases 1-1~1-4***

Figures 4.11 ~ 4.17 present the distributions of the displacement vectors, the accumulated plastic shear strain, the plastic volumetric strain, and the effective stress decreasing ratio for the cases subjected to the 1995 Kobe Earthquake (Cases 1-1~1-4). A unified scale has been used for all cases.

Case 1-1 shows mobilization for a deep slide on the right side which continues to the left slope. It means circular sliding and inclined crack shoulders are to be expected. Nevertheless, the main pattern of deformation is subsidence with little damage to the embankment. The accumulated plastic shear strain is not localized inside the embankment body; most of the contractions and the plastic volumetric strain are localized in the slopes.

In Case 1-2, a change in directions can be seen in vectors on the left slope; it continues until the deep right embankment toe. The vectors change direction in the middle of the left slope; this means that sliding initiates from there. The saturated part of the embankment body that has settled in the foundation does not reach liquefaction. However, most of the accumulated plastic shear strain is localized in the saturated bottom of the embankment. The contracted zones can be seen in the slopes and the crest. The damage in this case is not considerable either.

Case 1-3 also shows a deep slide initiating from the top of the left shoulder and continuing all the way to beneath the right toe. However, the red color vectors show that the amount of sliding on the right side is more severe. Although the green vectors start from the left shoulder and continue very deep under the right toe, which implies a lateral displacement of the body to the right, it is the right slope that shows more displacements starting from the middle of the crest up to the slightly bulged right toe. This case shows the maximum lateral displacements among the four cases. The saturated part of the embankment in Case 1-3 does not reach liquefaction; however, the localization of accumulated plastic strain can be seen in the saturated bottom and toe of the embankment which continues all the way to the slopes especially on the left side. The distribution of the plastic volumetric strain shows dilation fields in the embankment body that are inclined toward the center and create a wedge shape near the crest.

Case 1-4 shows no severe damage to the embankment body. However, the whole embankment has uniformly slumped into the liquefied ground which seems to be more damaged than the embankment body. Since the ground underneath the center of the embankment has not completely liquefied, the displacements are concentrated on the sides; this means that the ground around the embankment will show heaving and deformations. The saturated sandy foundation in this case is liquefied, although the distribution of liquefaction beneath the embankment body does not reach liquefaction because of the

higher confining pressures. Therefore, most of the localizations of the plastic shear strain and the plastic volumetric strain can be seen in the foundation rather than inside the embankment body.

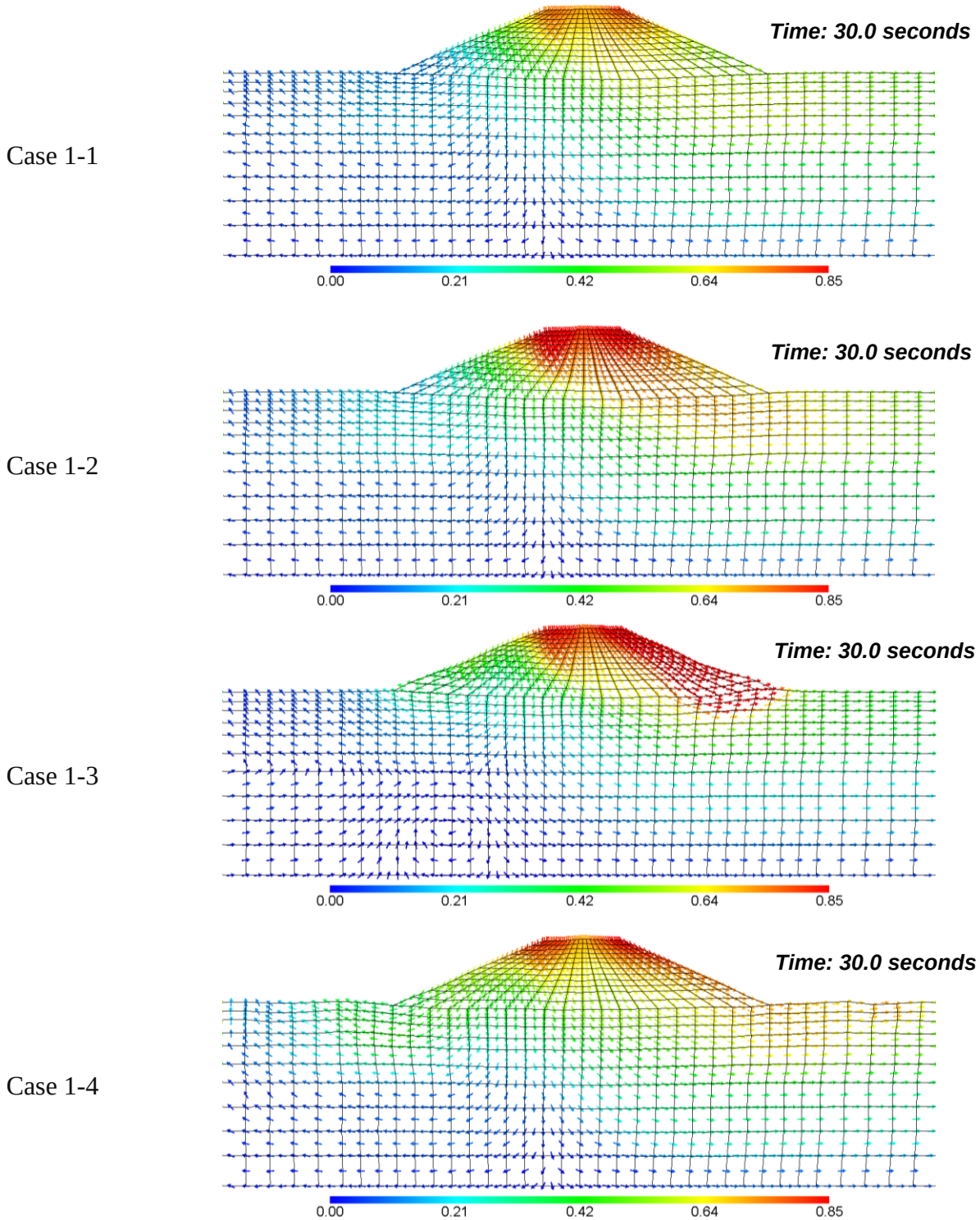

Figure 4.11. Distribution of displacement vectors for Cases 1-1 ~ 1-4, (unit: m)

Case 1-1

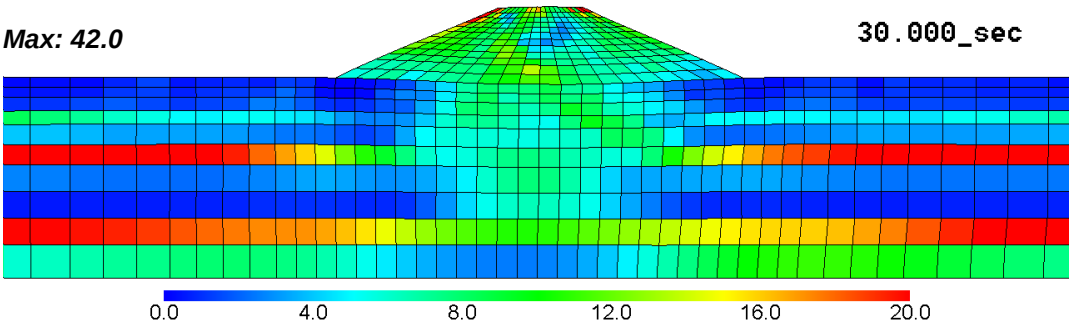

Case 1-2

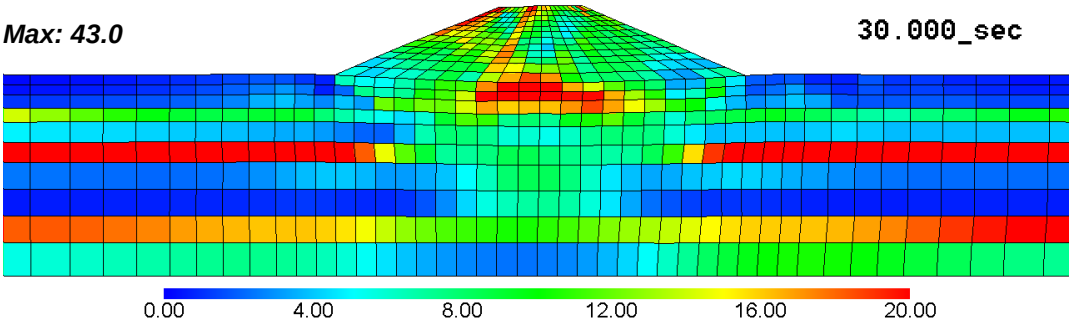

Case 1-3

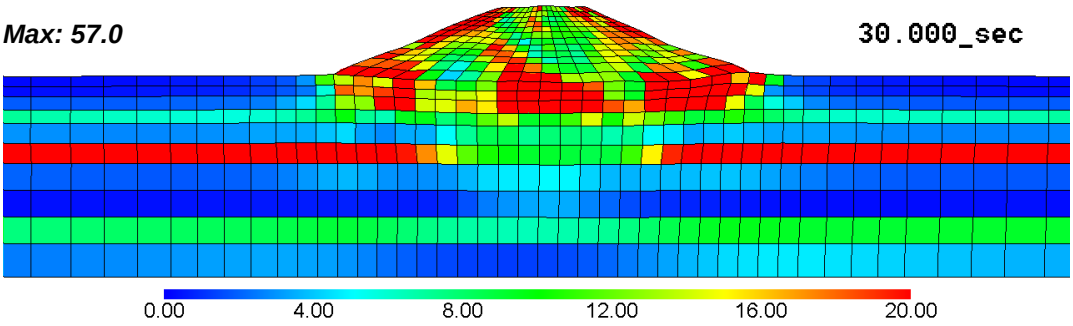

Case 1-4

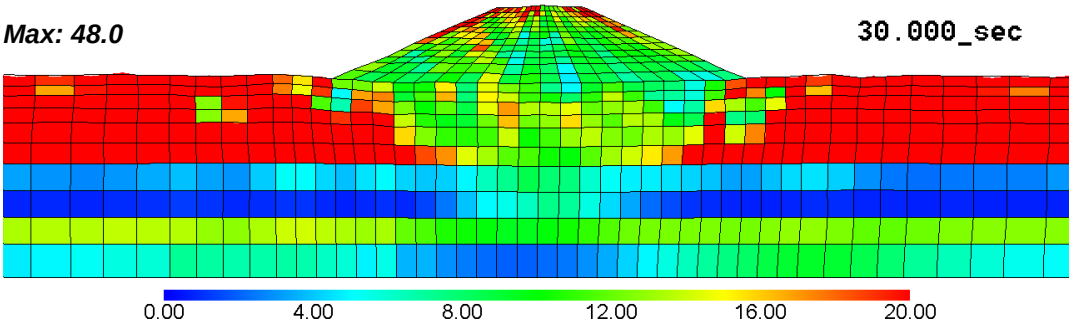

Figure 4.12. Distribution of accumulated plastic shear strain for Cases 1-1 ~ 1-4, (unit: %)

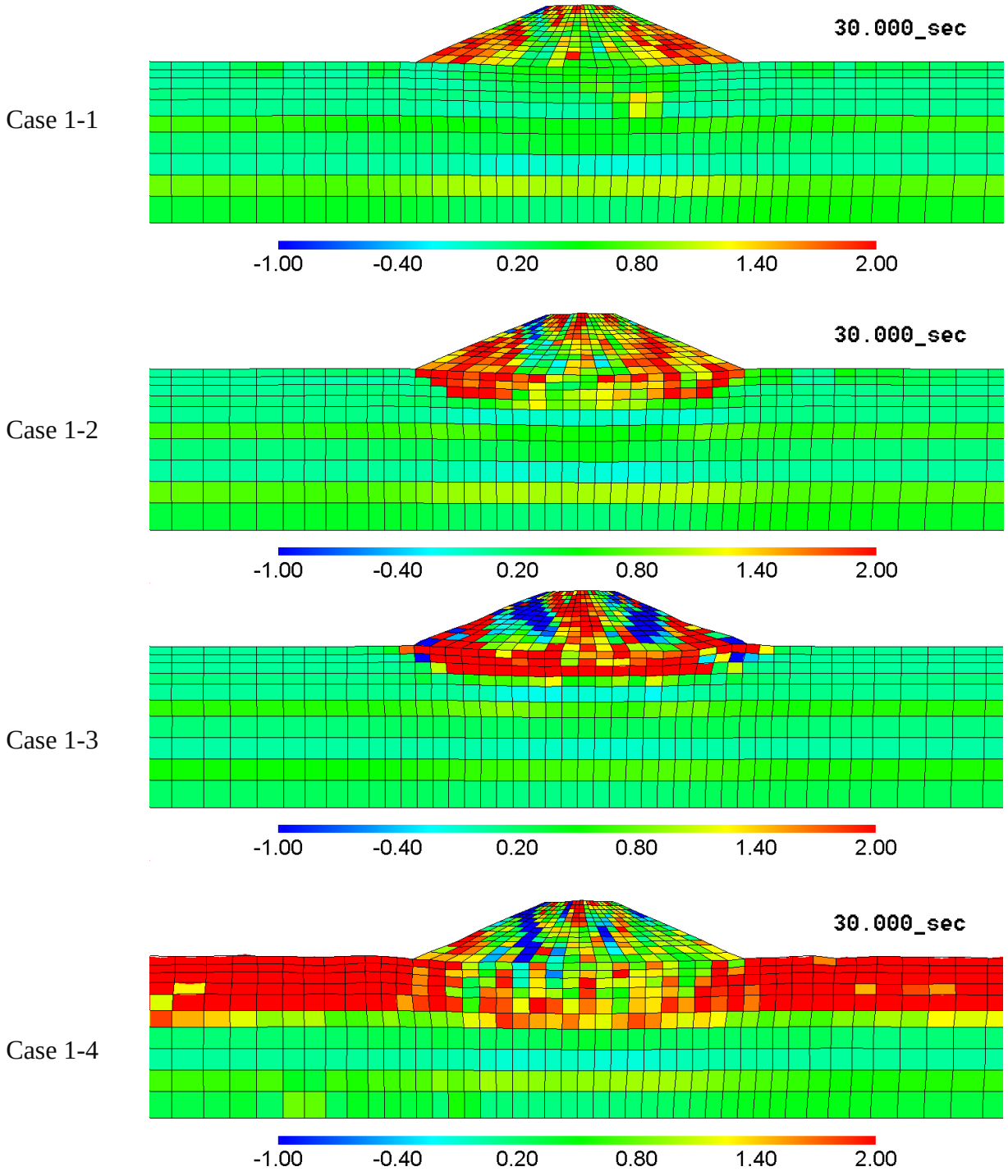

Figure 4.13. Distribution of plastic volumetric strain for Cases 1-1 ~ 1-4, Time = 30.0 sec

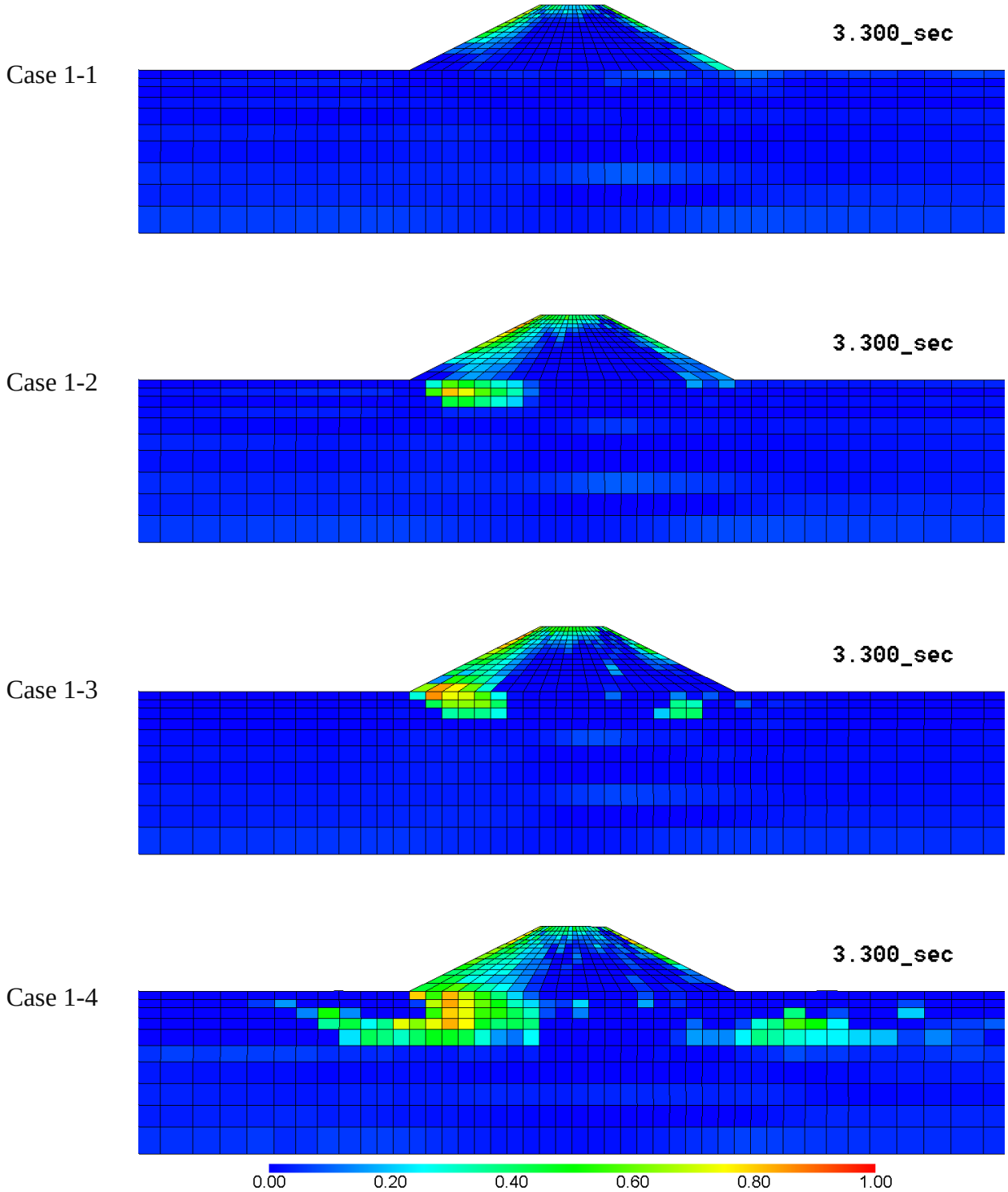

Figure 4.14. Distribution of effective stress decreasing ratio for Cases 1-1 ~ 1-4, Time = 3.30 sec

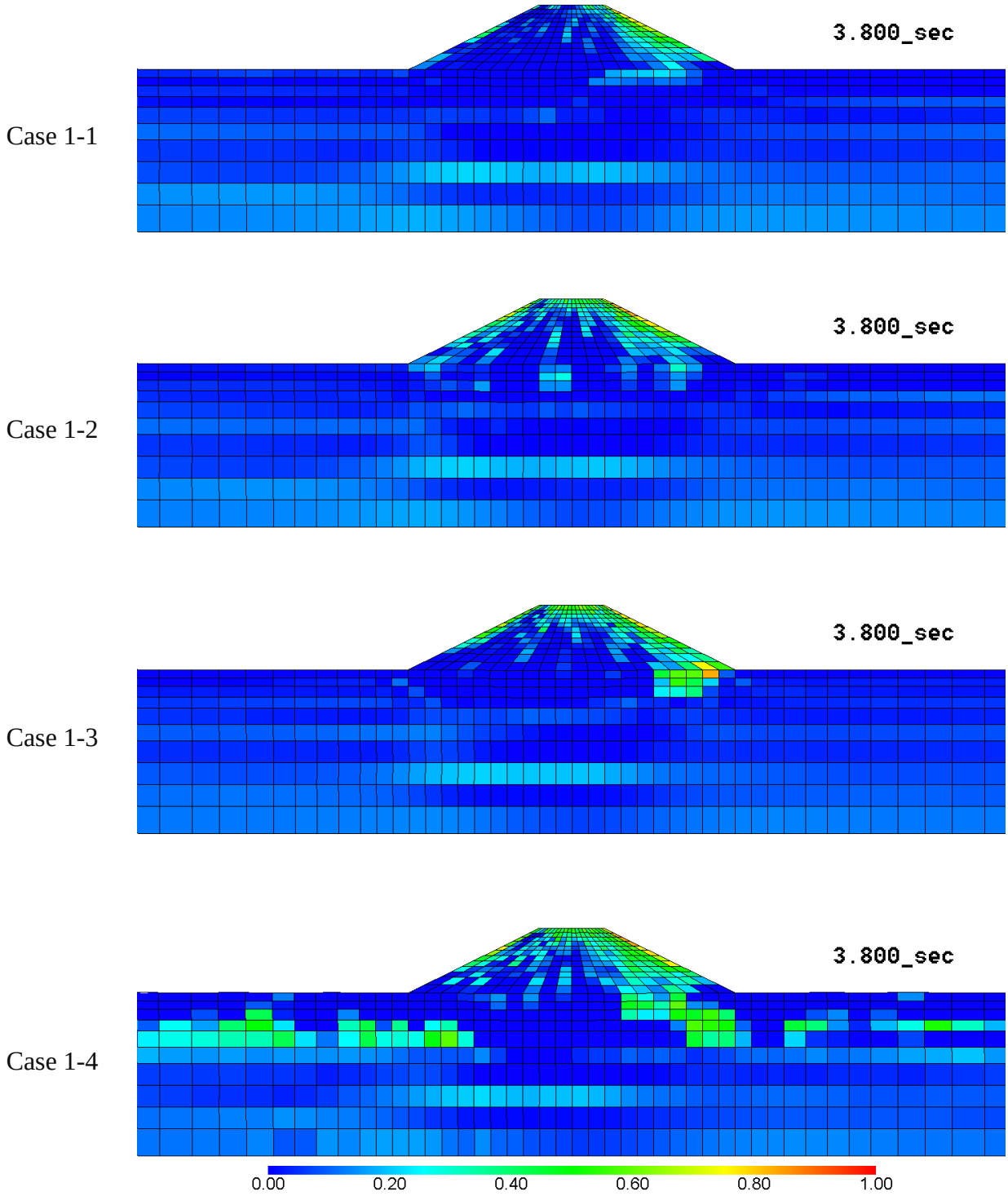

Figure 4.15. Distribution of effective stress decreasing ratio for Cases 1-1 ~ 1-4, Time = 3.80 sec

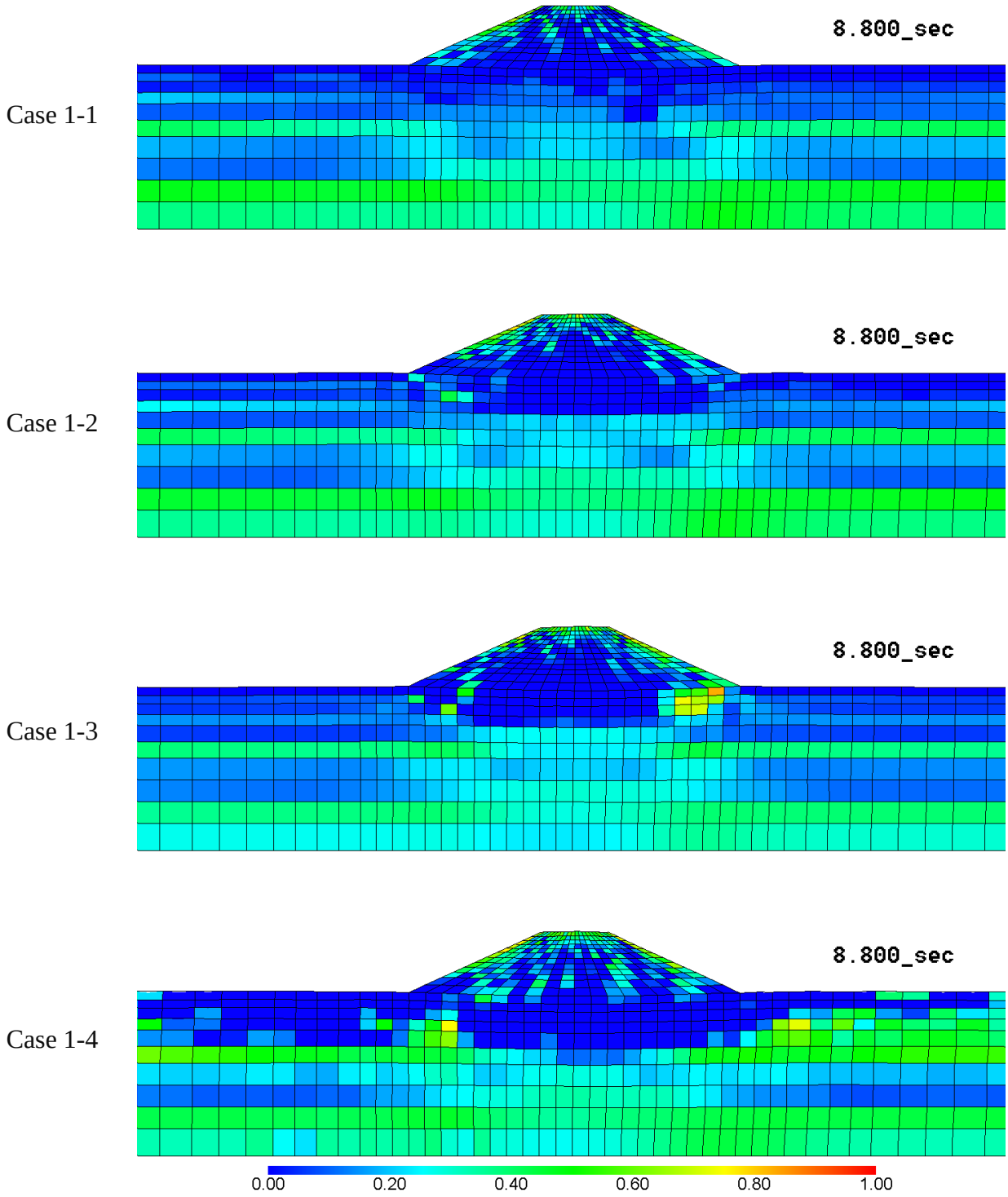

Figure 4.16. Distribution of effective stress decreasing ratio for Cases 1-1 ~ 1-4, Time = 8.80 sec

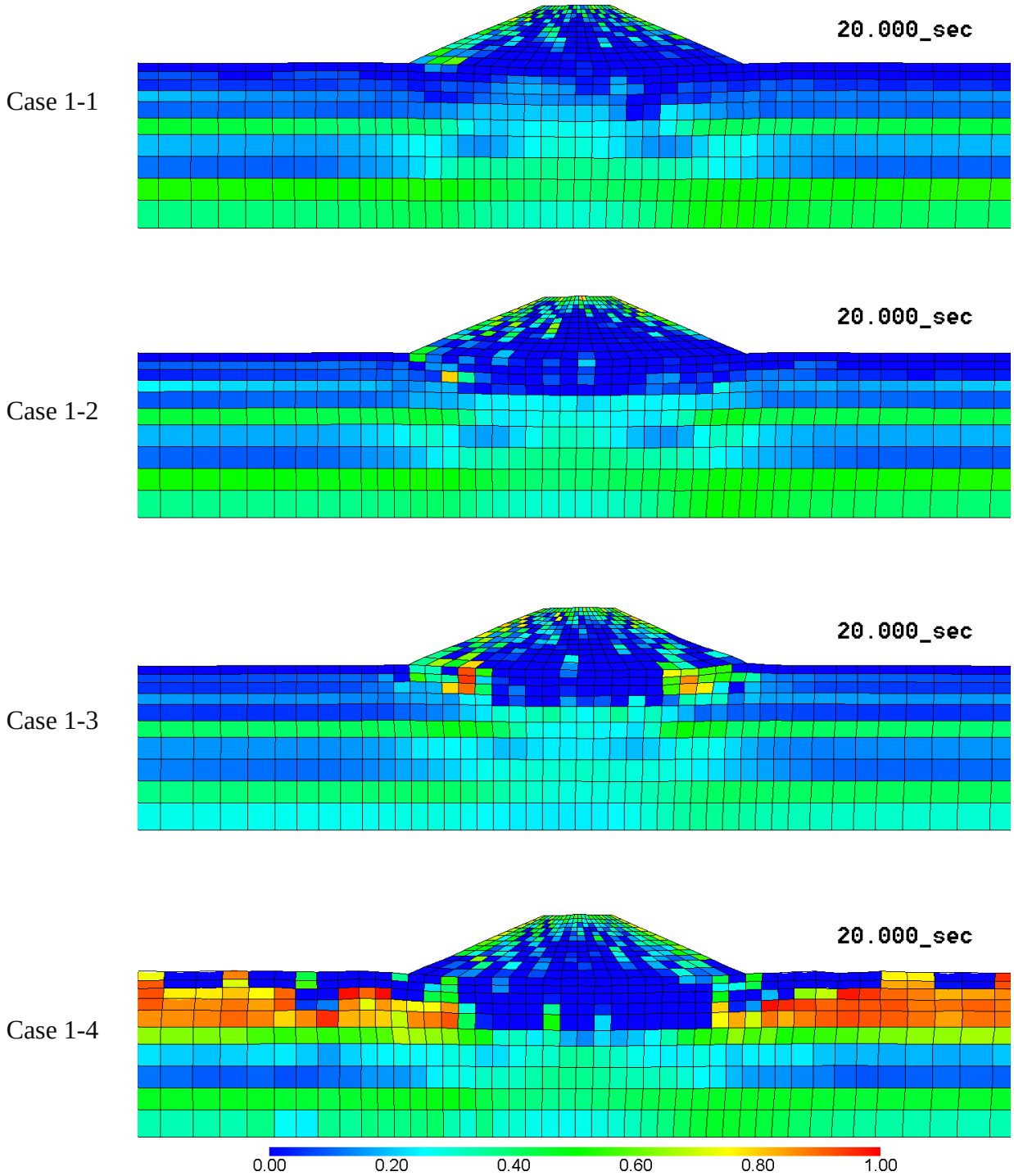

Figure 4.17. Distribution of effective stress decreasing ratio for Cases 1-1 ~ 1-4, Time = 20.0 sec

- ***Displacement vectors, accumulated plastic strain, and ESDR for Cases 2-1~2-4***

Figures 4.18~4.24 show the displacement vectors, the accumulated plastic shear strain, the plastic volumetric strain, and the effective stress decreasing ratio for the cases subjected to the 2011 Tohoku Earthquake (Cases 2-1~2-4).

Among Cases 2-1~2-4, the cases subjected to the 2011 Tohoku Earthquake, Case 2-1 shows the least damage. As discussed previously, the clayey ground remains almost intact and shows very small deformations. The embankment body does not show severe damage in this case either. The failure mode seen here is a shallow sliding on the left and right slopes, and the deformations remain in the small range. The slight damage in this case can be easily fixed. Most of the accumulated plastic shear strain and plastic volumetric strain are localized on the slopes.

In Case 2-2, the liquefied ground under the embankment center and toe contribute a lot to the lateral flow of materials; this causes tension fields and vertical cracks in the embankment body. However, it can be easily seen that these cracks do not follow the circular sliding paths that are assumed in practical soil mechanics. The embankment is damaged both on the slopes and inside, and obvious localizations can be seen among the crest and slopes. However, since the embankment itself is not liquefied, no apparent heaving can be seen inside the body of the embankment near the toes. The saturated bottom of the embankment is liquefied in this case. Moreover, a localization of the plastic shear strain can be seen in the liquefied sand at the bottom of the embankment which continues vertically or inclines toward the crest.

In agreement with what has been reported from the field observations, Case 2-3 shows the most severe damage. As with what happened in Case 2-2, this embankment is flowing on the liquefied sand layer. Moreover, the trapped water inside the embankment body causes liquefaction and severe deformation in the toes. The crest and the shoulders are separated and inclined cracks move toward the center. However, since the lateral displacements of the toes are not as large as those of the previous case, the tension field inside the body is less strong. It can be said that the embankment is severely damaged and obvious openings can probably be seen on the ground. The localization of the plastic shear strain in the saturated bottom of the embankment continues to be inclined toward the slopes, and the plastic volumetric strain shows a wedge shape of localization near the crest.

In Case 2-4, the embankment is lying over a liquefiable sandy layer. The liquefaction and the movements in this layer cause lateral displacements in the toes. In addition, the two slopes can easily slide on the liquefied bed to create deep sliding modes. Moreover, the displacement vectors explain the inclined localizations toward the center, reported by Sasaki et al. (1994) and Oka et al. (2012), and can be seen in this case too. This is also evident in the distribution of the plastic shear strain and the plastic

volumetric strain. Nevertheless, most of the localizations are concentrated in the liquefied sandy foundation.

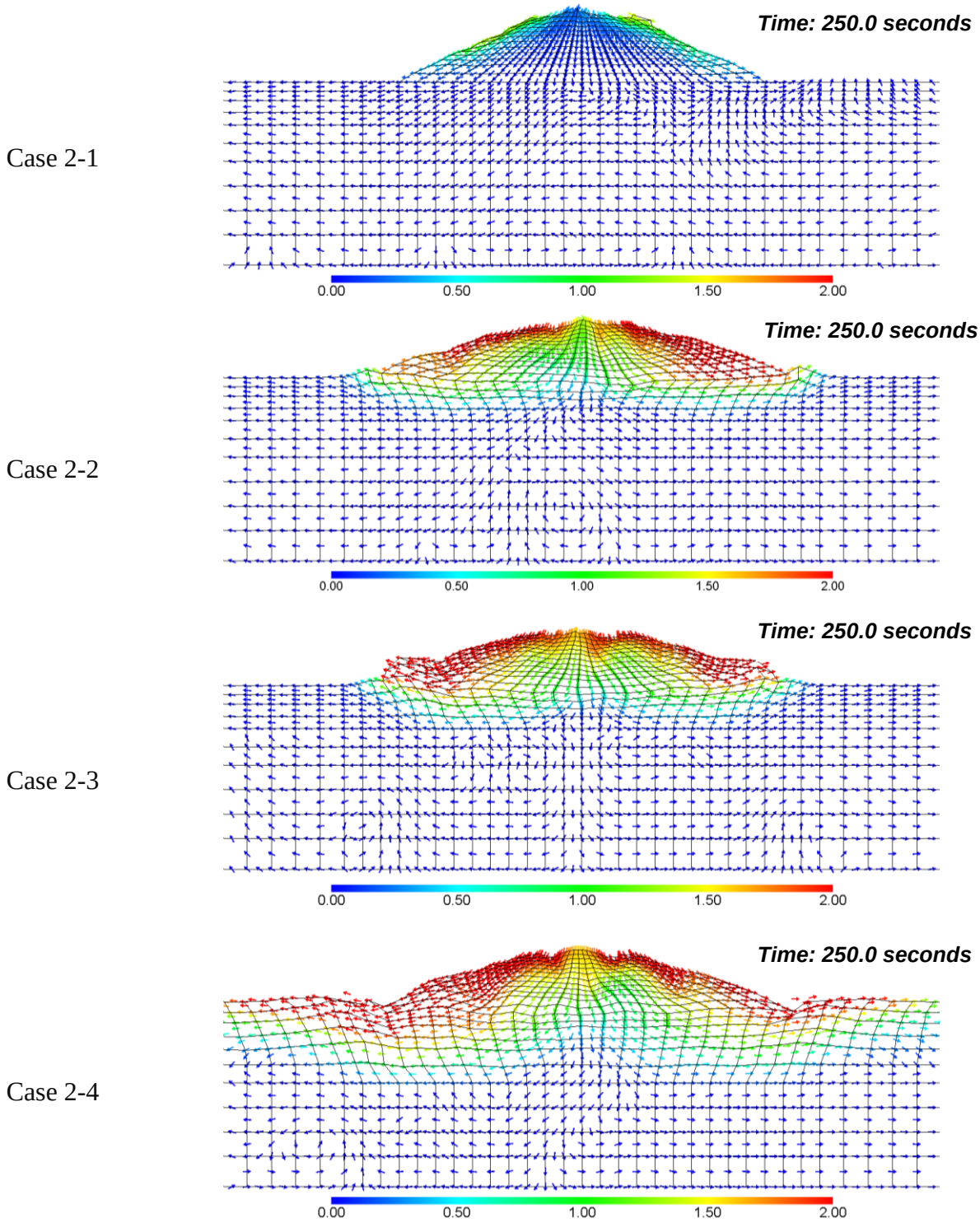

Figure 4.18. Distribution of displacement vectors for Cases 2-1 ~ 2-4, (unit: m)

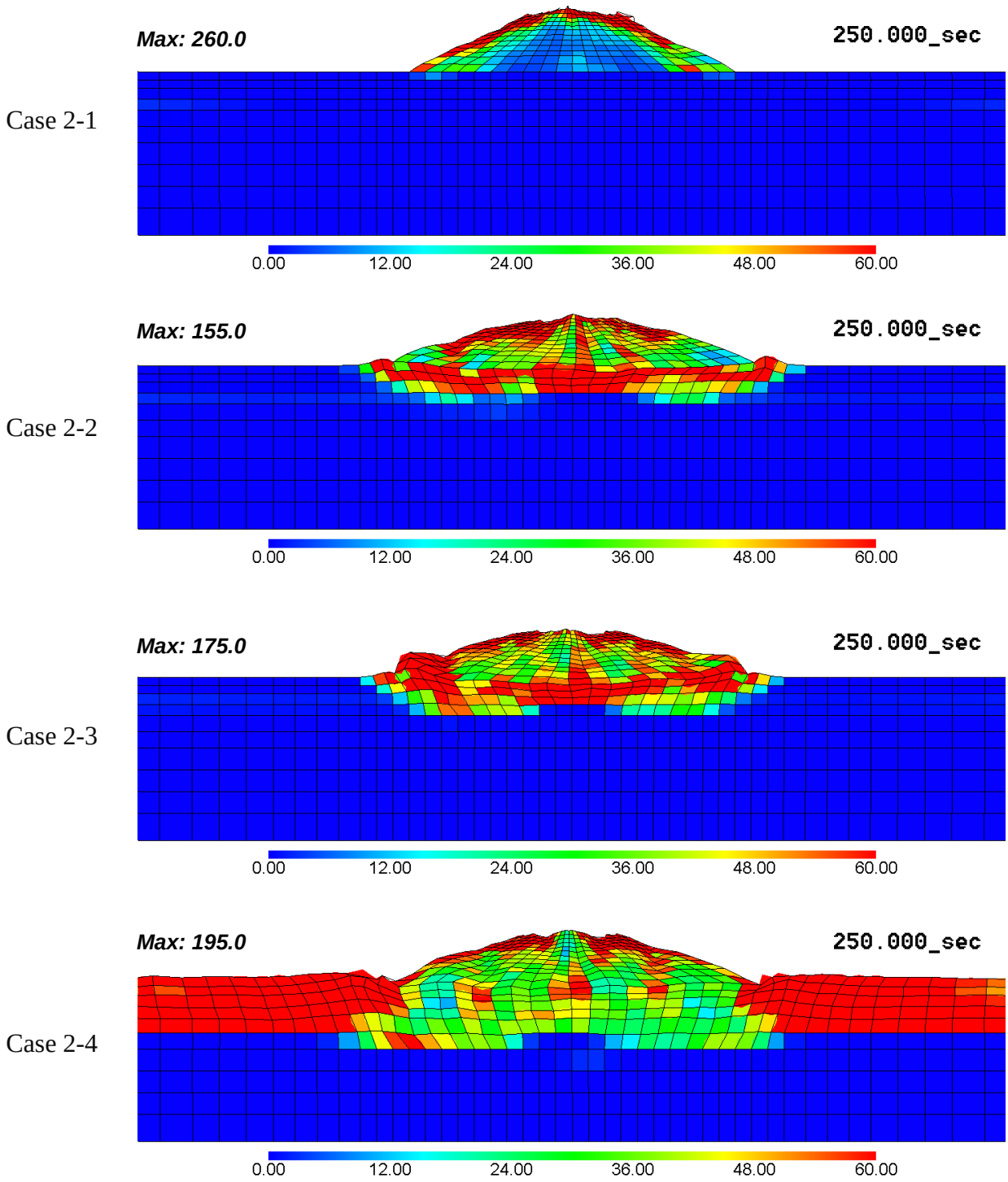

Figure 4.19. Distribution of accumulated plastic shear strain for Cases 2-1 ~ 2-4, (unit: %)

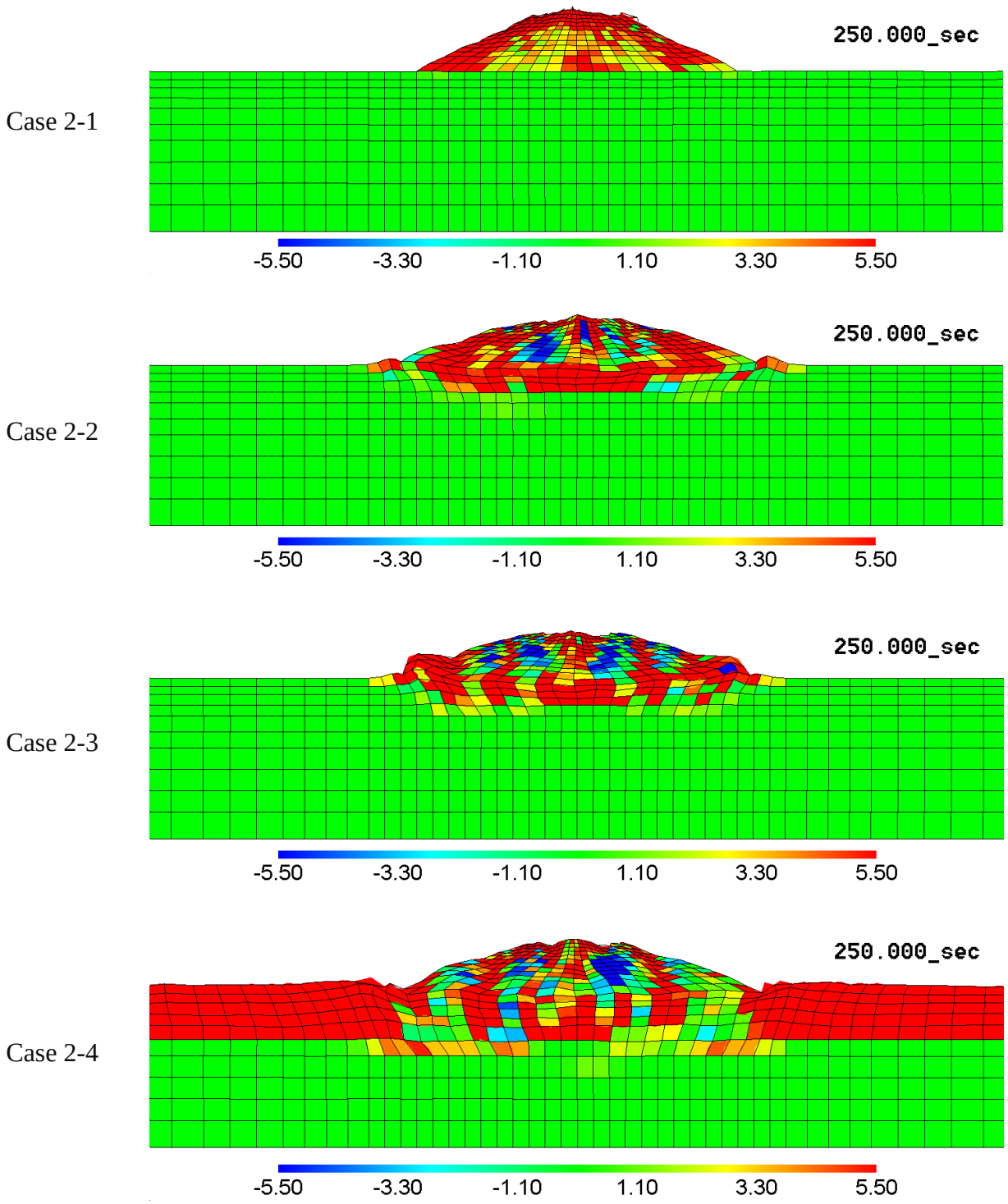

Figure 4.20. Distribution of plastic volumetric strain for Cases 2-1 ~ 2-4, Time = 250.0 sec

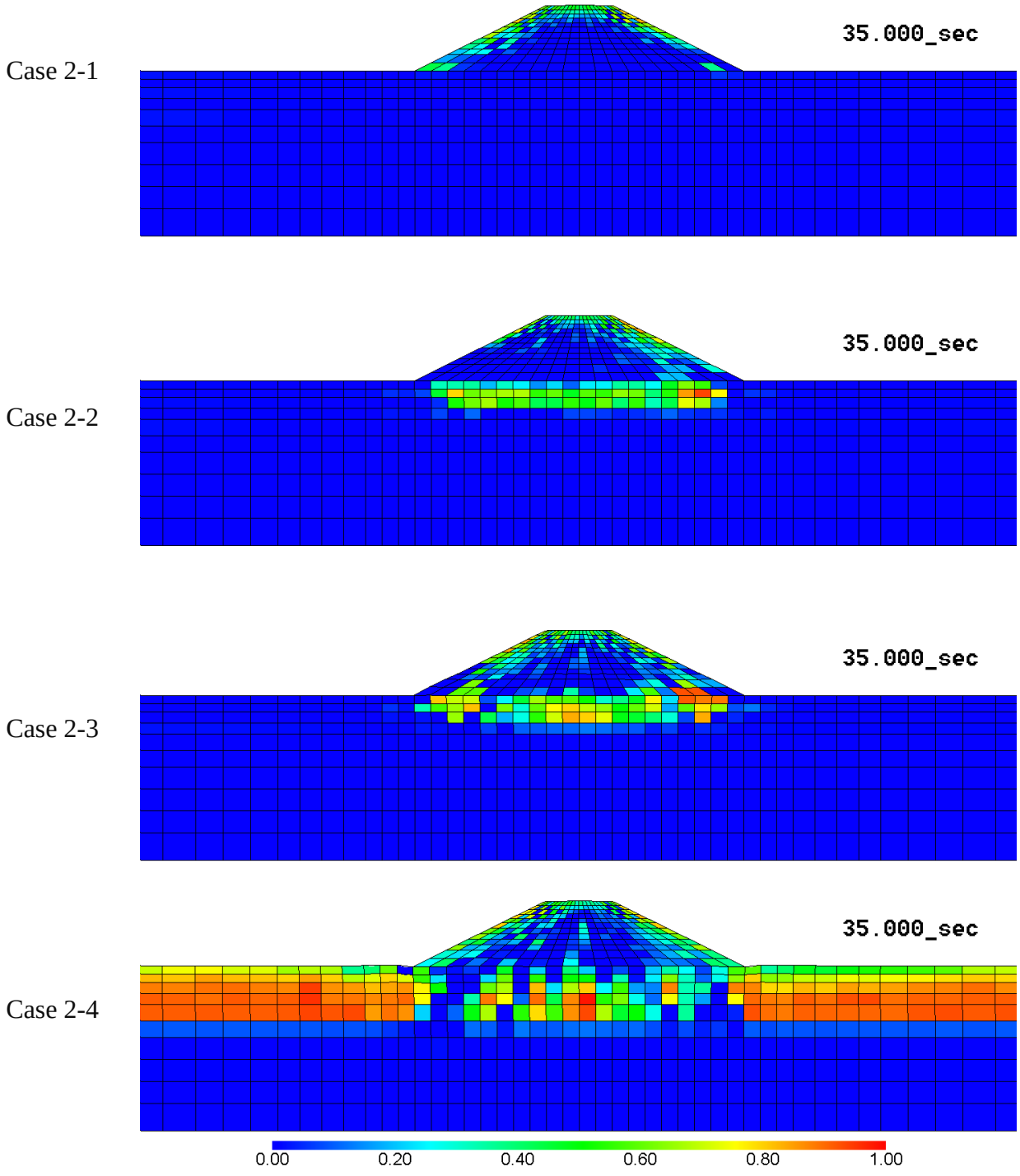

Figure 4.21. Distribution of effective stress decreasing ratio for Cases 2-1 ~ 2-4, Time = 35.0 sec

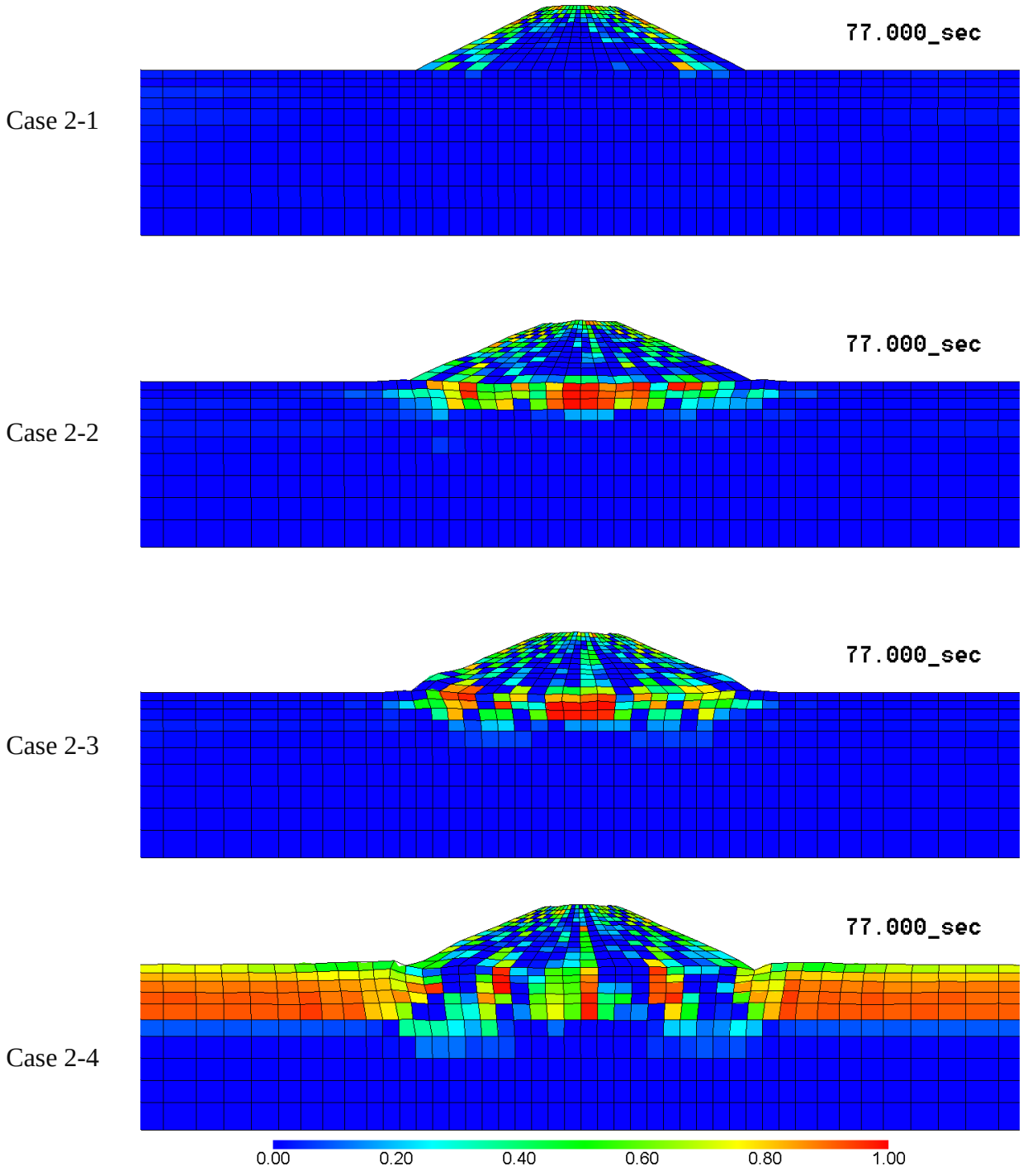

Figure 4.22. Distribution of effective stress decreasing ratio for Cases 2-1 ~ 2-4, Time = 77.0 sec

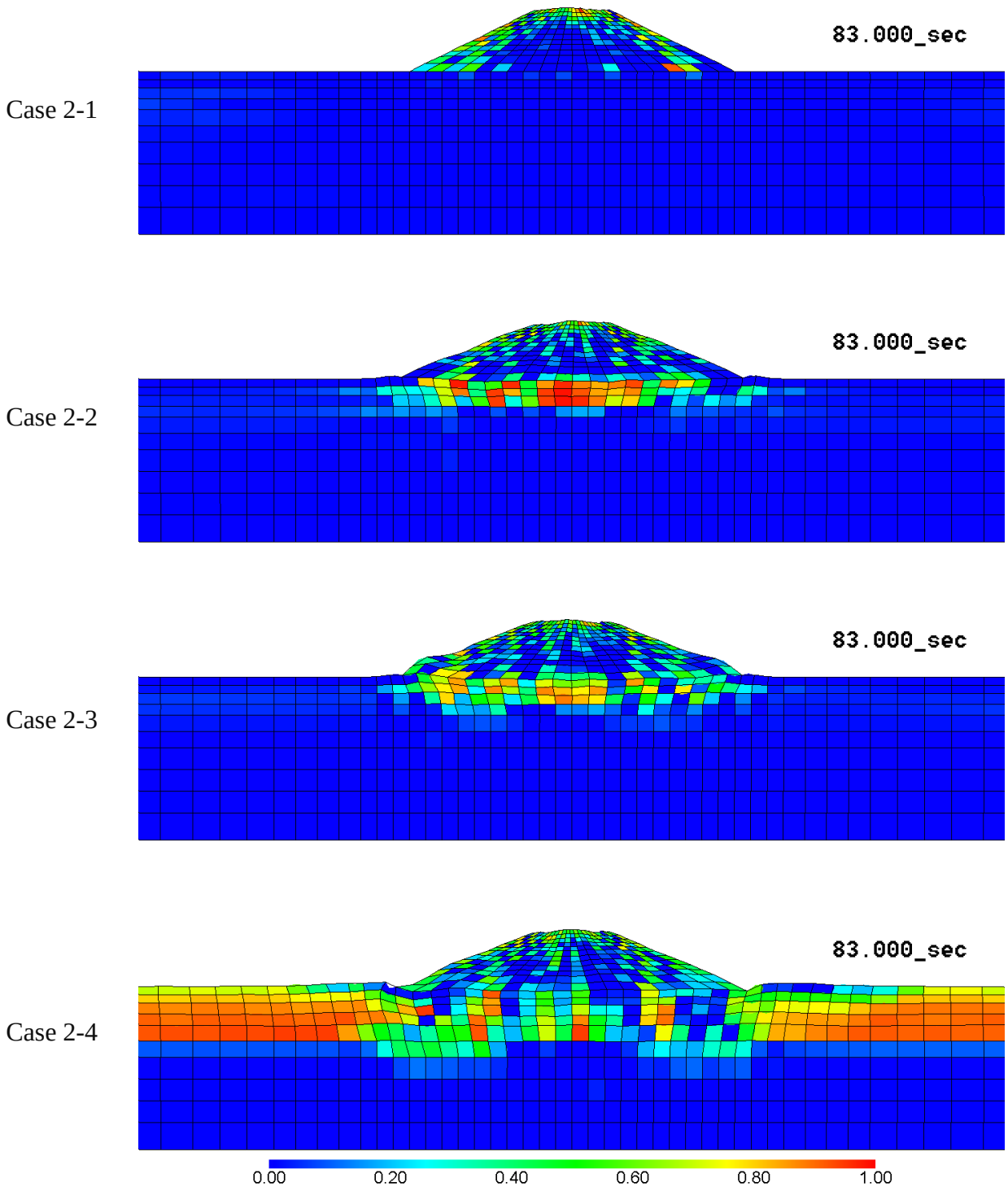

Figure 4.23. Distribution of effective stress decreasing ratio for Cases 2-1 ~ 2-4, Time = 83.0 sec

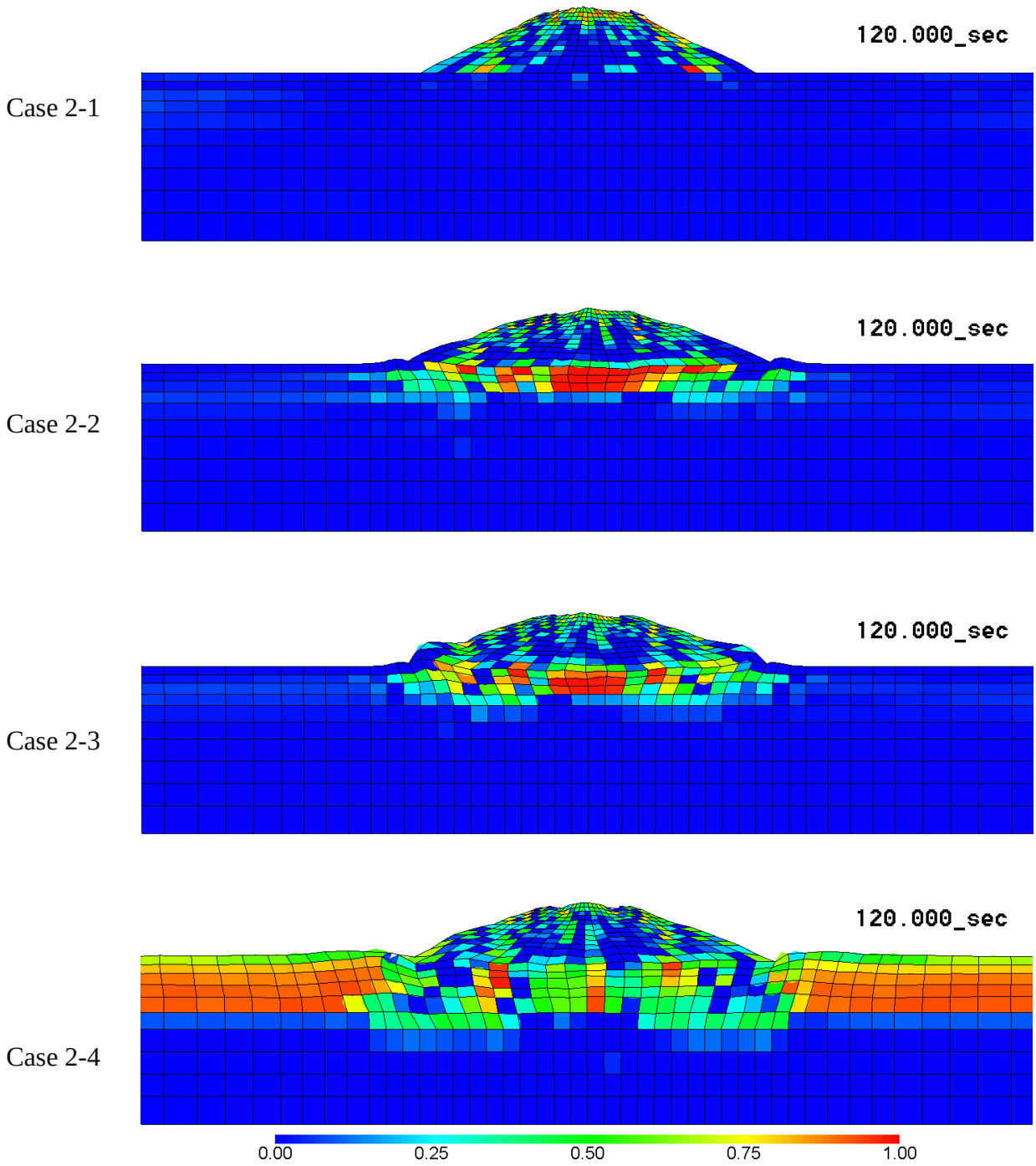

Figure 4.24. Distribution of effective stress decreasing ratio for Cases 2-1 ~ 2-4, Time = 120.0 sec

4.3.3. Distribution of strain in the embankment for Case 2-3

In order to discuss the deformation of the embankment, we will see the distribution of strain in Case 2-3. In the Type 3 ground, the embankment has settled into the saturated foundation and there is a groundwater table inside the embankment body. Since this type of behavior corresponds well to the severe damage caused by the 2011 Tohoku Earthquake, we hereby present a more detailed distribution of strain in the deformed embankment after the end of the 2011 Tohoku Earthquake. Figure 4.25 shows the Accumulated plastic shear strain in the magnified embankment for Case 2-3.

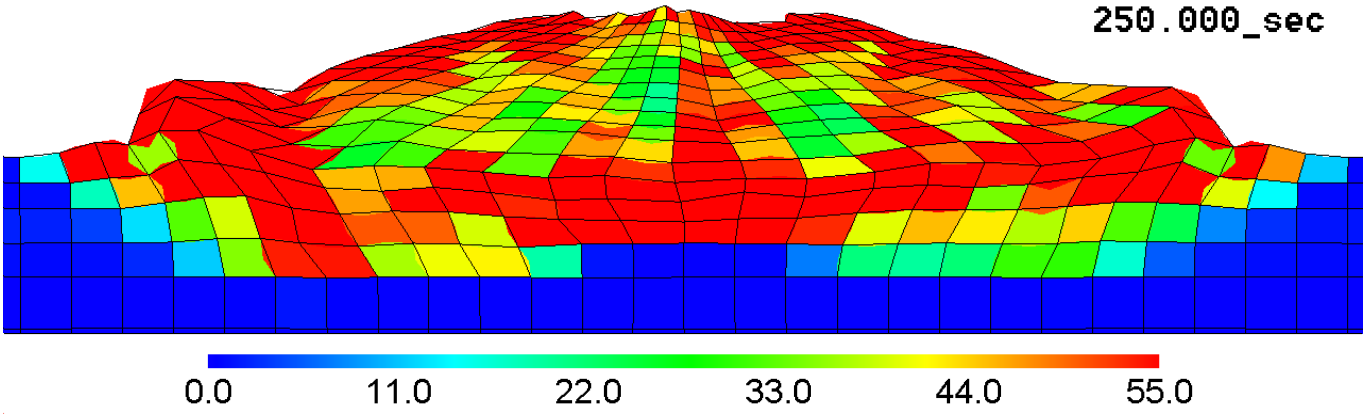

Figure 4.25. Accumulated plastic shear strain $\gamma^p = \int \sqrt{de_{ij}^p de_{ij}^p}$ *(%), Case 2-3*

Figure 4.26 shows the plastic volumetric strain in the magnified embankment for Case 2-3.

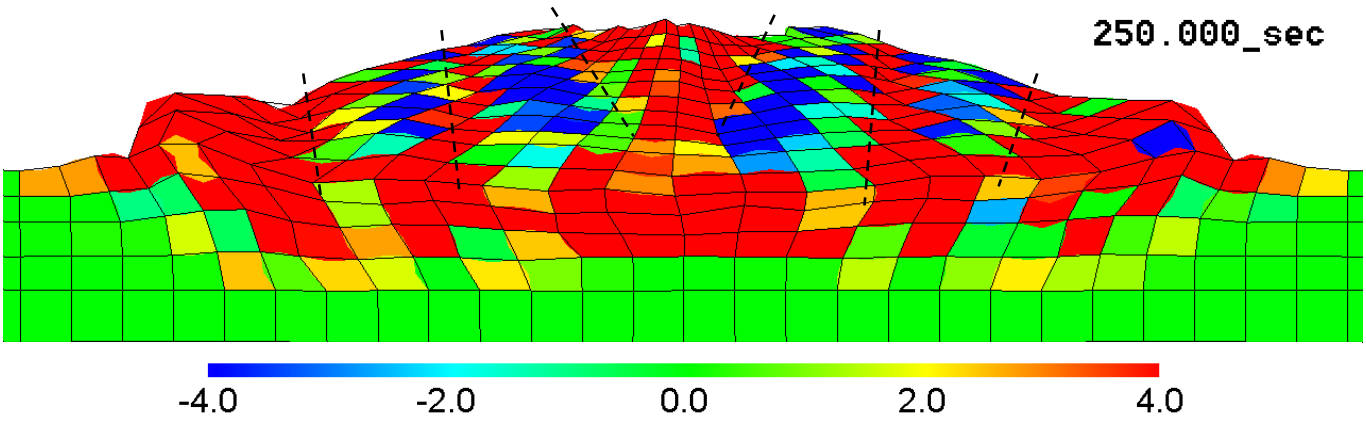

Figure 4.26. Plastic volumetric strain ε_v^{vp} *(%), Case 2-3*

**

Positive Values (Red): Contraction
Negative Values (Blue): Dilation

As can be seen here, the inclined localizations of shear strain start from the top of the shoulders and continue toward the center. A discontinuity of deformation between the crest and the shoulder can be seen especially on the left shoulder. The lateral displacements of the toes are not so large and instead a huge upward bulge can be seen on both toes. It can be said that the embankment is severely damaged and obvious openings can probably be observed on the ground. However, seeing the accumulated volumetric embankments provides a better idea about the dilation or the extension fields inside the embankment.

Contraction can be seen in the lower half of the embankment and foundation. Inclined dilation fields and localized contraction can also be observed inside the embankment body. Moreover, a distinct contraction triangular or wedge shape part is seen in the crest. As described by Sasaki et al. (1994) and Kaneko et al. (1995), these inclined dilation fields are the main reasons for the development of the wedge shape separation in the crest. Schematic Figures 1.1, 1.2, and 1.6, along with Figure 1.5, which depicts the failure of the right bank of the Naruse River, give a better understanding of the agreement between the simulated failure mechanism and the observed results. It is worth mentioning that without a doubt, the continuous mediums and finite element method cannot show a separation or a rupture between the elements, but the strain localizations help us gain an understanding of what happens in reality.

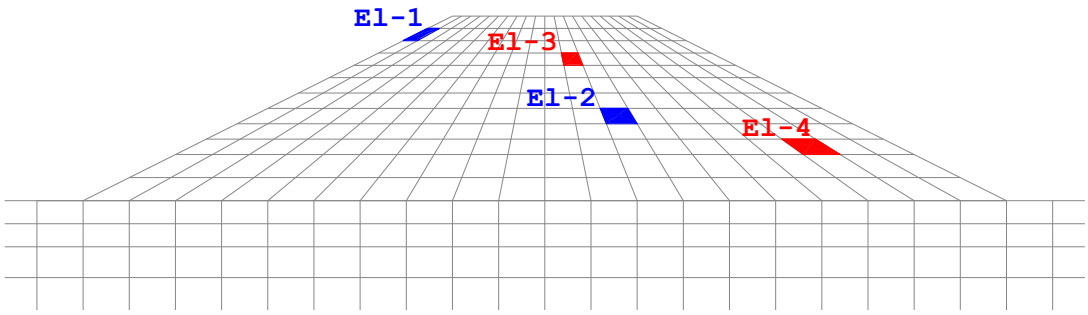

Figure 4.27. Location of reference points for acceleration output

Figure 4.27 illustrates the locations of the reference elements for the strain outputs while Figures 4.28 and 4.29 show the time profiles of the Accumulated plastic shear strain and the accumulated volumetric strain in the selected elements of the embankment, respectively.

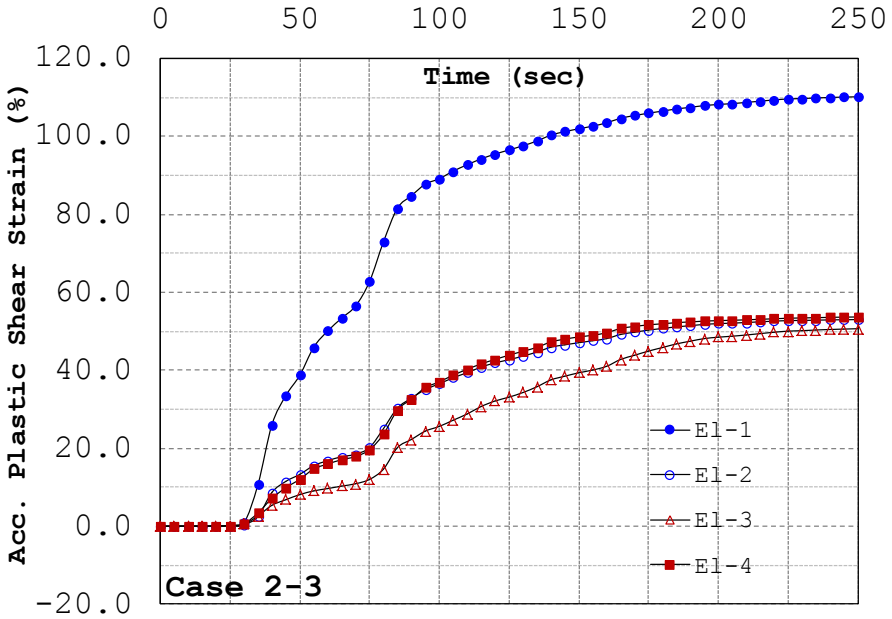

Figure 4.28. Time profile of accumulated plastic shear strain in the selected elements

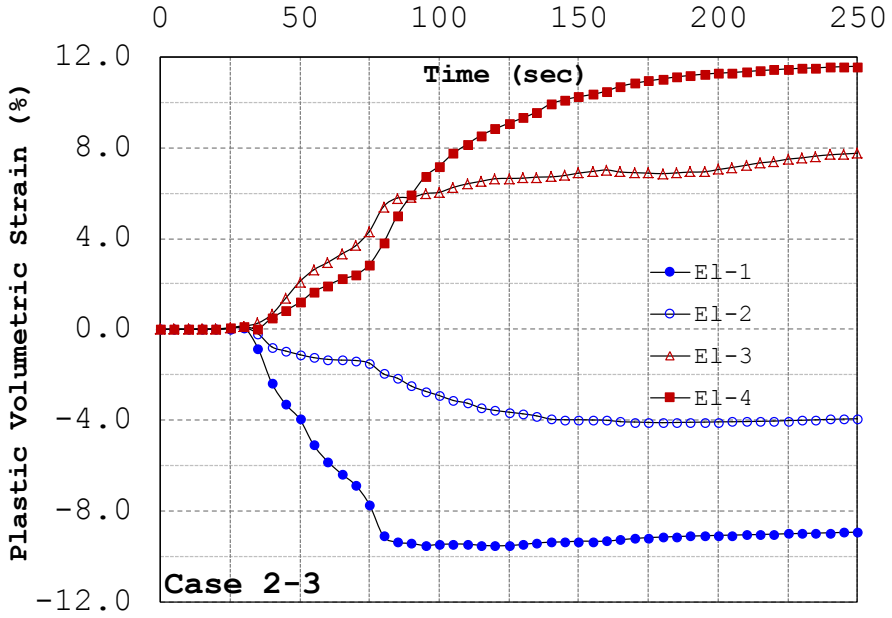

Figure 4.29. Time profile of plastic volumetric strain in the selected elements

**

Positive Values (Red): Contraction
Negative Values (Blue): Dilation

4.3.4. Acceleration Responses

Figure 4.30 illustrates the locations of the three reference points for the acceleration outputs in the model.

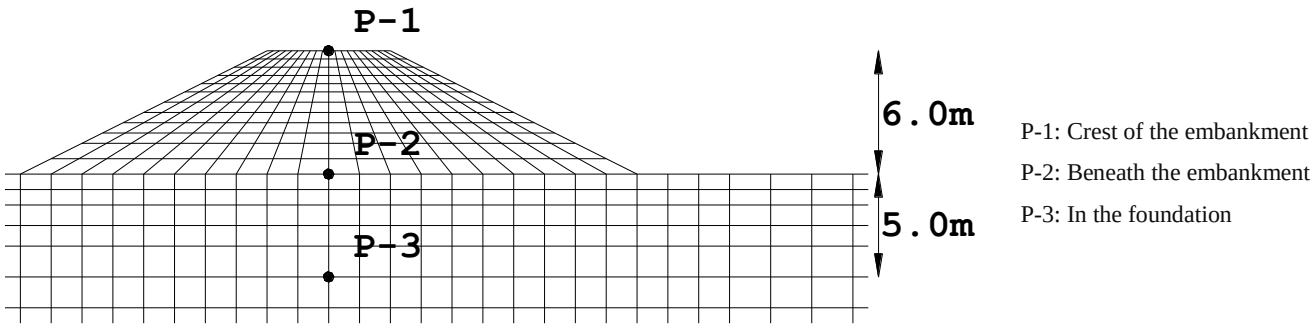

Figure 4.30. Location of reference points for acceleration output

Also shown in Figures 4.31~4.36 are the outputs for all the eight cases. What can be obviously seen in all cases is the amplification of the input acceleration due to the ground profile. While the 1995 Kobe Earthquake had a maximum acceleration of 446 gal, the acceleration response reached more than 1100 gal on the crest. As for the 2011 Tohoku Earthquake, whose peak acceleration was 155 gal, a maximum response of more than three times can be seen at the crest for Case 2-1 in Figure 4.31.

Case 1-1 shows a smooth amplification in the acceleration responses from bottom to top. Since no liquefaction occurs in this case, no significant damping effect can be seen. This is the same behavior as that of Case 2-1. As in the other cases subjected to the 1995 Kobe Earthquake, since there is no significant liquefaction beneath the embankment, the same trend is seen. However, the effect of a soft ground profile can be observed between the acceleration responses of Points 1and 2 in all of these cases.

Case 2-2 clearly shows the effect of liquefaction past the second peak at around 83 sec. Case 2-3, in which both the foundation and the embankment body are liquefied, also shows a clear damping effect of the liquefaction zone on the output acceleration of the crest. The effect is more severe in Case 2-4 in which a thick layer of sand is liquefied.

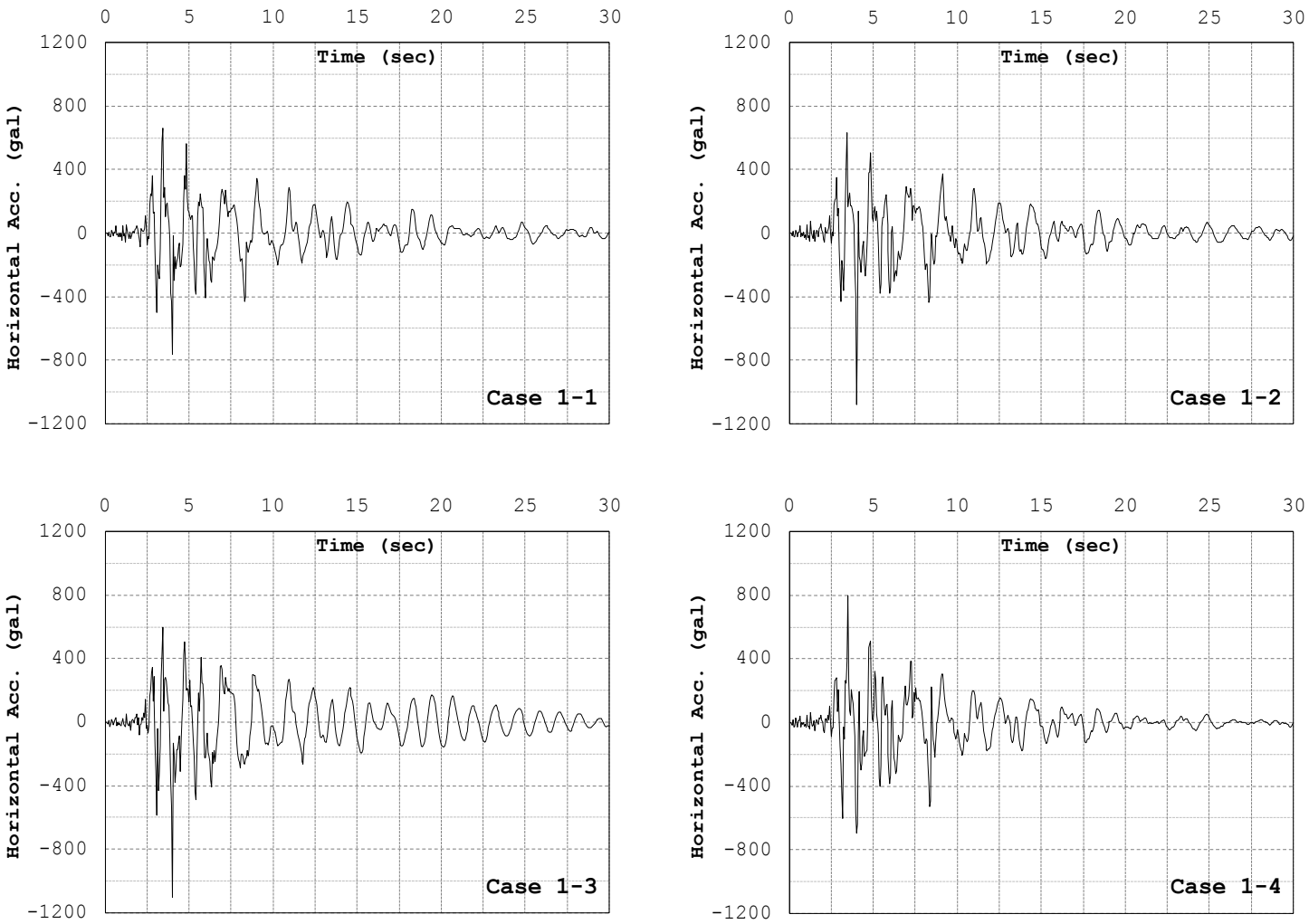

Figure 4.31. Response accelerations of P-1 at the crest of the embankment (Cases 1-1~1-4)

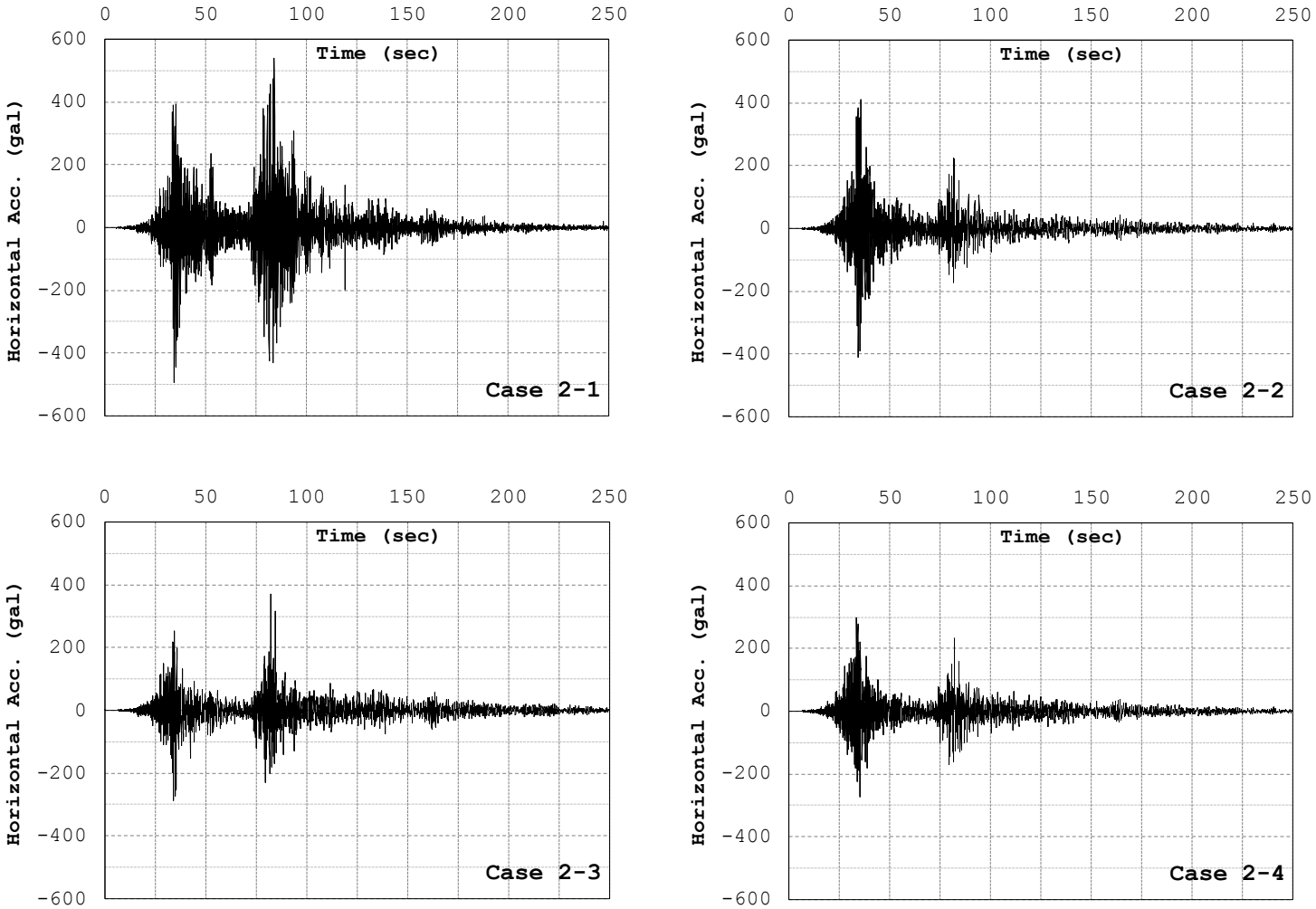

Figure 4.32. Response accelerations of P-1 at the crest of the embankment (Cases 2-1~2-4)

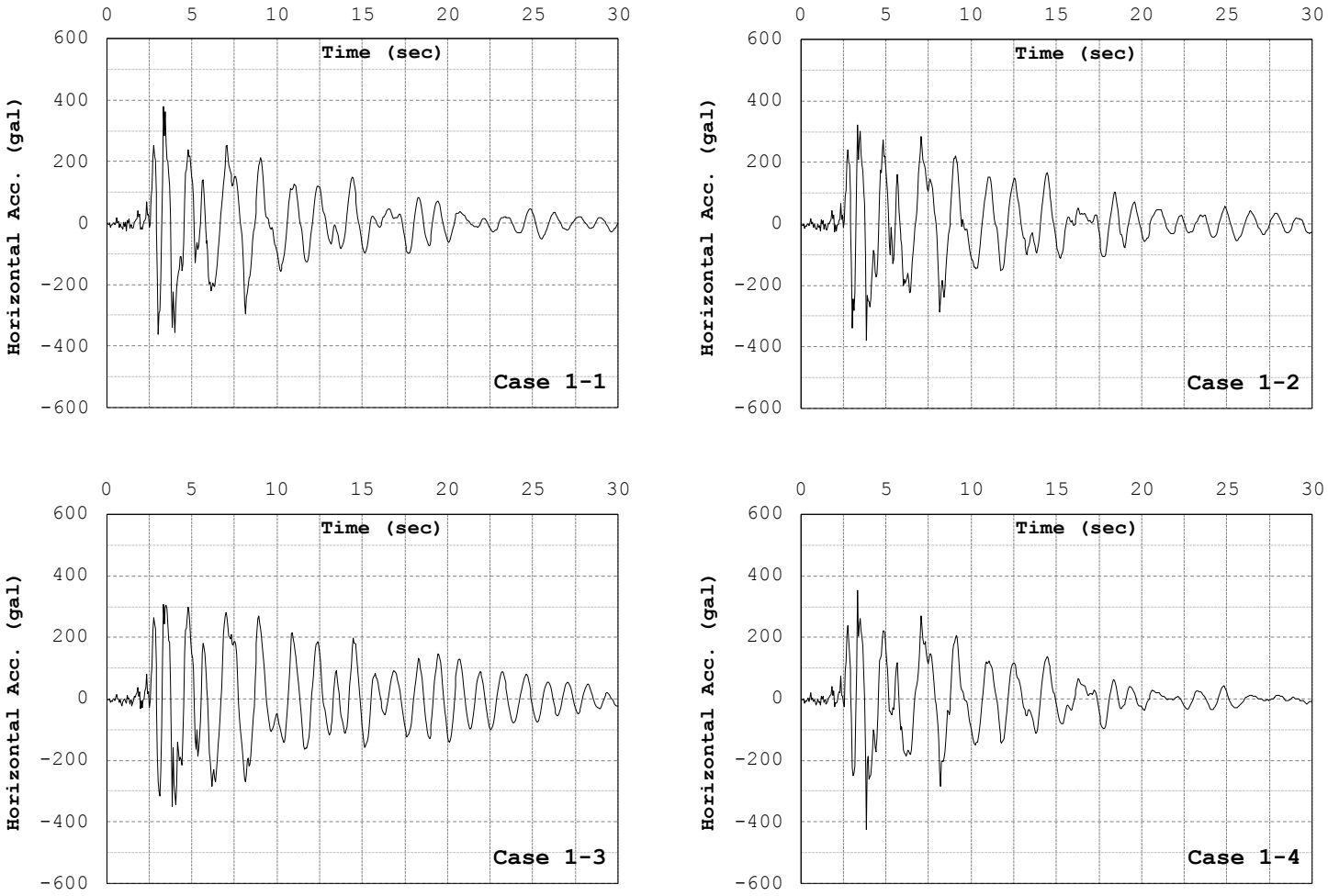

Figure 4.33. Response accelerations of P-2 beneath the embankment (Cases 1-1~1-4)

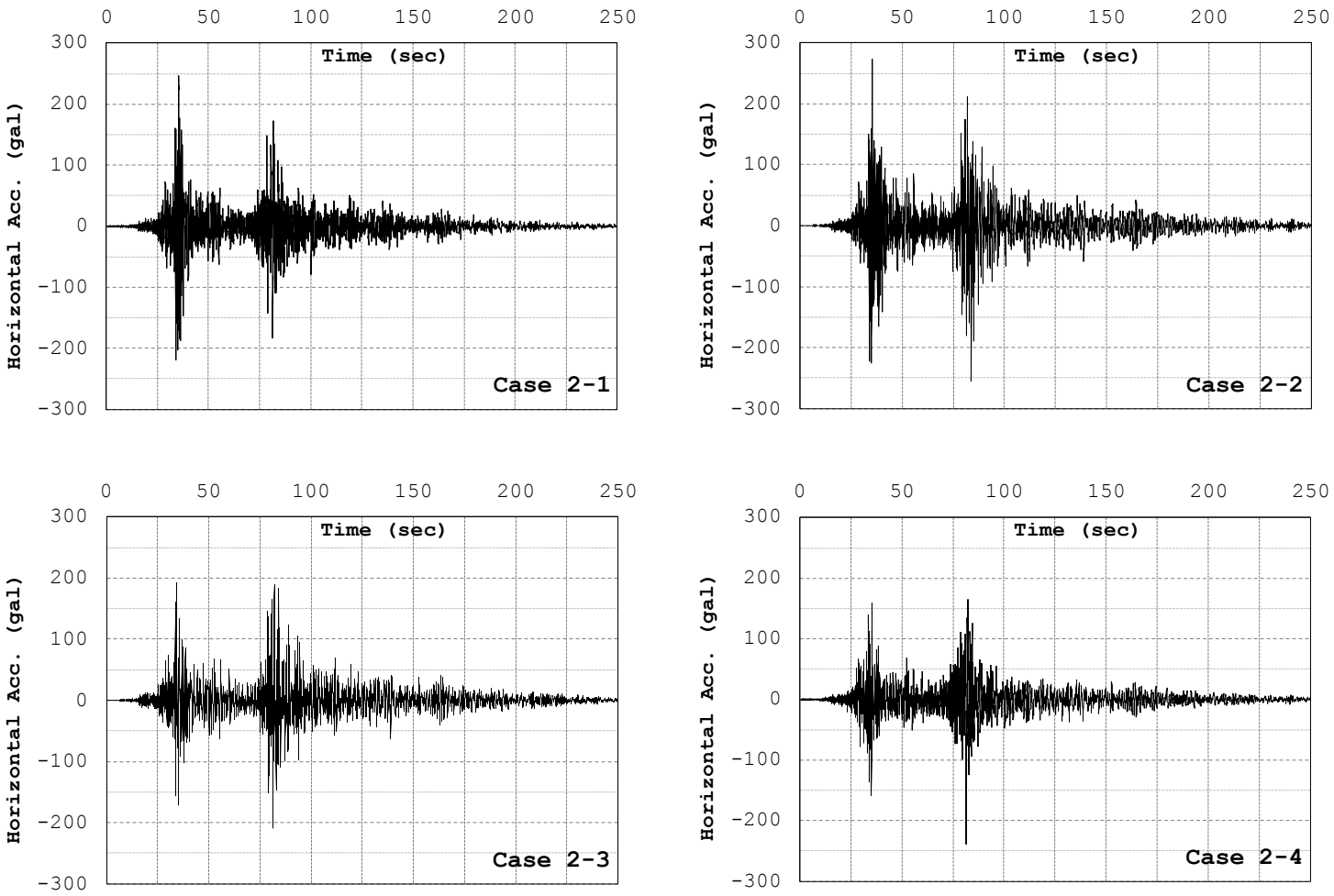

Figure 4.34. Response accelerations of P-2 beneath the embankment (Cases 2-1~2-4)

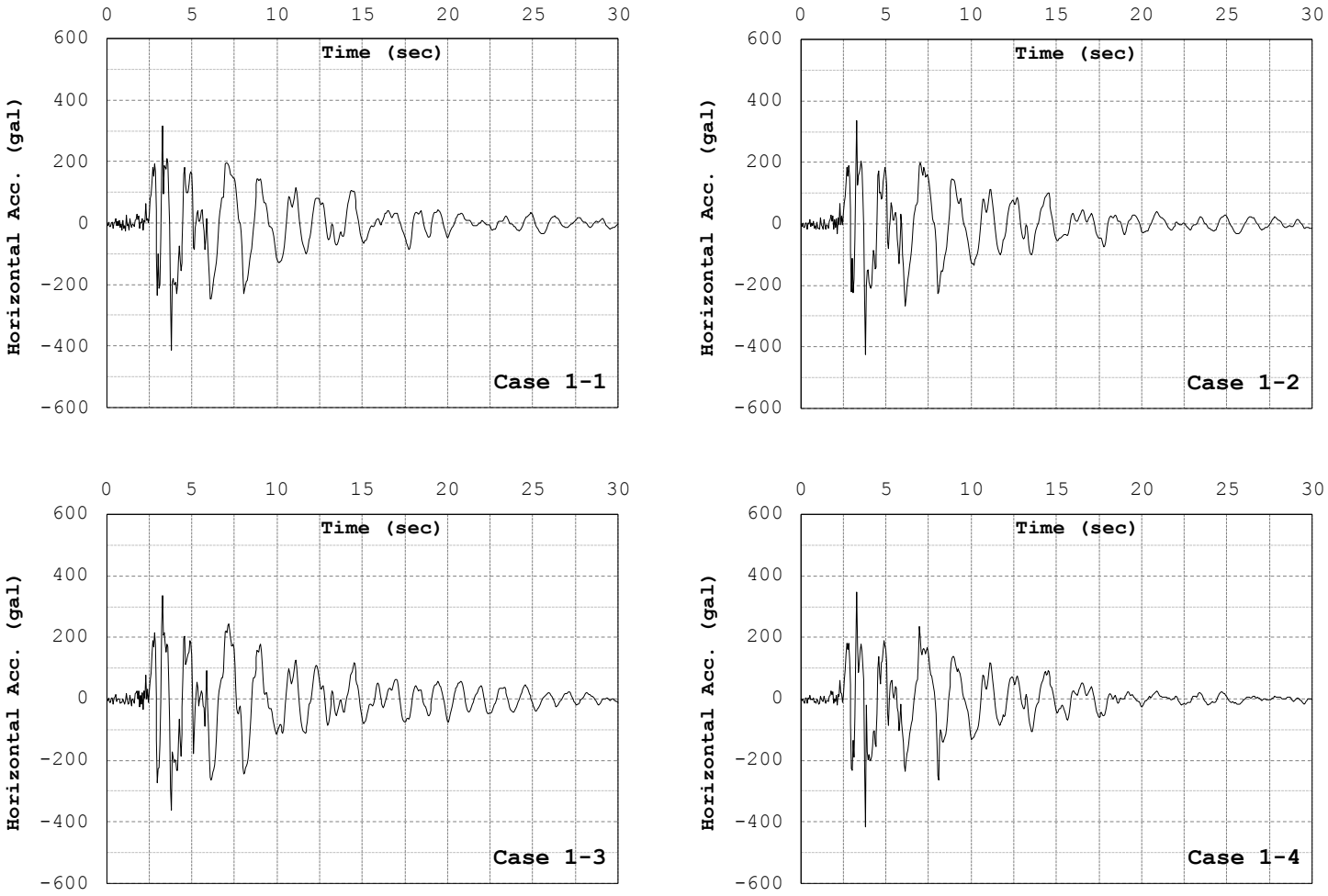

Figure 4.35. Response accelerations of P-3 in the middle of the foundation (Cases 1-1~1-4)

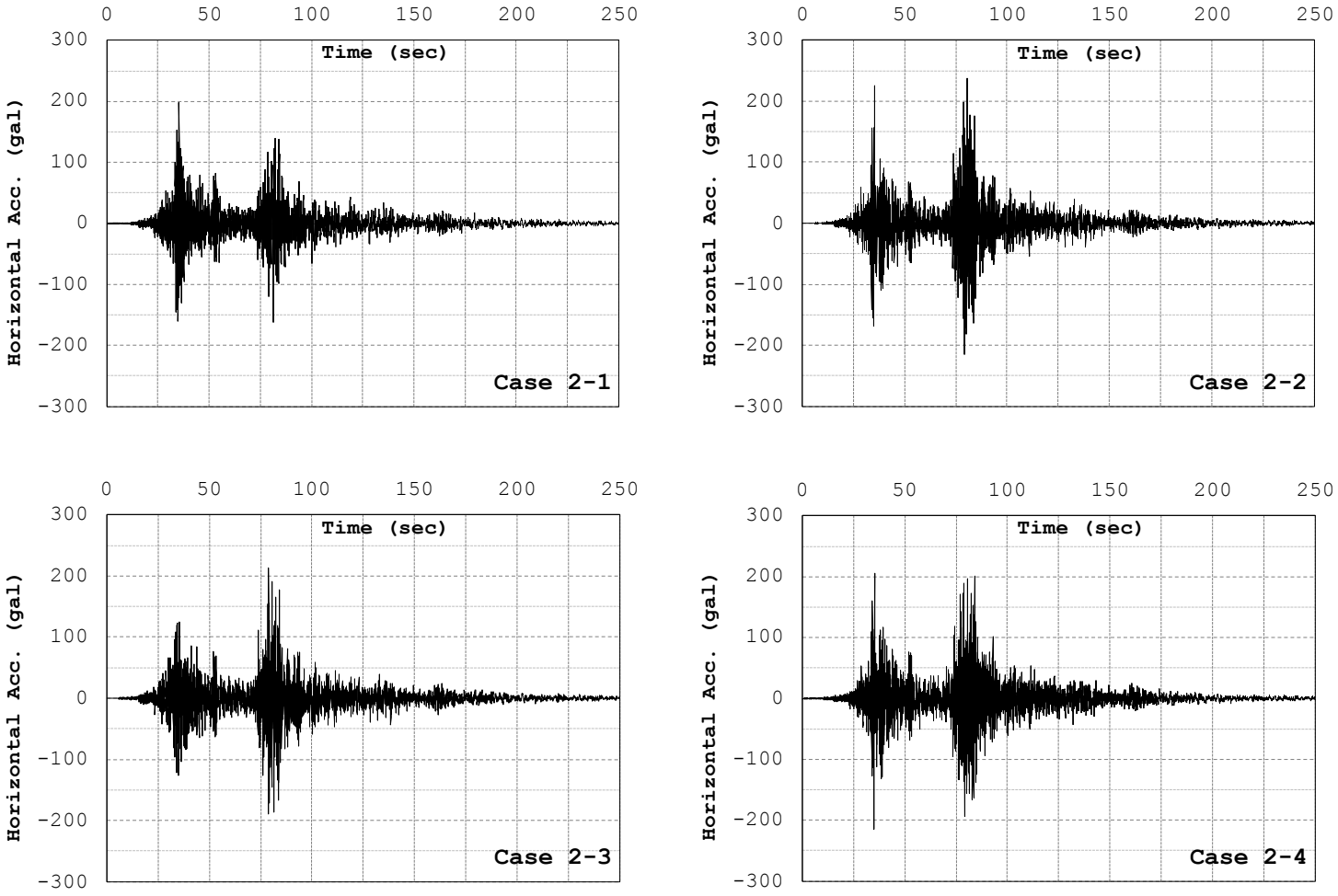

Figure 4.36. Response accelerations of P-3 in the middle of the foundation (Cases 2-1~2-4)

4.4. Summary

Eight cases of different ground profiles were subjected to two input accelerations of different natures and durations, and the following results were obtained:

- Four different types of ground profiles were subjected to two input accelerations of different natures and durations. Dynamic finite element analyses were performed using an elasto-viscoplastic model for clay and an elasto-plastic model for sand in the context of finite deformation. The model parameters for sand belong to sand with a relatively large fines content. The parameters for clay were determined based on the viscoplastic parameters for Torishima clay, Osaka, considering the initial strain rate difference between the laboratory and the field. The FEM model used in this analysis consisted of 880 eight-node isoparametric plane strain elements and the adoption of equal displacement between nodes at both side elements for lateral boundary conditions.
- Records for the 1995 Kobe Earthquake, with a depth of 33 m at the Higashi-Kobe Bridge, and the 2011 Tohoku Earthquake, recorded with MYGH06 at a depth of 80 m at Tajiri by KiK-net, were used as the input motions. The dominant period of the 2011 off the Pacific Coast of Tohoku Earthquake was smaller than that of the 1995 Kobe Earthquake. The duration time of the 2011 Tohoku Earthquake (Input 2) was longer than that of the 1995 Kobe Earthquake (Input 1), although its maximum acceleration was smaller than that of the 1995 Kobe Earthquake.
- Four types of ground profiles, including soft clay in the foundation, were used. In the Type 1 ground, the embankment made of sandy soil was lying on a saturated clay layer. The Type 2 ground corresponds to the case in which the embankment has settled into the clayey foundation and the bottom is below the water table. In the Type 3 ground, the river embankment has settled into the soft foundation, while the water table existed inside the embankment body. Finally, Type 4 is an embankment on a saturated sandy layer lying on a clay layer.
- In Case 1-1, subjected to the 1995 Kobe Earthquake, settlement, lateral spreading, and heaving around the toe is larger than the response of Case 2-1 which was subjected to the 2011 Tohoku Earthquake. The embankments in both cases (especially Case 2-1) are little damaged. Case 1-2 exhibits a small amount of settlement and damage, while Case 2-2, in which the foundation is liquefied, has a large settlement, lateral movement, and heaving with a vertical localized zone in the body. In Case 1-3, although no extensive liquefaction can be seen in the foundation, a deep sliding type of localization and the lateral spreading can be seen. However, Case 2-3, in which

part of embankment body and foundation are liquefied, manifests the largest settlement with vertical localized deformation. This case presents heavy damage. In Case 1-4, a uniform slump into the liquefied sandy bed is seen. However, in the response of Case 2-4, we can see lateral flow on the liquefied foundation with deep vertical or inclined localization toward the center.

- In all cases, the soft clay foundation causes an amplification effect. In addition, the liquefied foundation plays a major role in the damping of the input acceleration. The interesting point is that the deformation of the clay foundation due to the 2011 Tohoku Earthquake is small in all cases.
- The analysis results for the Type 3 ground profile, which has been reported to be the weakest against liquefaction during the 2011 Tohoku Earthquake, show the most severe damage due to the long duration of the earthquake motion. The numerical results indicate that in the ground with a liquefiable foundation, the simple circular sliding type of failure mode that is assumed in common geotechnical engineering practice is not to be expected.

Chapter 5

Comparison between the Results by Finite Deformation and Infinitesimal Methods in the Dynamic Behavior of River Embankments

5.1. Introduction

This chapter provides a comparison between the results by the finite deformation and the infinitesimal analysis methods for the dynamic analysis of embankments considering liquefaction. Due to its easier formulation, the current engineering practice and most numerical researches use the infinitesimal strain analysis method. Since earthquake-induced liquefaction causes large deformations, it is of great importance to pay attention to the differences between the finite deformation and the infinitesimal methods and to know their limitations. When using an infinitesimal formulation, the entanglement of the finite element mesh is encountered, and this will bring about low accuracy in the case of large deformations. This comes from the fact that the infinitesimal formulation adopts no changes in the integration points of the finite element mesh. To overcome this issue, several large-strain analysis methods or so-called finite deformation methods, i.e., the updated Lagragian method, have been developed by Tomita (1994), Belytchko et al. (2000), etc. In the infinitesimal scheme, the difference between the current and the reference configurations is not recognized, and the updated Lagrangian scheme renews the reference configurations like the finite element mesh at every step of the calculation.

It is not known whether or not the updated Lagrangian scheme is absolutely perfect, but this method definitely performs better in terms of accuracy, except for problems with very high rates of loading. It is worth noting that for very high rates of loading, the updated Lagrangian scheme may cause instability. This is because the response may be sensitive to the significant renewal of the mesh depending on the time increment of the analysis.

Oka & Kodaka et al. (2001) applied a numerical formulation to the analysis of a quay wall damaged by the 1995 Hyogoken Nanbu Earthquake and showed the effectiveness of the finite deformation method in the liquefaction analysis. Oka et al. (1992) and other researchers, such as Finn et al. (1991), Oka et al. (2006), Borja et al. (2002), Matsuo et al. (2000), Uzuoka et al. (2011), and Chiaro et al. (2012), investigated different features of finite deformation considering liquefaction. Nevertheless, many aspects of these numerical analysis methods are still unknown.

In this chapter, we present a comparison between the results of the finite deformation (FD) and the infinitesimal strain (IS) methods in the analysis of river embankments on liquefiable foundations subjected to earthquakes and investigate the different aspects of failure modes and deformations by the two methods.

5.2. Numerical Model

5.2.1. Soil Profile

The model used in the present study is for a sandy embankment on a clayey foundation. As seen in Figure 5.1., due to the consolidation or the compressibility of the ground, the bottom of the embankment has settled into the soft foundation and has become saturated (Case 2 in the previous chapter). The water table is at the ground level.

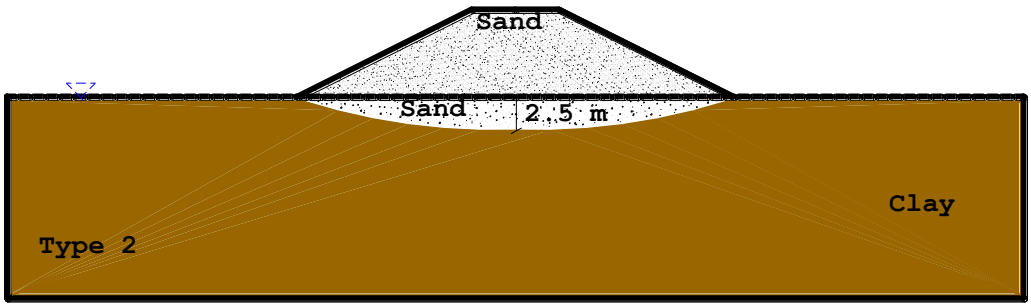

Figure 5.1. Soil profile and water table

5.2.2. Input Accelerations

The 2011 off the Pacific Coast of Tohoku Earthquake, observed at Tajiri recorded at the depth of -88.0m, was used as an input wave because of its main characteristic of long duration, as seen in Figure 5.2. In addition, the Tajiri area is close to the location of the levees damaged by the 2011 Tohoku Earthquake. This earthquake caused widespread damage to infrastructures, i.e. river embankments.

Input 2 – 2011 off the Pacific Coast of Tohoku at Tajiri MYGH06-NS Component (KIK-net)

Max: 155.2 gal

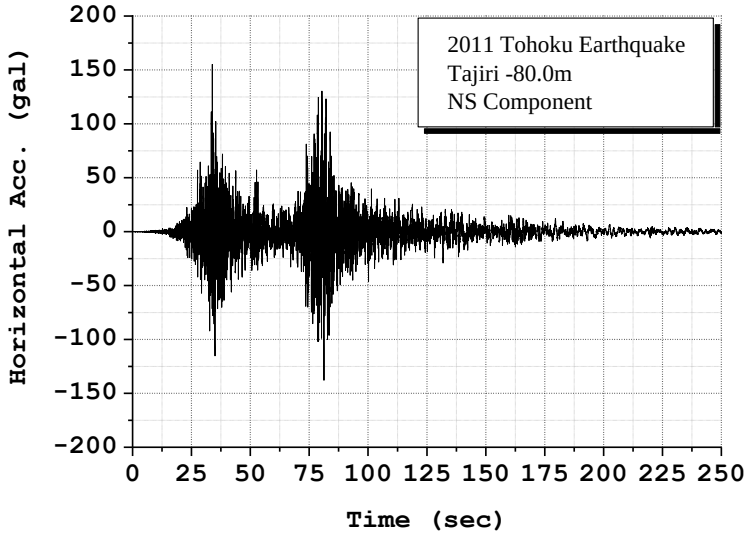

Figure 5.2. Input acceleration used for the analysis

5.2.3. FEM Model

The FEM model used in the analysis consists of 880 elements for both infinitesimal strain (IS) and finite deformation (FD) analyses. 4-node plane strain and 8-node isoparametric plane strain elements were used for the IS and FD analyses, respectively. Equal displacement lateral boundary conditions were adopted for the side elements. Figure 5.3 shows the left half of the model. In addition, Figure 5.4 shows the two types of elements used in this simulation. The IS analysis was performed using the LIQCA2D11 code by the LIQCA Research and Development Group, while the FD simulation was conducted using the program COMVI2D-DY013 developed by Oka et al. (2013).

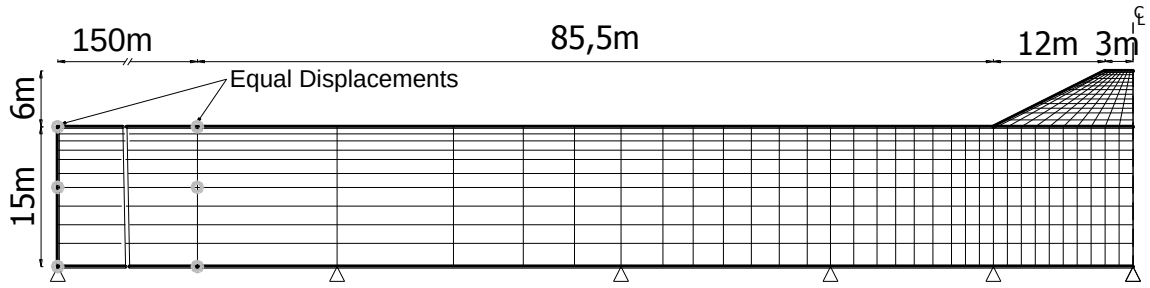

Figure 5.3. Finite element mesh and boundary conditions

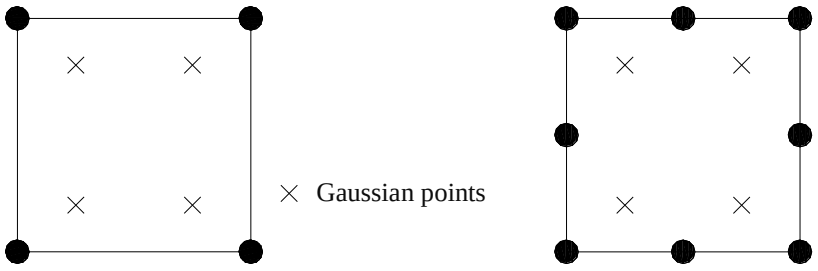

Figure 5.4. Different elements used in the analysis

5.2.4. Material Properties

Table 5.1 shows the material parameters used in the analyses. An elasto-viscoplastic material has been used for the clayey layer, while an elasto-plastic model has been used for the sandy layer as well as for the embankment.

Table 5.1. Material Parameters of Akita Sand and Torishima Clay

	Elasto-plastic Sand	Elasto-viscoplastic Clay
Density $\rho(t/m^3)$	1.8/2.0	1.66
Water specific weight γ_w (kn/m^3)	9.81	9.81
Coefficient of permeability K_{ws} (m/s)	2.25×10^{-4}	5.87×10^{-10}
Initial void ratio e_0	0.8	1.25
Compression index λ	0.025	0.341
Swelling index κ	0.0003	0.019
Initial elastic shear modulus ratio G_0/σ'_{m0}	761	400
Stress ratio at critical state (clay)/phase transformation (sand) M^*_m	0.909	1.24
Stress ratio at failure M^*_f	1.229	1.24
Hardening parameters B^*_0, B^*_1, C_f	5000,300,1000	500,100,5
Structural parameters n,β	0.50,50	0.30,3.6
Dilatancy parameters D^*_0,n	1.0,4.0	
Reference value of plastic strain γ_r^{p*}	0.0050	
Reference value of plastic strain γ_r^{e*}	0.003	
Viscoplastic parameter m'		24.68
Viscoplastic parameter C_1(1/s)		1.00×10^{-11}
Viscoplastic parameter C_2(1/s)		3.83×10^{-12}
Scalar hardening parameters A^*_2, B^*_2		5.9,1.8
Strain-dependent parameters α',r		10,0.4

5.3. Results

5.3.1. Effective Stress Decreasing Ratio

Both models were subjected to the 2011 Tohoku Earthquake, which was 250 seconds long. Figures 5.5 and 5.6 show the distributions of the effective stress decreasing ratio. It is clearly seen that in the FD model, liquefaction occurs earlier and causes a widespread flow in the foundation. However, the results show that the settlement of the embankment in the IS analysis is larger than that in the FD analysis. As shown in these figures, liquefaction in the foundation occurs beneath the toe of the embankment in the FD model, while liquefaction occurs locally in the center of the foundation in the calculation by the IS model. As suggested in previous researches, the development of excess pore-water pressure and liquefaction occurs sooner in the IS simulation. It can be clearly seen that just after the first shock of the earthquake, around 35 seconds, the IS model produces liquefaction earlier than the FD model.

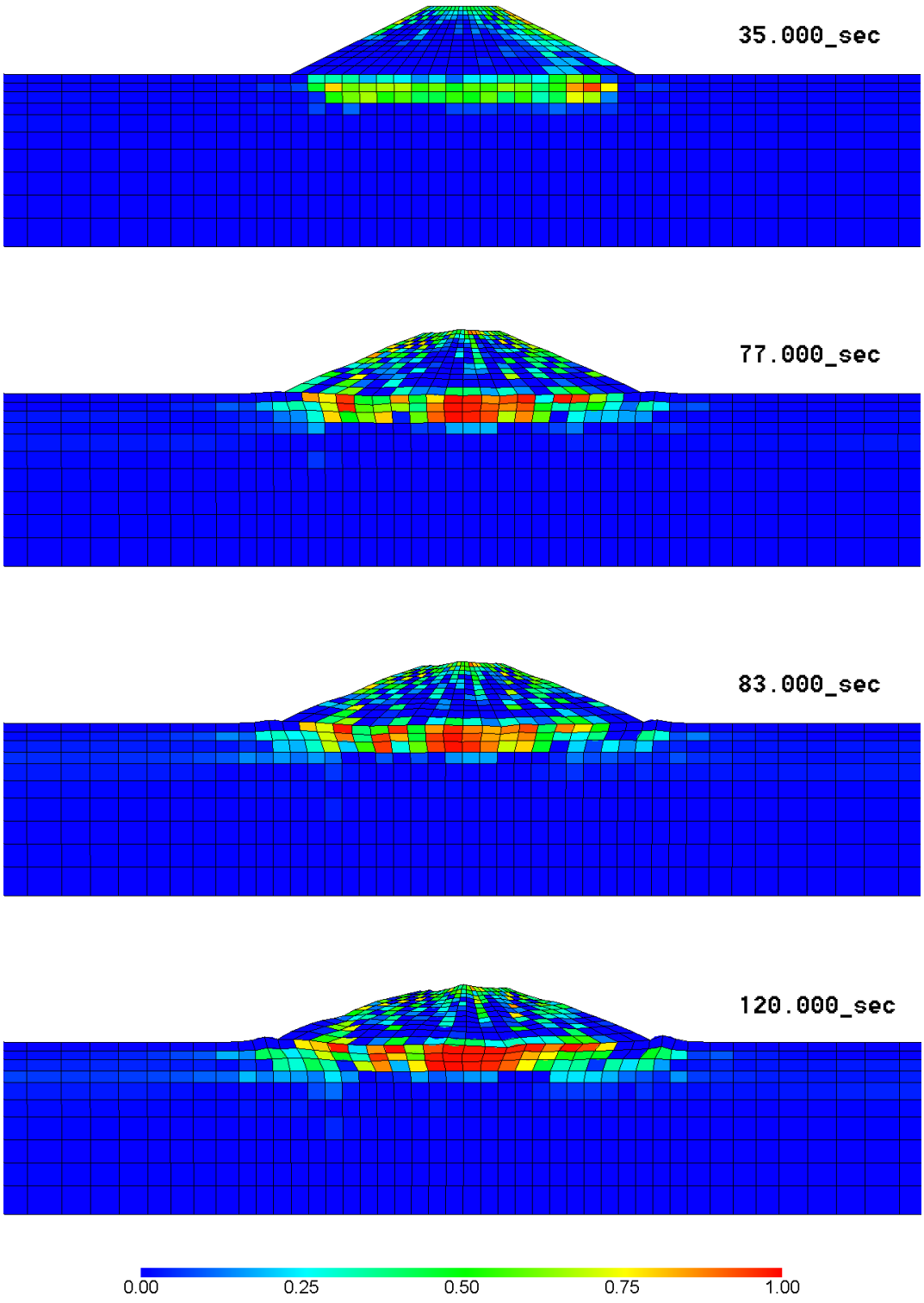

Figure 5.5. Distribution of effective stress decreasing ratio (FD analysis)

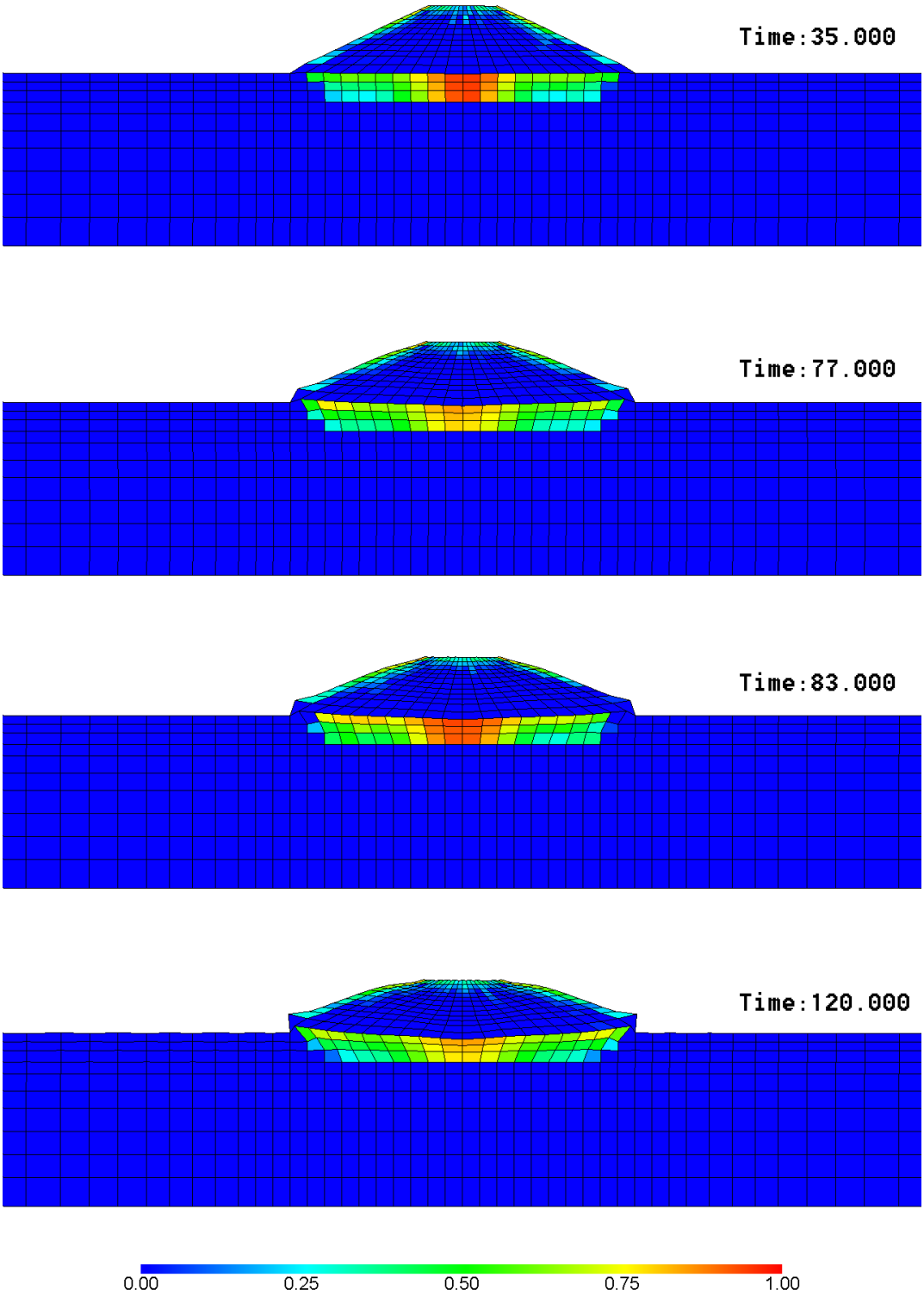

Figure 5.6. Distribution of effective stress decreasing ratio (IS analysis)

5.3.2. Displacements

Figures 5.7 and 5.8 illustrate the deformation-time profiles of the crest and the toe of the embankment, respectively. As previously mentioned, the IS method undergoes more settlements. However, there is a significant difference in the modes of deformation and failure. While the IS analysis method produces a larger settlement at the crest, the lateral spreading and heaving at the toe produced by the FD method are larger. This can be attributed to the fact that liquefaction occurs extensively toward the bottom of the toe in the simulation by the FD method. However, the deformation at the toe of the embankment in the IS analysis is quite unusual. The IS method shows an obvious start of rapid settlement, since the onset of liquefaction is at around 33 seconds. On the other hand, the rate of settlement is slightly larger by the second shock of the earthquake.

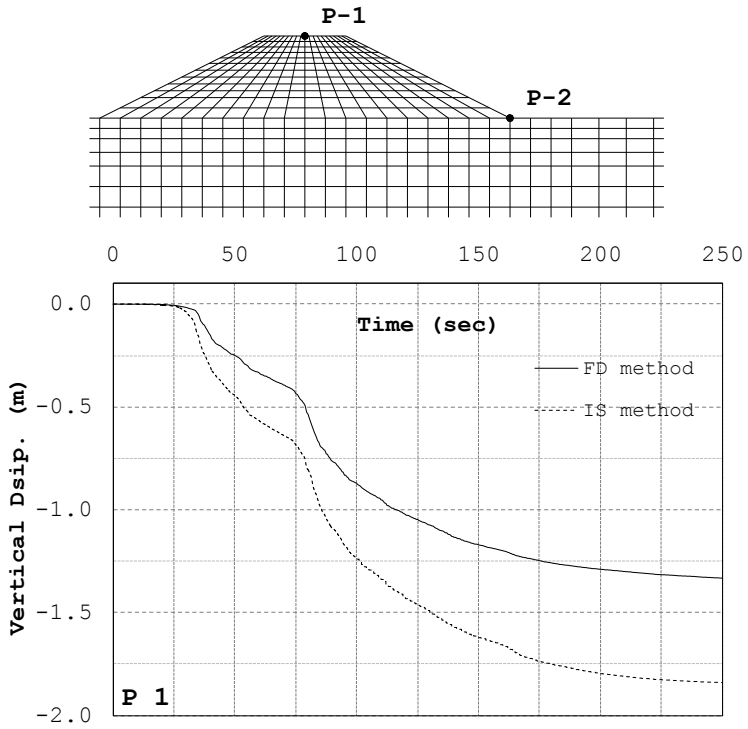

Figure 5.7. Settlement time-profile of embankment crest

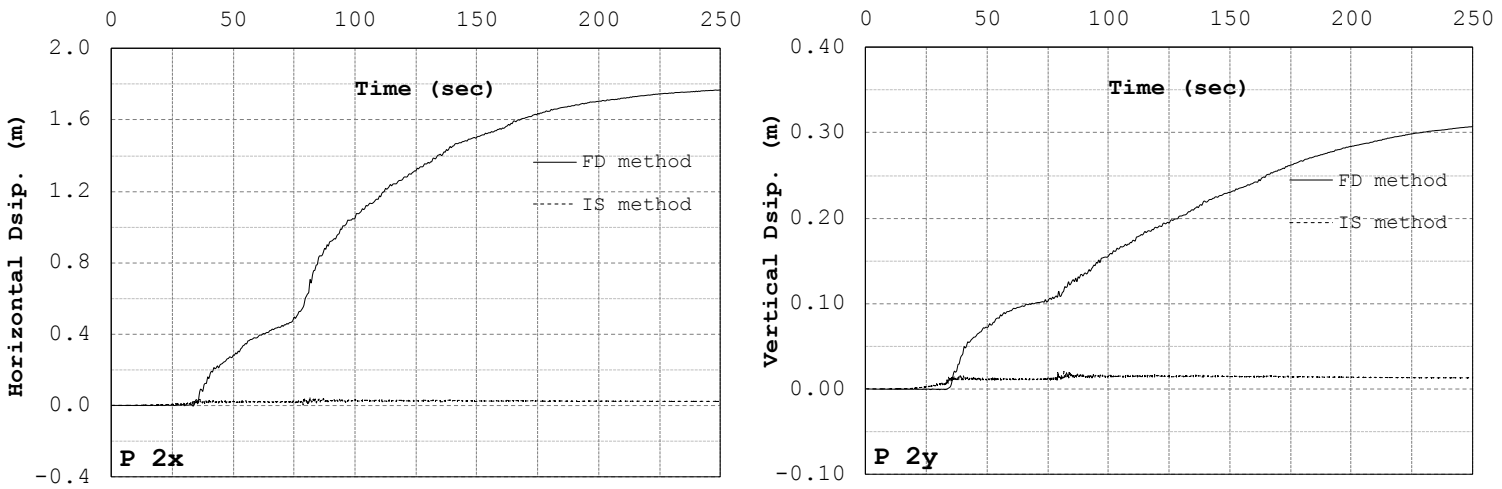

Figure 5.8. Horizontal and vertical displacements of embankment toe

5.3.3. Stress and Pore-Water Pressure Response

Figures 5.9 and 5.10 present the responses in the sandy and clayey layers with the FD and IS methods, respectively. El-1 is located beneath the embankment in the saturated sandy layer below the groundwater level, while El-2 is located in the clayey layer.

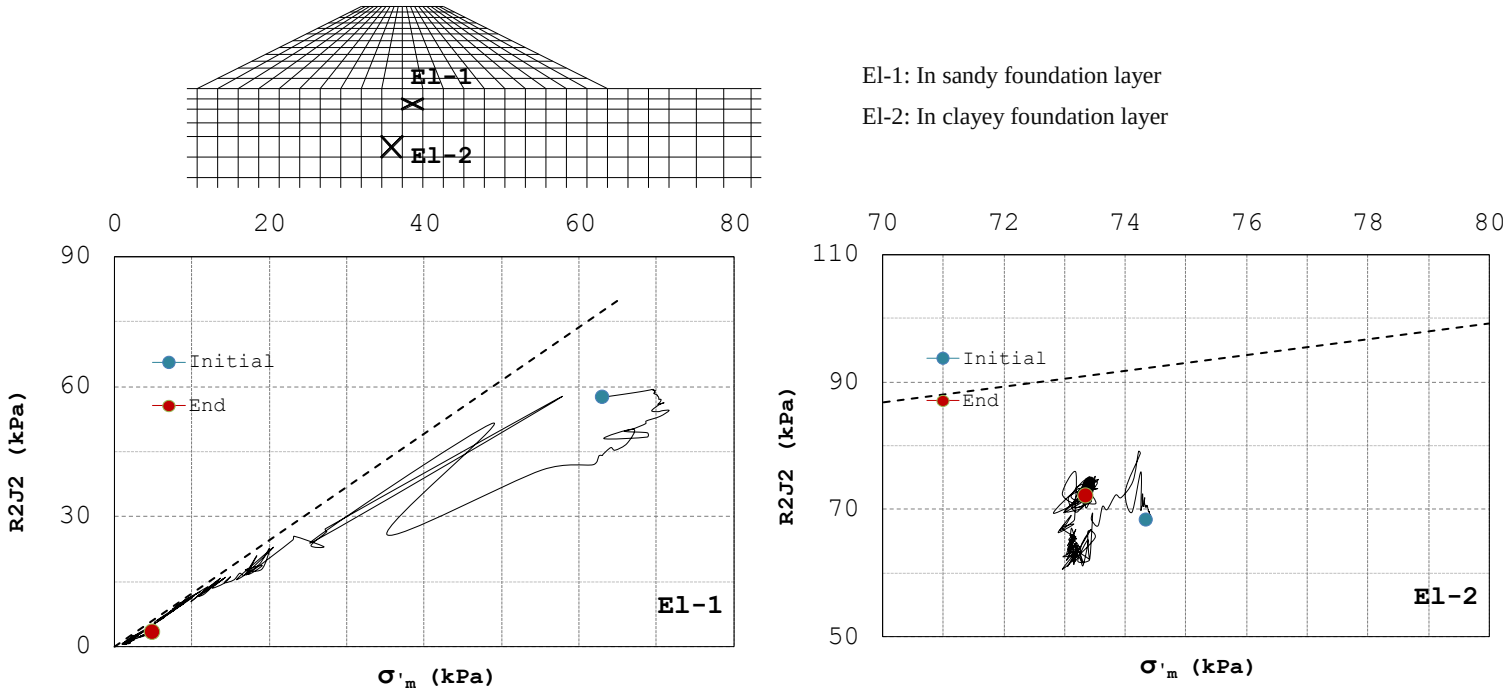

Figure 5.9. Stress path by FD method

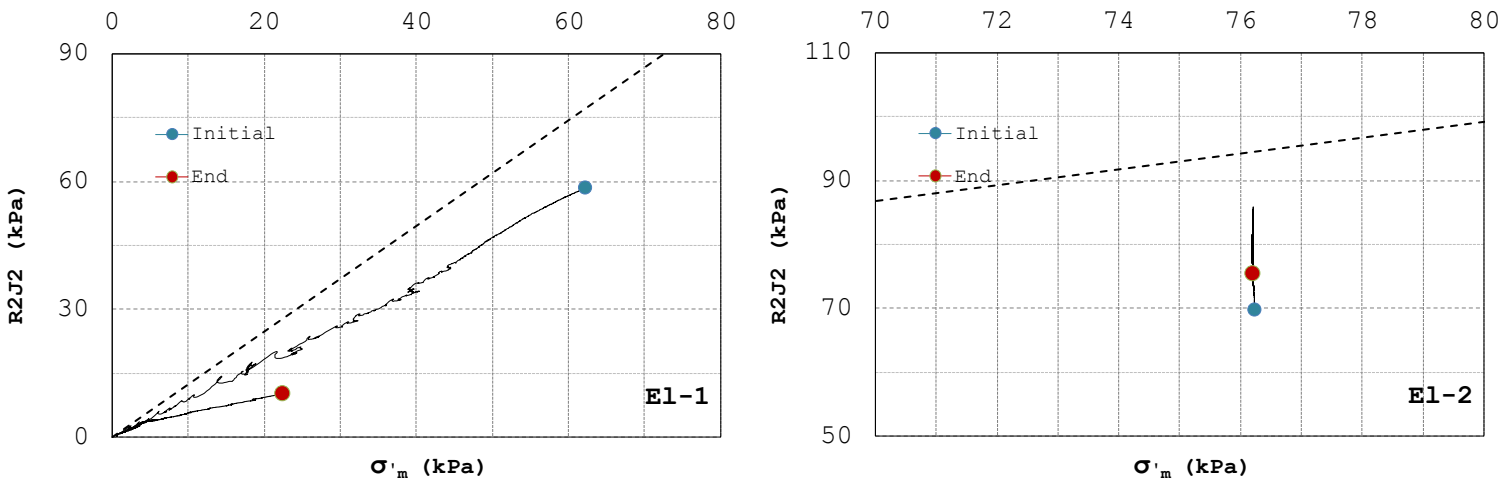

Figure 5.10. Stress path by IS method

As can be seen in Figures 5.9 and 5.10, in element El-1, the mean effective stress of both results reaches zero. On the other hand, element El-2, which is located in the clayey foundation layer, undergoes little damage or deformation. Hence, the mean effective stress does not vary much during the loading cycles.

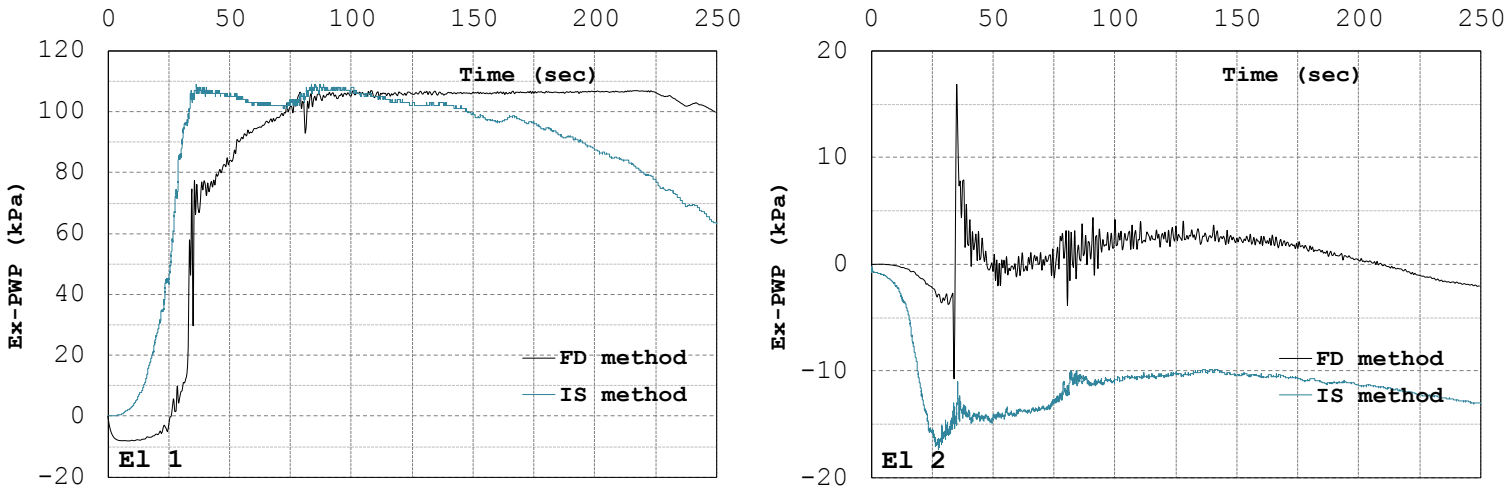

Figure 5.11. Development of excess pore-water pressure

The excess pore-water pressure responses in both elements are similar for both infinitesimal (IS) and finite deformation (FD) analyses, as seen in Figure 5.11. Element El-1, which is in the saturated sandy

layer, experiences rapid growth in excess pore-water pressure in 30 seconds. Although it is faster in excess pore-water pressure growth, the IS analysis shows a quick decline after 120 seconds.

Element El-2, which is less affected by the earthquake, shows a reduction in excess pore-water pressure before the first earthquake shock (33 seconds) and then continues with the increase in excess pore-water pressure afterwards. It is clear, however, that the development of pore pressure in the simulation by the IS method is faster and stronger.

Figure 5.12 shows the variations in the effective stress decreasing ratio ($ESDR = 1 - \sigma_m^{'} / \sigma_{m0}^{'}$, $\sigma_{m0}^{'}$: *initial mean effectivestress*) in the sand element.

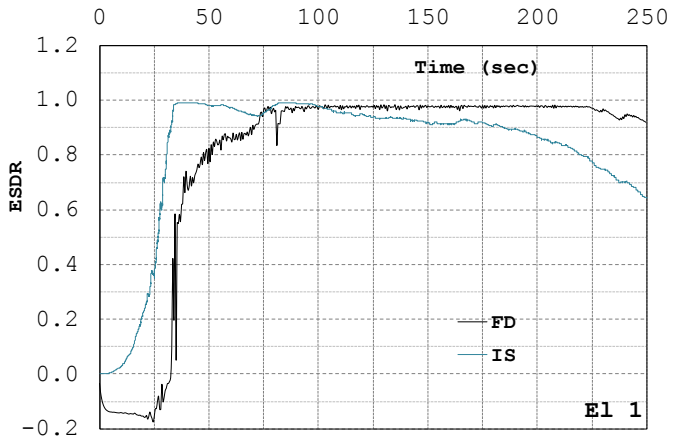

Figure 5.12. Effective stress decreasing ratio in Element 1 of the saturated sandy layer

In harmony with the development of excess pore-water pressure, Element El-1 in the IS simulation element reaches liquefaction faster. In the simulation by the IS method, the element reaches liquefaction around the first shock of the earthquake, but Element El-1 by the FD model does not completely liquefy until a few steps before the second main shock of the earthquake wave. It is apparent that in the simulation by the IS method, the excess pore-water pressure is reduced by the expansion of the soil and the ESDR reaches 65% by the end of the earthquake shocks.

5.3.4. Accumulated Plastic Shear Strain

The distributions of accumulated plastic shear strain $\gamma^p = \int \left(de_{ij}^p de_{ij}^p \right)^{1/2}$ for simulation results at both 83 and 250 seconds are presented in Figures 5.13 and 5.14, respectively. It is seen that the deformation patterns and the strain localizations are different in the two simulations.

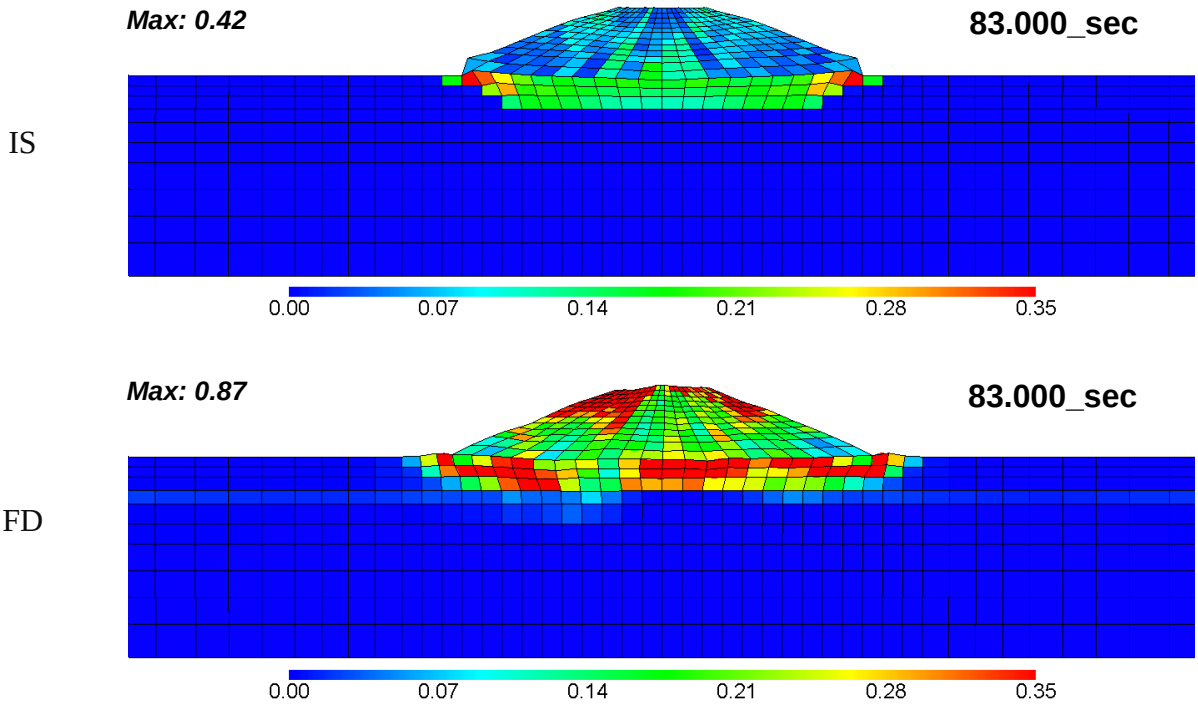

Figure 5.13. Distributions of accumulated plastic shear strains after 83.0 seconds

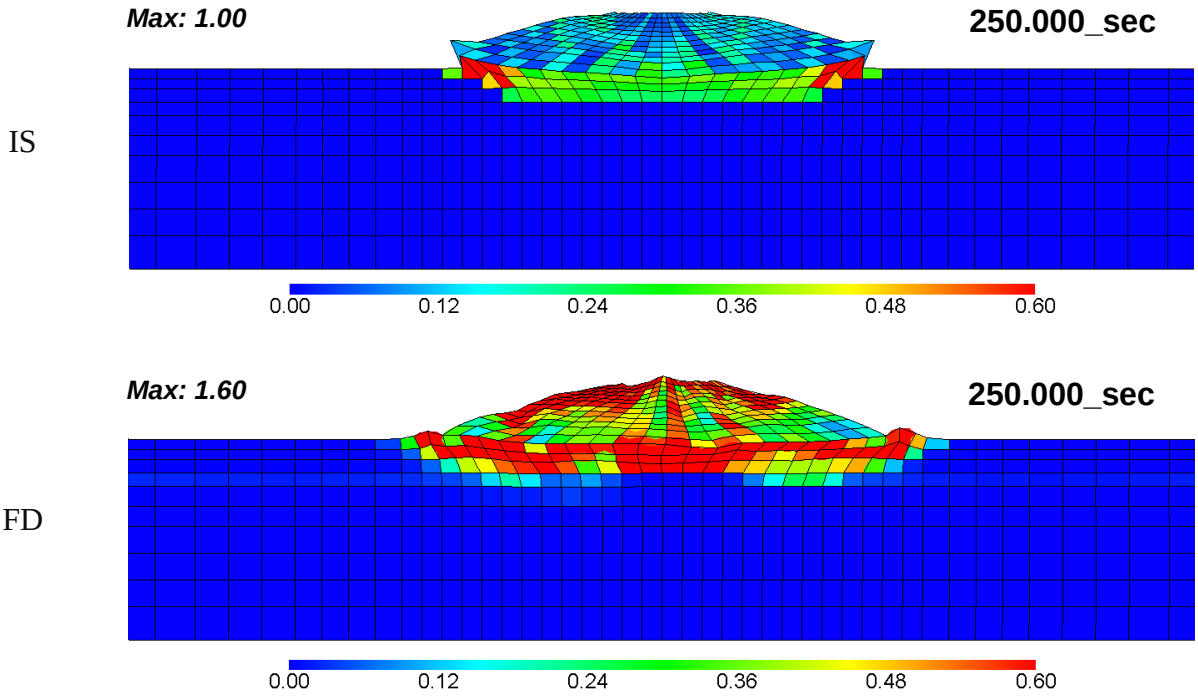

Figure 5.14. Distributions of the accumulated plastic shear strains after 250.0 seconds

While a subsidence is seen at the center of the embankment in the simulation by the IS method, the crest of the embankment in the analysis by the FD method subsides unequally. This appears to lead to vertical cracks. Moreover, the maximum localization of strain in the FD analysis occurs between the shoulder and the center of the embankment. By the IS analysis method, however, the strain is severely localized beneath the toe of the embankment. In the simulation by the FD method, the liquefaction just below the embankment (in the saturated sandy layer) causes the spreading of the embankment body to both right- and left-hand sides.

5.3.5. Acceleration Responses

Figure 5.15 shows the location of reference points for discussing the acceleration response. Point P-1 is on the embankment crest, Point P-2 is the point just beneath the embankment center, and Point P-3 is the point in the clay foundation.

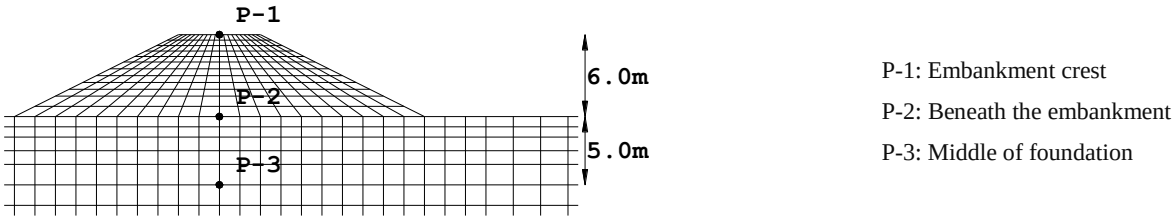

Figure 5.15. Location of reference points for acceleration response

In addition, the acceleration responses for the simulations by both methods are shown in Figures 5.16 and 5.17. It is clearly seen that the amount of acceleration response for the FD analysis is larger than that for the IS analysis at almost all points in time. However, the relatively soft clay shows the damping effect in both simulations. It can be easily seen that the accelerations decrease from P-3 to P-1. Moreover, the responses of the crests of the embankment exhibit smaller shocks due to the liquefaction of the foundation.

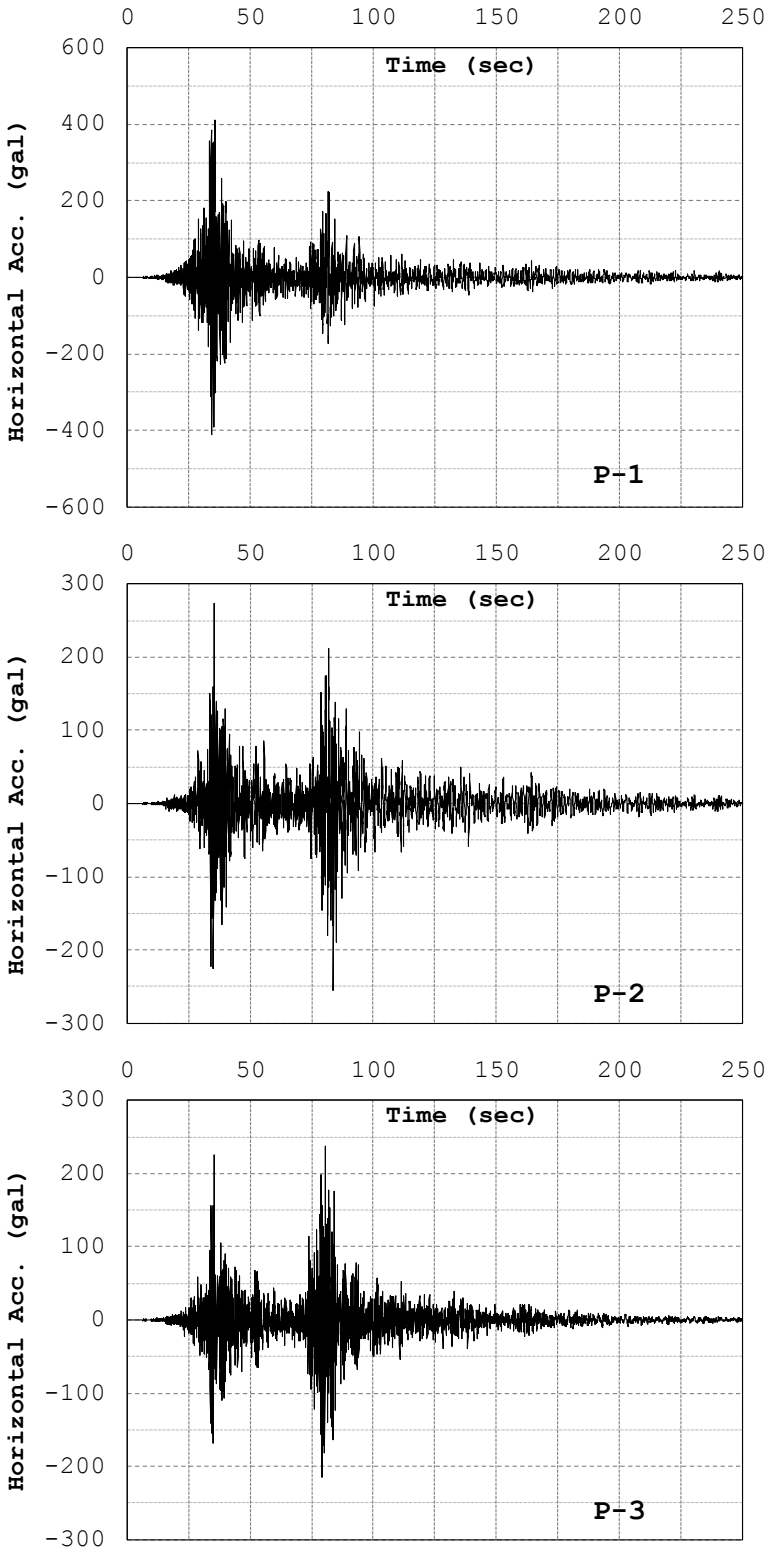

Figure 5.16. Response accelerations (FD analysis method)

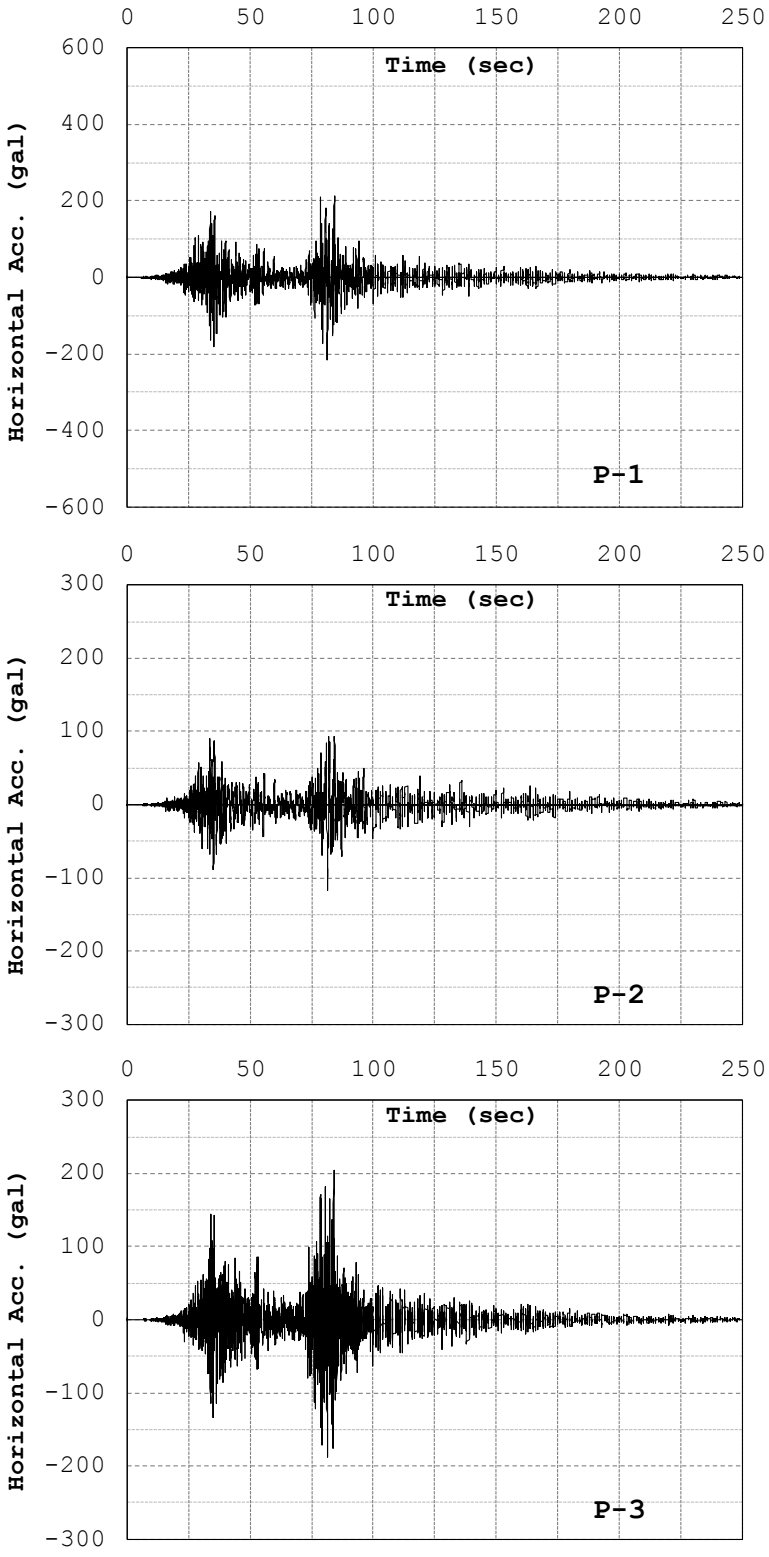

Figure 5.17. Response accelerations (IS analysis method)

5.4. Summary

- In the infinitesimal strain (IS) analysis method, it was seen that the excess pore-water pressure developed earlier in both the sandy and the clayey layers. However, the dissipation of pore-water pressure was stronger. The fast dissipation occurred specifically in the post-peak of the earthquakes.
- The settlements of the embankment calculated by the IS method were larger than those by the finite deformation (FD) analysis method. It was clearly seen that the deformation of the sandy embankment in the analysis by the IS analysis method was larger than that by the FD analysis method.
- The simulated results show that the heaving and the lateral spreading at the toe of the embankment by the FD method were larger than those by the IS analysis method.
- The finite deformation analysis seems to be more stable after liquefaction. In the dissipation of the excess pore-water pressure, depending on the level of permeability, the thickness of the soil layer, the fines content, etc. However, it was clearly seen that the element in the IS simulation dissipated a considerable amount of excess pore-water pressure just after the onset of liquefaction.
- The IS and FD analysis methods yielded differences in terms of the overall deformation-failure mechanisms in the liquefiable embankments. It is clear that the simulated pattern by the FD method for the embankments on liquefiable foundations had a better agreement with the field observations in terms of deformation-failure mechanisms.

Chapter 6

Conclusions

6.1. Summary and Concluding Remarks

In the present study, the dynamic behavior of river embankments subjected to strong earthquakes was studied using a multiphase finite element method based on the finite deformation theory. The main focus was placed on the different possible deformation-failure mechanisms and damage patterns of river embankments due to earthquakes and the liquefaction they induced. Moreover, achieving the complex deformation-failure modes that are not usually considered in geotechnical engineering practice was of great interest. The main conclusions of each chapter are given as follows.

In *Chapter 2*, the cyclic elasto-viscoplastic constitutive model for clay proposed by Kimoto et al. (2013) and the model extended for unsaturated soils, using the skeleton stress and the suction effect by Shahbodaghkhan (2011), were reviewed. Their performance was then studied through cyclic test simulations. Moreover, the elasto-plastic model developed by Oka et al. (1999), considering nonlinear kinematic hardening and the generalized and non-associated flow rule, was also reviewed, and the results of cyclic triaxial test simulations were presented.

In *Chapter 3*, a finite deformation formulation, based on the updated Lagrangian scheme for partially saturated soils, was presented. The Newmark β method was used to discretize the time domain in which Rayleigh's damping, which is proportional to the initial stiffness and mass matrix, is included. The van Genutchen type of characteristic equation was adopted as the constitutive model between the saturation and the suction. In addition, finite element code COMVIDY-2D by Oka et al. (2013), developed for the two-dimensional large deformation dynamic coupled analyses of soils, was presented.

In *Chapter 4*, four different types of ground profiles, including soft clay in the foundation, were subjected to two acceleration records with different magnitudes and durations. Dynamic finite element analyses were performed using an elasto-viscoplastic model for clay and an elasto-plastic model for sand in the context of finite deformation. The FEM model used in this analysis consists of 880 eight-node

isoparametric plane strain elements and the adoption of equal displacement between nodes at both side elements for the lateral boundary conditions. Motions from the 1995 Hyogo-ken Nambu Earthquake (1995 Kobe Earthquake) and the 2011 off the Pacific Coast of Tohoku Earthquake (2011 Tohoku Earthquake) were used as the input motions. The dominant period of the 2011 Tohoku Earthquake was smaller than that of the 1995 Kobe Earthquake. However, the 2011 Tohoku Earthquake had a long duration of 250 seconds, while the 1995 Kobe Earthquake had a shorter duration of 30 seconds.

In the Type 1 ground profile, the embankment made of sandy soil lies on a saturated clay layer. When subjected to the 1995 Kobe Earthquake, the settlement, the lateral spreading, and the heaving around the toe of the embankment were larger than the corresponding responses for the 2011 Tohoku Earthquake. The embankments were slightly damaged in both cases.

The Type 2 ground corresponds to the case in which the embankment is in a clayey foundation due to consolidation and the bottom is below the water table. This ground exhibited a small amount of settlement and damage after the 1995 Kobe Earthquake. When subjected to the 2011 Tohoku Earthquake, however, the sandy soil below the water table was liquefied and the embankment exhibited large settlement, lateral movement, and heaving with a vertically localized zone in the body.

In the Type 3 ground, before the earthquake, the river embankment was in a soft foundation and the water table existed inside the embankment body. When this ground was subjected to the 1995 Kobe Earthquake, although no extensive liquefaction could be seen in the foundation, a deep sliding type of localization and lateral spreading were observed. When subjected to the 2011 Tohoku Earthquake, however, parts of the embankment body and foundation were liquefied and the embankment manifested largest settlement with vertically localized deformation. Heavy damage was presented in this case.

Finally, in the Type 4 ground, the embankment is on a saturated sandy layer lying on a clay layer. Due to the shaking of the 1995 Kobe Earthquake, a uniform slump into the liquefied sandy bed was seen. However, in the response to the 2011 Tohoku Earthquake, this ground experienced a lateral flow on the liquefied foundation with deep vertical or inclined localization toward the center.

In all cases, the soft clay foundation caused an amplification effect. The analysis results for the Type 3 ground profile show that the bottom of the embankment had settled due to the consolidation of clay, and that the water table existed inside the embankment, which was reported to have been the weakest state against liquefaction during the 2011 Tohoku Earthquake and showed the most severe damage due to the long duration of the earthquake motion.

In *Chapter 5*, a comparison between the results of the numerical analyses on river embankments using finite deformation and infinitesimal strain methods was performed. In the IS (infinitesimal strain) analysis method, it is seen that excess pore-water pressure developed earlier in both the elasto-plastic and elasto-viscoplastic models. However, it was also quick to dissipate. The settlements of the embankment calculated by the IS method were larger than those by the FD (finite deformation analysis with updated Lagrangian scheme) method. However, heaving and lateral spreading of the embankment toe by the FD method were found to be larger than those by the IS analysis method

The finite deformation analysis was found to be more stable for the analysis of liquefaction and large strains. Simulation results by the FD method for embankments on liquefiable foundations had a better agreement with the field observations in terms of failure mechanisms. However, the applicability of the finite deformation analysis method, i.e., the updated Lagrangian method, needs to be studied for very high strain rate problems, such as collision. In this sense, the finite deformation method is not yet absolutely perfect.

6.2. Recommendations for Future Works

Based on the assumptions, findings, and results of this study, the following recommendations are made for future research works:

In this research, simplified geometry and homogenous soil behavior were assumed for the ground profiles and the embankments. Assuming real geometry and heterogeneity of the material will naturally lead to more realistic results. It should also be noted that most of the research, so far, has been dedicated to the effects of the heterogeneity of the foundation ground. However, more attention should be paid to the heterogeneity in geotechnical structures, such as permeability and the mechanical properties, etc.

The earthquake motions used in this research were from the 1995 Kobe and the 2011 Tohoku Earthquakes. These two types of earthquakes were different in frequency content, duration, and amplitude. However, few analyzes can ever include all the possible different characteristics of earthquake motions. Thus, it is suggested that simulations for other types of input earthquakes, including expected ones, be continued.

The ground profile assumed in the analyses in this research was fully saturated. However, in order to approach the real behavior of embankments, it is strongly recommended that partially saturated soils at a shallow depth of the ground be assumed in future works.

The foundation profiles assumed for the river embankments in this study mainly contained soft clay. Nevertheless, the stiffness of the foundation has been proved to be very important to the behavior of embankments. Therefore, it is necessary to consider the effect of this stiffness in future studies.

References

Alonso, E, Gens, A. and Josa Garcia-Tornel, A. (2009). A constitutive model for partially saturated soils. Geotechnique, **40**(3), 405-430.

Belytschko, T., Liu,W.K. and Moran, B. (2000). The finite elements for continua and structures, John Wiley and Sons, New York.

Biot, M.A. (1941). Three-dimensional theory of consolidation. Journal of Applied Physics, **12**(2), 155-164.

Biot, M.A. (1956). Theory of propagation of elastic waves in a fluid-saturated porous solid. I. Low-frequency range. The Journal of the Acoustical Society of America, 28, 168.

Biot, M.A. (1962). Mechanics of deformation and acoustic propagation in porous media. Journal of Applied Physics, **33**(4), 1482-1498.

Bishop, A.W. and Donald, I.B. (1961). The experimental study of partly saturated soil in the triaxial apparatus. In Proceedings of the 5th International Conference on Soil Mechanics and Foundation Engineering, Paris, **1**, 13-21.

Bishop, A.W. (1960). The measurement of pore pressure in the triaxial test. Proc. Conf. Pore Pressure and Suction in Soils, Butterworth, London, 38-46.

Borja, R.I. (2002). Bifurcation of elastoplastic solids to shear band mode at finite strain. Computer Methods in Applied Mechanics and Engineering, **191**(46), 5287-5314.

Chaboche, J.L. and Rousselier, G. (1983). On the plastic and viscoplastic constitutive equations—Part I: Rules developed with internal variable concept. Journal of Pressure Vessel Technology, **105**(2), 153-158.

Chiaro, G., Koseki, J. and Sato, T. (2012). Effects of initial static shear on liquefaction and large deformation properties of loose saturated Toyoura sand in undrained cyclic torsional shear tests. Soils and Foundations, **52**(3), 498-510.

Finn, W.D.L., Yogendrakumar, M., Ledbetter, R. and Yoshida, N. (1991). Analysis of liquefaction induced displacements. In Proceedings of 7th International Conference on Computer Methods and Advances in Geomechanics, Cairns, Australia, 913-921.

Fredlund, D.G. and Morgenstern, N.R. (1977). Stress state variables for unsaturated soils. Journal of Geotechnical and Geoenvironmental Engineering, ASCE, **103**(GT5), 313-321.

Geotechnical Extreme Events Reconnaissance (GEER) Association (2010). www.geerassociation.org, URL.

Harder, L. F., Leslie, F., Kelson, K. I., Kishida, T., & Kayen, R. (2011). Preliminary observations of the Fujinuma dam failure following the March 11, 2011 Tohoku Offshore Earthquake,

Japan. Geotechnical Extreme Events Reconnaissance Report No. GEER-25e, www. geerassociation. org, URL.

Hoizumi, A. (1996). Mechanical behavior of clay during cyclic loading and elasto-viscoplastic model, Master thesis, Gifu University. (in Japanese)

Iai, S. and Kameoka, T. (1993). Finite element analysis of earthquake induced damage to anchored sheet pile quay walls. Soils and Foundations, **33**(1), 71-91.

Investigation Committee of the 1978 Miyagiken-oki Earthquake at Tohoku Branch of JSCE (1980). General Report on the 1978 Miyagiken-oki Earthquake.

Japan Institute of Construction Engineering (JICE) (2011). 3rd Urgent Exploratory Committee for the Earthquake Resistant Measure of River Embankments, August 27, 2011, Material-1; http://www.jice.or.jp/sonota/t1/201106210.html.

Jommi, C. (2000). Remarks on the constitutive modelling of unsaturated soils. Experimental evidence and theoretical approaches in unsaturated soils, 139-153.

Kaliakin, V.N. and Dafalias, Y.F. (1990). Theoretical aspects of the elastoplastic-viscoplastic bounding surface model for cohesive soils. Soils and Foundations, **30**(3), 11-24.

Kaneko, M., Sasaki, Y., Nishikawa, J., Nagase, M. and Mamiya, K. (1995). River dike failure in Japan by earthquakes in 1993. Proc. 3rd Int Conf. on Recent Advances in Geotechnical Earthquake Engineering and Soil Dynamics, edt. By S. Prakash, **1**, St. Louis, Missouri, 495-498.

Kanto Regional Development Bureau of MLIT. (2011). Material-1 and reference materials of the 3rd Exploratory Committee of MLIT on the Earthquake Resistant Measure of River Embankments, 2011.9.4, tp://www.ktr.mlit.go.jp/river/bousai/river_bousai00000090.html.

Kimoto, S. and Oka, F. (2005). An elasto-viscoplastic model for clay considering destructuralization and consolidation analysis of unstable behavior. Soils and Foundations, **45**(2), 29-42.

Kimoto, S., Oka, F., Fushita, T. and Fujiwaki, M. (2007). A chemo-thermo-mechanically coupled numerical simulation of the subsurface ground deformations due to methane hydrate dissociation. Computers and Geotechnics, **34**(4), 216-228.

Kimoto, S., Oka, F. and Higo, Y. (2004). Strain localization analysis of elasto-viscoplastic soil considering structural degradation. Computer Methods in Applied Mechanics and Engineering, **193**(27), 2845-2866.

Kimoto, S., Sahbodagh, K.B., Mirjalili, M. and Oka, F. (2013). A cyclic elasto-viscoplastic constitutive model for clay considering the nonlinear kinematic hardening rules and the structural degradation, Int. J. Geomechanics, ASCE, to appear.

Kinki Regional Development Bureau of MILT. (2010). Research report on the study of prevention method of the deformation of super river embankment.

Kohgo, Y., Nakano, M. and Miyazaki, T. (1993). Theoretical aspects of constitutive modelling for unsaturated soils. Soils and Foundations, **33**(4), 49-63.

Laloui, L. and Nuth, M. (2009). On the use of the generalized effective stress in the constitutive modelling of unsaturated soils. Computers and Geotechnics, **36**(1), 20-23.

Lambe, T.W. and Whitman, R.V. (1969). Soil Mechanics, John Wiley & Sons, 553 p.

Leroueil, S., Samson, L. and Bozozuk, M. (1983). Laboratory and field determination of preconsolidation pressures at Gloucester. Canadian Geotechnical Journal, **20**(3), 477-490.

LIQCA Research and Development Group (Representative: F. Oka Kyoto University) (2005). User's manual for LIQCA2D04 (2005 released print).

LIQCA Research and Development Group (Representative: F. Oka, Kyoto University) (2011). Materials for LIQCA2D11・LIQCA3D11 (2011 released print).

Loret, A. and Alonso, E.E. (1980). Consolidation of unsaturated soils including swelling and collapse behaviour. Geotechnique, **30**(4), 449-477.

Matsuo, O., Shimazu, T., Uzuoka, R., Mihara, M. and Nishi, K. (2000). Numerical analysis of seismic behavior of embankments founded on liquefiable soils. Soils and Foundations, **40**(2), 21-39.

Mirjalili, M. (2011). Numerical analysis of a large-scale levee on soft soil deposits using two-phase finite deformation theory, PhD Thesis of Kyoto University.

Modaressi, H. and Laloui, L. (1997). A thermo‐viscoplastic constitutive model for clays. International Journal for Numerical and Analytical Methods in Geomechanics, **21**(5), 313-335.

Ogisako, E., Nishio, S., Denda, A., Oka, F. and Kimoto, S. (2007). Simulation of triaxial compression tests on soil samples obtained from seabed ground in deep sea by elasto-viscoplastic constitutive equation. In Proceedings of the Seventh ISOPE Ocean Mining Symposium, 63-68.

Oka, F. (1992). A cyclic elasto-viscoplastic constitutive model for clay based on the non-linear hardening rule. In Proceedings of 4th International Symposium on Numerical Models in Geomechanics, Swansea, 105-114.

Oka, F. (1996). Validity and limits of the effective stress concept in geomechanics. Mechanics of Cohesive- frictional Materials, **1**(2), 219-234.

Oka, F., Adachi, T. and Yashima, A. (1994). Instability of an elasto-viscoplastic constitutive model for clay and strain localization. Mechanics of materials, **18**(2), 119-129.

Oka, F., Feng, H. and Kimoto, S. (2008). A numerical simulation of triaxial tests of unsaturated soil at constant water and constant air content by using an elasto-viscoplastic model. In Proc. 1st European Conference on Unsaturated Soils. Taylor and Francis Group , 35-741.

Oka, F., Kodaka, T. and Kim, Y.S. (2004). A cyclic viscoelastic−viscoplastic constitutive model for clay and liquefaction analysis of multi‐layered ground. International Journal for Numerical and Analytical Methods in Geomechanics, **28**(2), 131-179.

Oka, F., Kodaka, T., Kimoto, S., Kim, Y. S., & Yamasaki, N. (2006, April). An elasto-viscoplastic model and multiphase coupled FE analysis for unsaturated soil. In Unsaturated Soils 2006, ASCE Geotechnical Special Publication , **147**(2), 2039-2050.

Oka, F., Kodaka, T., Koizumi, T. and Sunami, S. (2001). An effective stress based liquefaction analysis based on finite deformation theory. Computer Methods and Advances in Geomechanics, 1113-1116.

Oka, F., Kodaka, T., Morimoto, R. and Kita, N. (2002). A liquefaction analysis method based on finite deformation theory using a cyclic elasto-plastic model for sand. Proc. of 5th WCCM.

Oka, F., Shahbodaghkhan B., Kimoto, S. and Sadeghi, H. (2013). Program COMVIDY-2D, large deformation dynamic analysis based on the three-phase mixture theory, Geomechanics Lab, Kyoto University.

Oka, F. (1988). The validity of the effective stress concept in soil mechanics. Micromechanics of Granular Materials, M. Satake and JT Jenkins eds., Elsevier Science Publishers BV, Amsterdam, 207-214.

Oka, F., Yoshida, N., Kai, S., Tobita, T., Higo, Y., Torii, N., Kagamihara, S., Nakanishi, N., Kimoto, S., Yamakawa, Y., Touse, Y., Uzuoka, R. and Kyoya, T. (2012). Reconnaissance Report of Geotechnical Damage due to the 2011 off the Pacific Coast of Tohoku Earthquake – 4. Northern Area of Miyagi Prefecture, Journal of JGS, **7**(1), 37-55.

Oka, F., Tsai, P., Kimoto, S., & Kato, R. (2012). Damage patterns of river embankments due to the 2011 off the Pacific Coast of Tohoku Earthquake and a numerical modeling of the deformation of river embankments with a clayey subsoil layer. Soils and Foundations, **52**(5), 890-909.

Oka, F., A. Yashima, Tateishi, A., Taguchi, Y. and Yamashita, S. (1999).A cyclic elasto-plastic constitutive model for sand considering a plastic-strain dependence of the shear modulus. Geotechnique, **49**(5), Oct., 661-680.

Oka, F., Kimoto, S. and Kato, R. (2011). Seepage-deformation coupled numerical analysis of unsaturated river embankment using an elasto-plastic model. First International Conference on Geotechnique, Construction Materials and Environment, Mie, Japan, Nov.21-23, 2011, CD-ROM, ISBN: 978-4-9905958-0-7 C3051.

Oka, F. and Kimoto, S. (2012). Computational Modelling of Multi-Phase Geomaterials. CRC Press.

Perzyna, P. (1963). The constitutive equations for work-hardening and rate sensitive plastic materials. Proc. Vibrational Problems, **4**(3), 281-290.

Peirce, D., Shih, C. F. and Needleman, A. (1984). A tangent modulus method for rate dependent solids. Computers and Structures, **18**(5), 875-887.

Research Institute for Earth Science and Disaster Prevention (2011). Foundation strong motion observation network http:www.kik.bosai.go.jp. (in Japanese)

Sadeghi, H., Oka, F. and Kimoto S. (2013). Proc. JSCE 15th International Symposium, CS2-010, 19-20, Japan.

Sasaki, Y., Oshiki, H. and Nishikawa, J. (1994). Embankment failure caused by the Kushiro-Oki earthquake of January 15, 1993, Performance of ground and soil structures during earthquakes, 13th ICSMFE, JGS, 61-68.

Sasaki, Y., Towhata, I., Miyamoto, K., Shirato, M., Narita, A., Sasaki, T., & Sako, S. (2012). Reconnaissance report on damage in and around river levees caused by the 2011 off the Pacific coast of Tohoku earthquake. Soils and Foundations, **52**(5), 1016-1032.

Sawada, M. (2008). A cyclic elasto-viscoplastic model constitutive equation and visualization of microstructure for soils, Master thesis, Geomechanics Lab, Kyoto University. (in Japanese)

Shahbodagh, K.B. (2011). Large deformation dynamic analysis method for partially saturated elasto-viscoplastic soils, PhD Thesis of Kyoto University.

Terzaghi, K. (1943). Theoretical Soil Mechanic, John Wiley and Sons.

Terzaghi, V.K. (1936). The shearing resistance of saturated soils and the angle between the planes of shear. In Proceedings of the 1st International Conference on Soil Mechanics and Foundation Engineering, **1**, 54-56.

Thomas, H.R. and He, Y. (1998). Modelling the behaviour of unsaturated soil using an elastoplastic constitutive model. Géotechnique, **48**(5), 589-603.

Tohoku Regional Development Bureau of MLIT (2011), Material-3, Interim Report by the 3rd investigative commission for the restoration of the river dikes of Kitakami River etc. July 29, 2011, 18-19. (in Japanese)

Tomita, Y. (1994). Simulations of plastic instabilities in solid mechanics. Applied Mechanics Review, **47**(6) Part 1, 171-205.

Towhata, I. (2008). Geotechnical Earthquake Engineering, Springer.

Uzuoka, R. and Borja, R.I. (2012). Dynamics of unsaturated poroelastic solids at finite strain. International Journal for Numerical and Analytical Methods in Geomechanics, **36**(13), 1535-1573.

van Genutchen, M.T. (1980). A closed-phase mixture model of liquids-gas flow and heat transfer in capillary porous media. Soil Sci. Soc. Am. J, **44**, 892-898.

Watanabe, T., Oka, F., Kimoto, S., Higo, Y. and Yabuki, T. (2007). Simulation of cyclic triaxial tests of unsaturated silt by elasto-viscoplastic model. Proc. 62th Annual Meeting of JSCE, Hiroshima, 211-212. (in Japanese)

Yasuda, S., Harada, K., Ishikawa, K. and Kanematsu, Y. (2012). Characteristics of liquefaction in Tokyo Bay area by the 2011 Great East Japan earthquake. Soils and Foundations, **52**(5), 793-810.